GENERAL ATOMIC

GA-A14112
UC-77

GAS-COOLED FAST BREEDER REACTOR

QUARTERLY PROGRESS REPORT
FOR THE PERIOD AUGUST 1, 1976 THROUGH OCTOBER 31, 1976

by

Project Staff

Prepared under
Contract E(04-3)-167
Project Agreement No. 23
for the
San Francisco Operations Office
U.S. Energy Research and Development Administration

General Atomic Project 3228

Date Published: November 1976

PROGRESS REPORT SERIES

GA-5537	November 1, 1963 through July 31, 1964
GA-6667	August 1, 1964 through July 31, 1965
GA-7645	August 1, 1965 through July 31, 1966
GA-8107	August 1, 1966 through July 31, 1967
GA-8787	August 1, 1967 through July 31, 1968
GA-8895	August 1, 1968 through October 31, 1968
GA-9229	November 1, 1968 through January 31, 1969
GA-9359	February 1, 1969 through April 30, 1969
GA-9639	May 1, 1969 through July 31, 1969
GA-9811	August 1, 1969 through October 31, 1969
GA-9838	November 1, 1969 through January 31, 1970
GA-10517	February 1, 1970 through January 31, 1971
GA-10645	February 1, 1971 through April 30, 1971
GA-A10803	May 1, 1971 through July 31, 1971
GA-A10906	August 1, 1971 through October 31, 1971
GA-A12003	November 1, 1971 through January 31, 1972
GA-A12252	May 1, 1972 through July 31, 1972
GA-A12421	August 1, 1972 through October 31, 1972
GA-A12530	November 1, 1972 through January 31, 1973
GA-A12635	February 1, 1973 through April 30, 1973
GA-A12728	May 1, 1973 through July 31, 1973
GA-A12824	August 1, 1973 through October 31, 1973
GA-A12894	November 1, 1973 through January 31, 1974
GA-A13021	February 1, 1974 through April 30, 1974
GA-A13148	May 1, 1974 through July 31, 1974
GA-A13238	August 1, 1974 through October 31, 1974
GA-A13379	November 1, 1974 through January 31, 1975
GA-A13458	February 1, 1975 through April 30, 1975
GA-A13565	May 1, 1975 through July 31, 1975
GA-A13766	August 1, 1975 through October 31, 1975
GA-A13815	November 1, 1975 through January 31, 1976
GA-A13868	February 1, 1976 through April 30, 1976
GA-A13975	May 1, 1976 through July 31, 1976

ABSTRACT

The tasks of the gas-cooled fast breeder reactor (GCFR) program which are supported by the U.S. Energy Research and Development Administration include development of GCFR fuel, blanket, and control assemblies; development of the pressure equalization system for GCFR fuel; out-of-pile loop facility test program planning; fuels and materials development; fuel, blanket, and control rod analyses and development; nuclear analysis and reactor physics for GCFR core design; shielding requirements for the GCFR; reactor engineering to assess the thermal, hydraulic, and structural performance of the core and the core support structure; plant systems control; development of reactor components, including reactor vessel, control and locking mechanisms, fuel handling equipment, core support structure, shielding assemblies, main helium circulator, steam generator, and auxiliary circulator; development of a helium circulator test facility; reactor safety, including an in-pile safety evaluation program; and nuclear island engineering design.

CONTENTS

FIGURES

FIGURES (Continued)

FIGURES (Continued)

TABLES

TABLES (Continued)

1. INTRODUCTION

The various tasks of the gas-cooled fast breeder reactor (GCFR) program for the period August 1, 1976 through October 31, 1976 sponsored by the U.S. Energy Research and Development Administration (ERDA) are discussed in this quarterly progress report. The GCFR utility program, which is supported by a large number of electric utility companies, rural electric cooperatives, and General Atomic (GA), is primarily directed toward the development of a GCFR demonstration plant. The utility-sponsored work and the ERDA-sponsored work are complementary.

Analytical, experimental, and fabrication development is being accomplished under the core assembly development task to establish the basis for the design of GCFR fuel, blanket, and control assemblies. Analytical methods development for structural and thermal-hydraulic analyses is discussed, and the results of structural analysis of the fuel assembly components and thermal-hydraulic analysis of the blanket assembly during low power are presented. Current progress on rod spacer interaction tests, fuel assembly seismic and vibration test planning, and development of assembly fabrication techniques is also presented. The various subtasks of core assembly development and the work accomplished during this reporting period are discussed in Section 2.

The technology to support the design and construction of the pressure equalization system (PES) for GCFR fuel is being developed. This includes (1) the development of analytical models and computer codes which will be verified by test programs and testing of materials and seals and (2) the development of fabrication processes for the PES. These are discussed in Section 3.

To demonstrate the ability of GCFR fuel, control, and blanket assembly designs to meet design goals and verify predictions of analytical models, a

series of out-of-pile simulation tests will be performed. The emphasis of the tests will be on obtaining thermal-structural data for steady-state, transient, and margin conditions using electrically heated rod bundles in a dynamic helium loop. These are discussed in Section 4.

In the fuels and materials development program, thermal flux and fast flux irradiation programs are being conducted to establish conditions and design features specific to GCFR fuel rods, such as vented fuel, fission product traps, and surface-roughened cladding. In addition, a test program of smooth and surface-roughened GCFR cladding specimens is being conducted to determine how materials behave under irradiation. The fuels and materials tests, the analytical studies, and the results to date are presented in Section 5.

Under the fuel rod engineering task, performance of the fuel and blanket rods under steady-state and transient conditions is being evaluated to determine performance characteristics, operating limits, and design criteria. In addition, surveillance of the fuel rod and blanket rod technology of other programs is being carried out. These studies are presented in Section 6.

The objectives of the nuclear analysis and reactor physics task are to verify and validate the nuclear design methods which will be applied to the GCFR core design. A critical assembly experimental program is being carried out on the ZPR-9 facility at Argonne National Laboratory (ANL) for this purpose. Critical assembly design, analysis, and methods development are discussed in Section 7.

Verification of the physics and engineering analytical methods and the data for design of the GCFR shields is being conducted under the shielding requirements task along with an evaluation of the effectiveness of various shield configurations. The results of radial shield analyses and the work being done on structural analysis are presented in Section 8.

To assess the thermal-hydraulic performance of the GCFR reactor core, analytical methods and models are being developed and utilized to define operating strategies. These, together with the development of GCFR plant control systems and an evaluation of the capability of the prestressed concrete reactor vessel (PCRV) internal structures to provide postaccident fuel containment, are discussed in Section 9.

Section 10 presents the evaluation and development of the main components of the GCFR which are currently in progress, including reactor vessel, control and locking mechanisms, fuel handling, core support structure, shielding assemblies, main helium circulator, steam generator, and auxiliary circulator.

Development of a test facility for qualification testing of the main helium circulator is discussed in Section 11. This task includes the responsibility for (1) evaluation studies of alternative test facility concepts, (2) preparation of specifications for the selected facility, and (3) final design, construction, and checkout of the facility.

The objective of the reactor safety task, which is discussed in Section 12, is to study the safety aspects of the GCFR using logical probabilistic methods to determine the probabilities associated with accident initiation and progression sequences.

The gas reactor in-pile safety test (GRIST) program is being studied as a potential follow-on to the analytical and experimental programs covering design basis accidents. The objective of the GRIST program is to provide information related to beyond-design-basis accidents, particularly the behavior of melted cladding and fuel. Progress in test assembly analysis and design is discussed in Section 13.

Section 14 discusses the nuclear island. The purposes of this task are to accomplish engineering design work on the nuclear island portion of the demonstration plant and to resolve the interface requirements of major nuclear steam supply (NSSS) and balance of plant (BOP) systems.

2. CORE ASSEMBLY DEVELOPMENT (189a No. SU006)

2.1. FUEL AND CONTROL ASSEMBLY ANALYSIS

2.1.1. Introduction

The analytical basis for the design and development of the GCFR fuel and control assemblies is being developed through evaluation of experimental data. Because complete prototype in-pile tests cannot be conducted, a strong analytical base supported by development tests is required to design the core assemblies. The current effort is devoted to the development of an adequate steady-state and transient analysis capability in the areas of thermal-hydraulic and structural analyses to provide a basis for assembly design criteria and specific test requirements.

During the previous quarter, the outer solutions in FLOMAX were checked using several sample problems. Special techniques were developed to handle surface transitions and abrupt changes in heat flux, and preliminary comparisons with COBRA calculations indicated excellent agreement. The COBRA code was modified (1) to permit the analysis of carbon-dioxide-cooled fuel bundles in order to perform analysis of the Swiss Federal Institute for Reactor Research (EIR) experiments (performed with Swiss funding) and (2) to increase the maximum number of types of subchannels, i.e., the number of friction factor and Stanton number correlations, which may be applied to a problem. Based on annulus test data, a correlation of the friction factor as a function of the Reynolds number and the relative roughness was developed.

During this quarter, the inner temperature solutions were programmed in FLOMAX, and good preliminary results were obtained. The same technique reported last quarter (Ref. 2-1) for the friction factors was used in

correlating selected Stanton number data; a subprogram STCENT was developed from the correlation for use in subsequent analyses. Conduction analysis of ribbed cladding was performed to determine the axial variation of the midwall temperature.

2.1.2. Analytical Methods Development

2.1.2.1. FLOMAX Thermal Analysis Code. During this quarter, work continued on the development of the thermal-hydraulic subchannel analysis code FLOMAX. The mathematical problem of rod bundle codes involves determination for each subchannel i of the mass velocities $G_i(x)$, the temperatures $T_i(x)$, and the pressures $P_i(x)$ as a function of the axial coordinate x. In FLOMAX, this is done by expanding these variables into the asymptotic series

$$G_i(x) \sim G_{oi} + \sigma G_{1i}(x) + \sigma g_i(\xi) + O(\sigma^2) \quad , \tag{2-1}$$

$$T_i(x) \sim T_o(x) + \sigma T_{1i}(x) + \sigma t_i(\xi) + O(\sigma^2) \quad , \tag{2-2}$$

$$P_i(x) \sim P_o(x) + \sigma P_1(x) + \sigma p_i(\xi) + O(\sigma^2) \quad , \tag{2-3}$$

where the uppercase letters denote outer variables which are valid away from the inlet and geometry transitions, the lowercase letters denote inner variables which are valid near the inlet and transitions, σ is a small parameter, and the stretched inner coordinate is $\xi = x/\sigma$.

Programming of the inner temperature solutions $t_i(\xi)$ was completed during this quarter, and good preliminary results were obtained for a two-channel sample problem. Some difficulties were experienced with multi-channel problems having abrupt axial changes in heat generation and rod roughening; however, after an extensive debugging effort, these difficulties were resolved and the code now appears to correctly calculate the subchannel temperatures for general rod bundles. Good agreement has been obtained with a COBRA execution of a 28-channel model of the BR-2 test assembly,

including the effect of power tilting in the assembly. This model is currently under further COBRA and FLOMAX execution to compare the effect of turbulent mixing and the presence of spacers.

2.1.2.2. Correlation of Rough-Surface Stanton Numbers. Subchannel thermal-hydraulic analysis computer codes such as FLOMAX and COBRA use correlations of the friction factor (f) and the Stanton (St) or Nusselt (Nu) numbers to calculate pressure drops and system temperatures. Correlations of f and St were developed from test data for single, heated, roughened rods mounted in annular flow tubes. The test data were first "transformed" to separate the effects on the flow field of the smooth outer tube wall from those of the rough inner rod. The procedure for correlating the friction factor data is described in Ref. 2-1. A similar procedure was used to correlate the heat transfer data, expressed in terms of the Stanton number, as a function of the Reynolds number (Re) and the relative roughness (ε), defined as the ratio of roughness rib height to hydraulic diameter.

A number of Stanton number transformation techniques have been developed, three of which are compared: (1) a technique by Nathan and Pirie (Ref. 2-2) which is widely used in England; (2) a new method by Dalle Donne of Gesellschaft für Kernforschung (GfK), Germany, which is based on the earlier method of Maubach; and (3) a technique developed at EIR, Switzerland.

The Stanton number transformation of Nathan and Pirie consists of one equation:

$$\frac{St_1}{St} = \frac{f_1}{f}\left(\frac{D_h}{D_{h_1}}\right)^{0.5} (1.096 - 1.896\ f_1)\ (1.255 - 0.0432\ \log Re_1) \quad , \quad (4\text{-}2)$$

where f is the friction factor, and D_h is the hydraulic diameter. The subscript one indicates transformed parameters. This transformation

is very simple to use in the forward and inverse directions. However, it is expressed in terms of f_1, Re_1, and D_{h1} and is therefore directly affected by the technique used to transform friction factor data. Using the modified Warburton and Pirie transformation (Ref. 2-1) to obtain f_1, Re_1, and D_{h1}, the Stanton number data for EIR-ROHAN rod 19 were transformed by the Nathan-Pirie technique. Rod 19 was selected owing to its similarity to the GCFR fuel rod. The effect of this combination of transformations on the parameters is indicated in Fig. 2-1, where St_1 versus Re_1 data are plotted together with untransformed data. In general, for all methods, the transformation process increases the Reynolds number and the Stanton number of the data point. For example, for the point Re = 29,600 and St = 0.00771, the transformed Stanton number St_1 is 12% higher and Re_1 is 78% higher.

Figure 2-2 compares the three transformations applied to the EIR-ROHAN rod 19 test data. The Nathan-Pirie and Dalle Donne results compare very favorably, but the transformed results from EIR have consistently higher values of St_1, as much as 25% at low values of Re_1. Based on this comparison, the Nathan-Pirie technique was selected to transform annulus test data for subsequent correlation.

The technique used to fit the Stanton number data was essentially the same as that used for the friction factor data. However, rather than being constant above a certain Reynolds number, the curves were forced to vary as the function $Re_1^{-0.2}$. The selected interfacing points between the fitted regions were Re_1 values of 8,000 and 70,000. The points and slopes of the individual spline fits were matched at these Re_1 values. Below Re_1 = 2,000, a constant Nusselt number of 11 was used based on the work of Sparrow, et al. (Ref. 2-3) on laminar flow parallel to cylinders in an equilateral triangular array. For zero relative roughness and Re_1 greater than 8,000, the Dittus Boelter equation was used:

$$St_1 = 0.023\ Re_1^{-0.2}\ Pr^{-0.6} \quad . \tag{2-5}$$

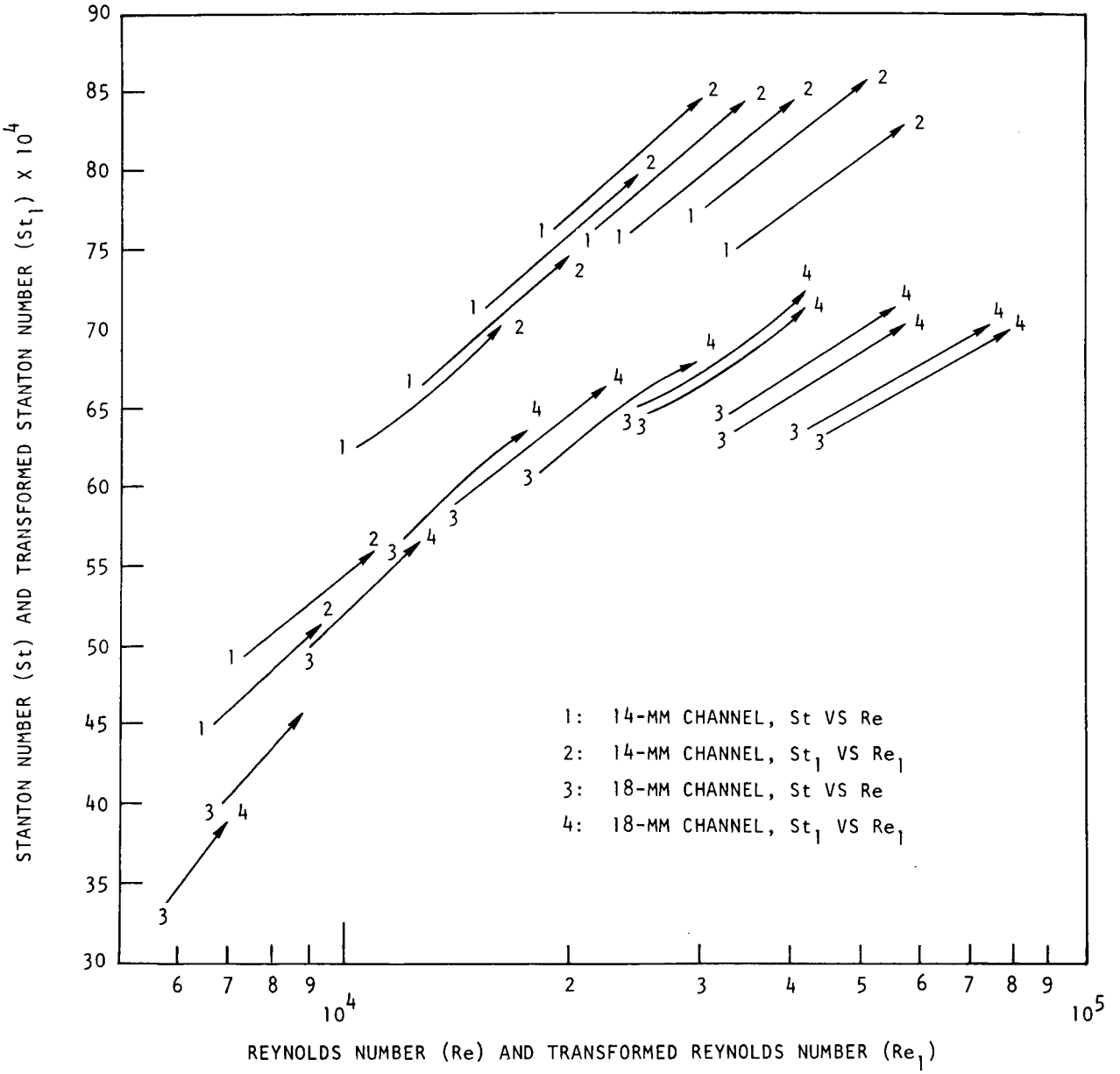

Fig. 2-1. Effect of the Nathan-Pirie transformation on Stanton and Reynolds numbers

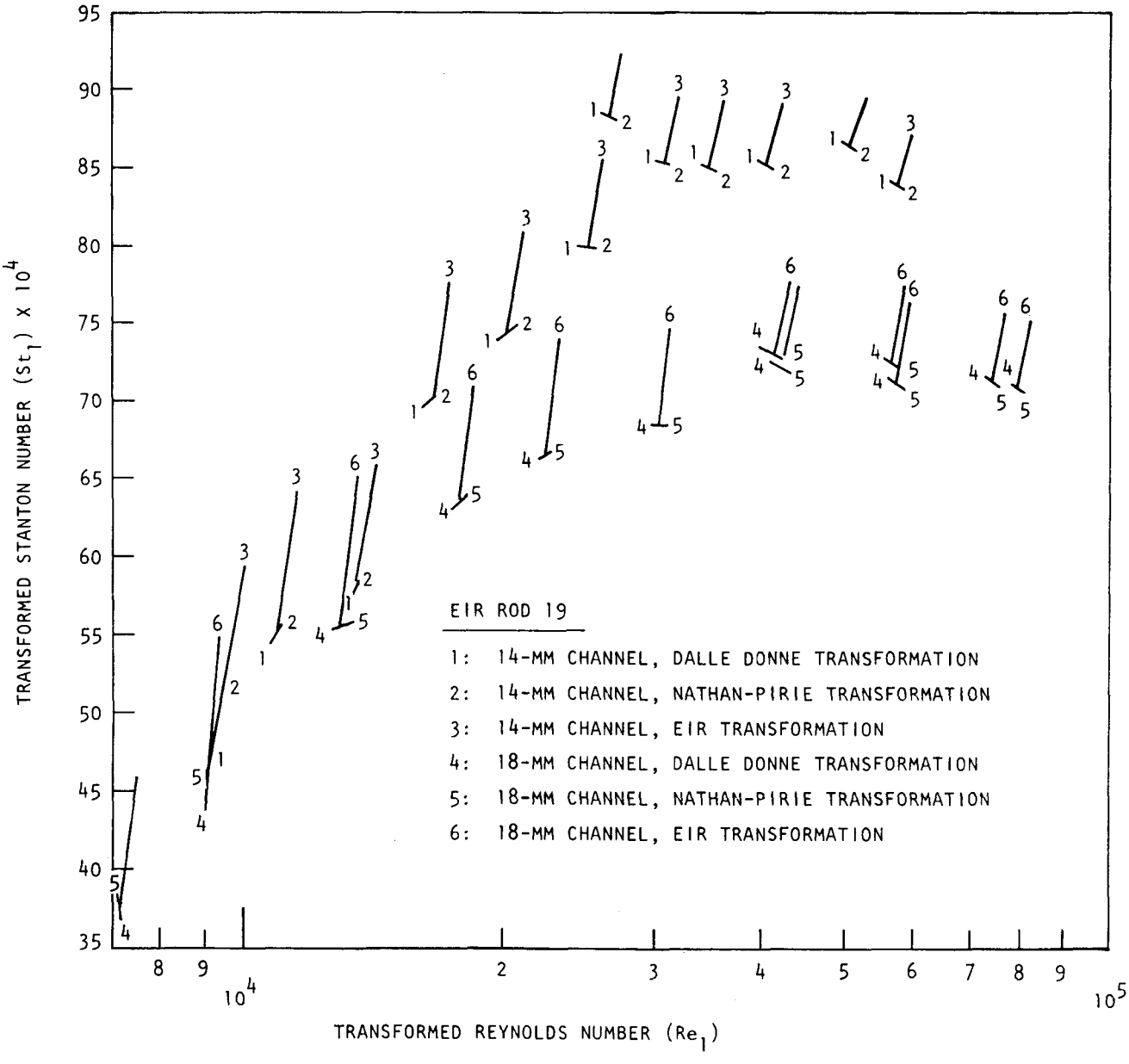

Fig. 2-2. Comparison of transformation methods

As discussed in Ref. 2-1, use of the spline equations requires specification of the ordinate and slope at each of the intersection points. At each point, equations of the form

$$St_1, \frac{\partial St_1}{\partial Re_1} = a_i + b_i(\varepsilon_1)^{c_i} \tag{2-6}$$

were used to specify these values. A nonlinear least squares technique was then used to determine the optimum values for the a_i, b_i, and c_i parameters based on the transformed Stanton number data. The results are shown in Fig. 2-3 with ε_1 as a parameter. At Re_1 equal to 100,000, the transformed Stanton number was related to the relative roughness by the equation

$$St_1(10^5, \varepsilon_1) = 0.00293 + 0.0244\ \varepsilon_1^{0.4} \quad .$$

To illustrate the adequacy of the correlation, predictions were made for each of the data points shown in Fig. 2-4 along with the original data. The total root-mean-square error is 2.7%, with most of the deviation due to normal test data scatter.

The function subprogram STCENT which calculates the transformed Stanton number given the transformed Reynolds number (RE1) and relative roughness (EPS1) has been developed. Functions for the cubic spline (SPLINE) and the slope of the cubic spline (CSLOPE) are given together with the parameters required to define the points and slopes at the boundaries of the various Reynolds number regions. The program selects the appropriate region and calculates the transformed Stanton number (St_1). This correlation is currently being used in conjunction with the inverse transformation to obtain heat transfer coefficients for the various subchannels of the GCFR fuel assembly.

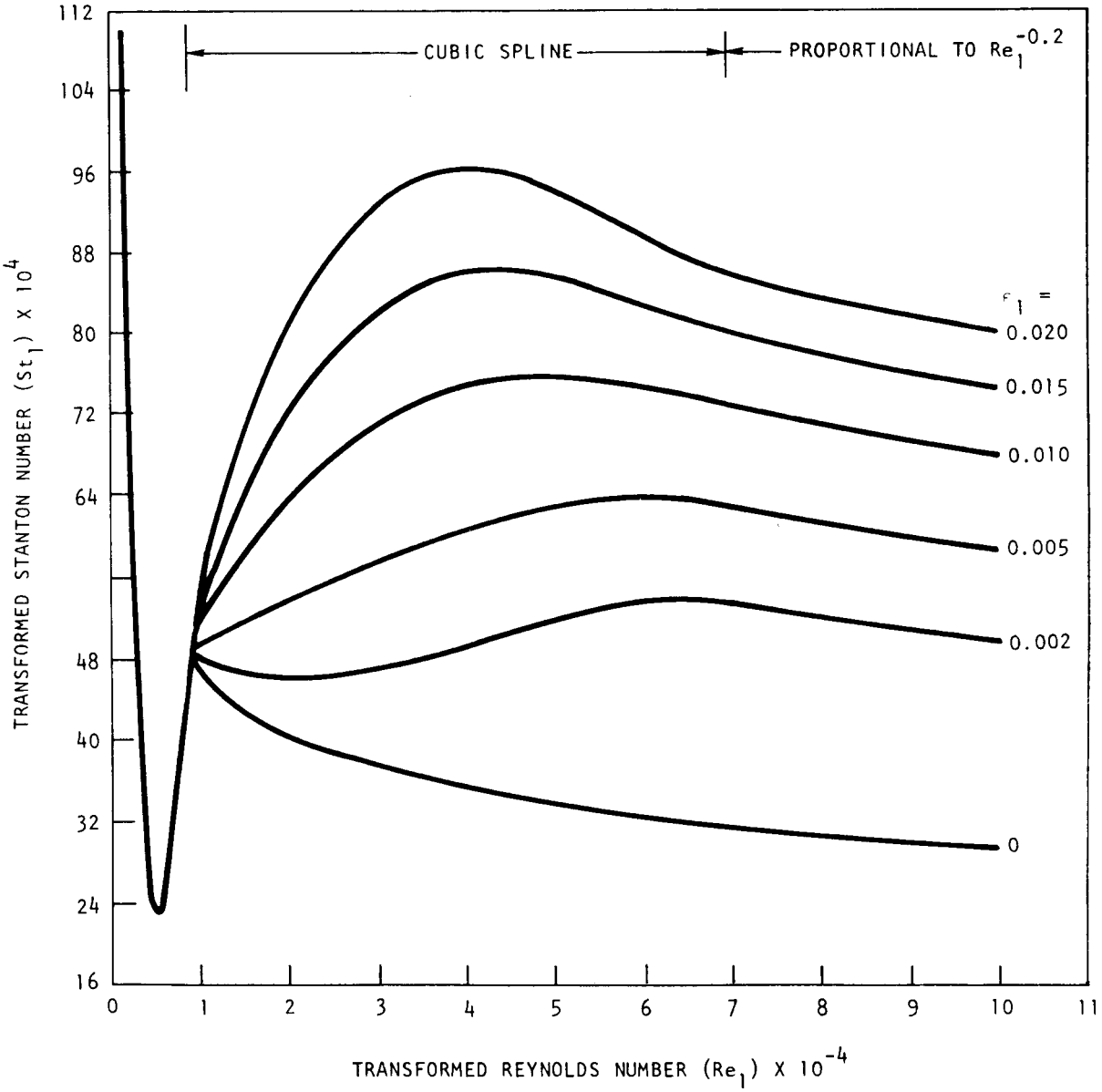

Fig. 2-3. Stanton number correlation

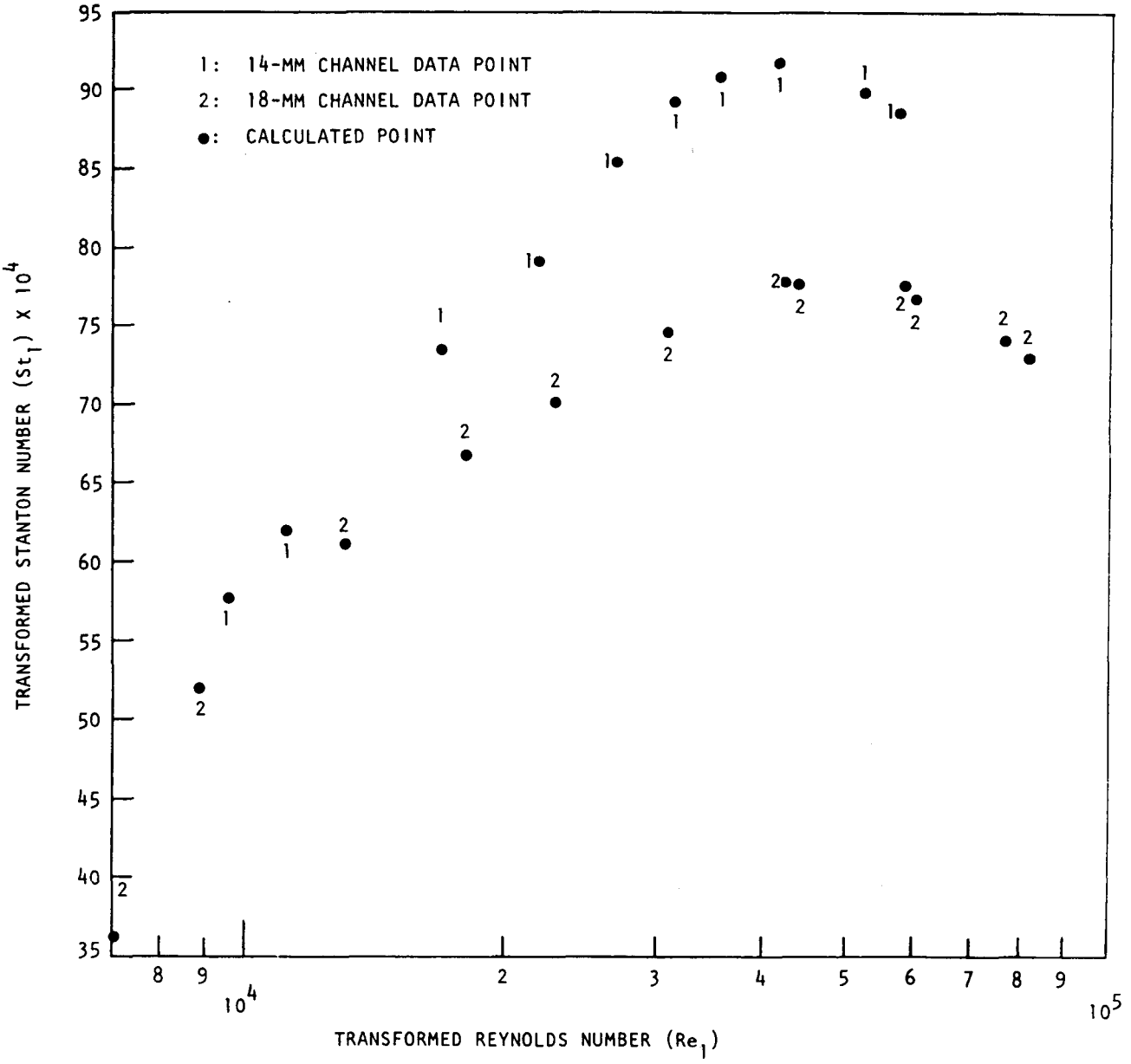

Fig. 2-4. Comparison of predictions and actual data

2.1.3. Thermal Analysis

The heat transfer coefficient varies along the axial length for a ribbed surface (Fig. 2-5), resulting in surface temperature variations (Fig. 2-6). These variations are reduced toward the inside surface of the rod owing to axial conduction in the cladding material. A thermal conduction analysis was carried out at the hot spot location to determine the deviation of the midwall temperature from the mean temperature. The results obtained (Fig. 2-7) indicated that the maximum temperature at the midwall is 3.5°C higher than the mean calculated value. For reactor calculations, a hot spot subfactor was defined owing to axial variation of the film coefficient; this subfactor is 1.067 applied to the nominal film drop.

2.2. BLANKET ASSEMBLY ANALYSIS

The purpose of this task is to develop and verify analytical techniques for blanket assembly analysis. These analytical techniques will be used to obtain preliminary and final designs of the blanket assembly and to determine the design margin requirements. This task includes thermal-hydraulic, structural, and dynamic analyses and evaluation of handling and shipping of the blanket assembly.

During the previous quarter, methods of obtaining the hot spot factors for the GCFR radial blanket assembly were reviewed, and a list of subfactors relevant to blanket assembly hot spot analysis was prepared. During this quarter, a scoping study for the low-ΔP GCFR radial blanket was done, and values for some of the hot spot subfactors were obtained.

2.2.1. Scoping Study for Low-ΔP GCFR Radial Blanket

It was recently proposed that the GCFR reference design be modified by reducing the pressure drop across the core from 293 kPa and increasing the inlet temperature from 323° to 350.6°C. These changes, if adopted for the GCFR reference design, would necessitate a redesign of the GCFR radial

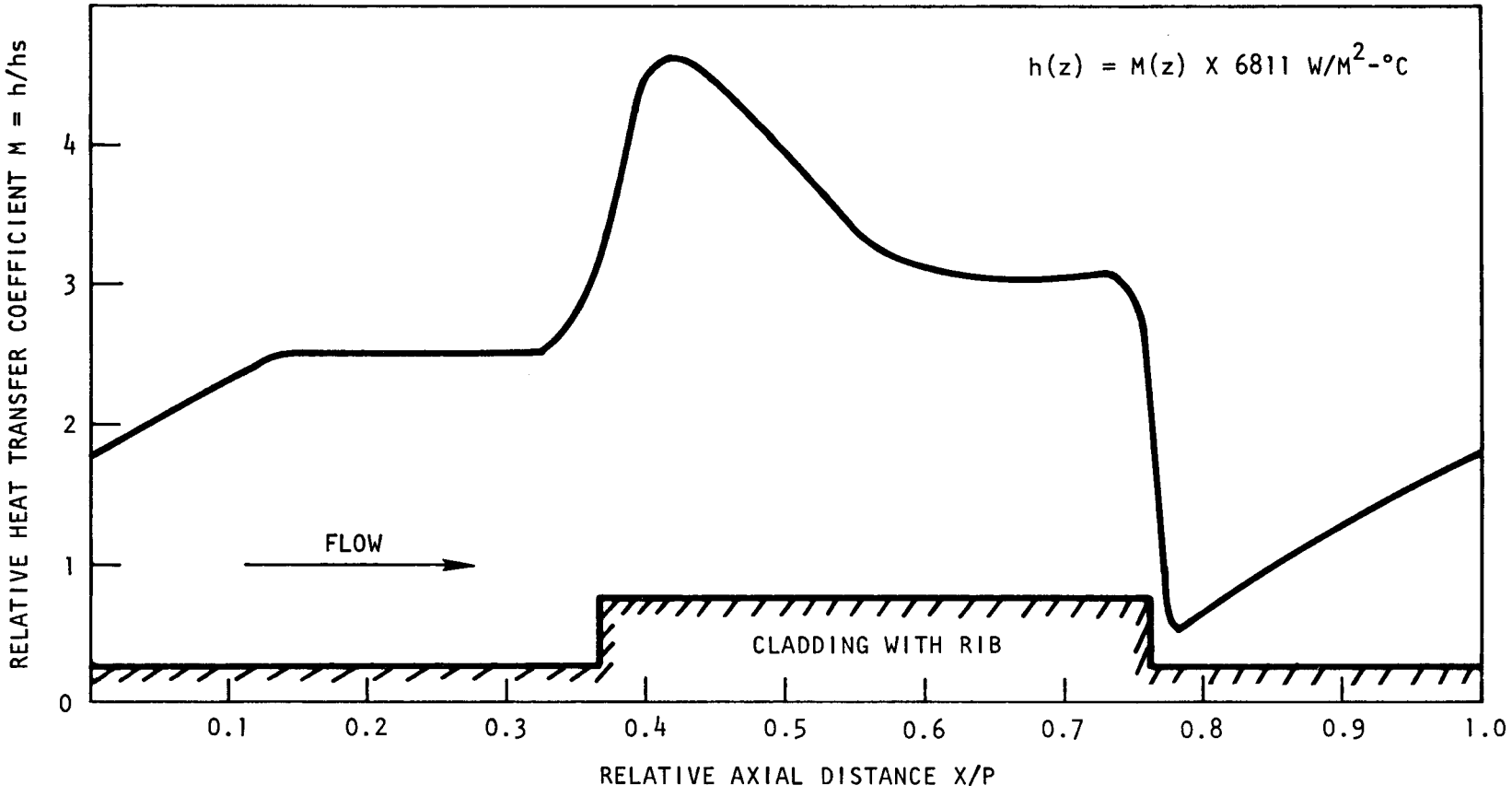

Fig. 2-5. Local heat transfer coefficient multiplier

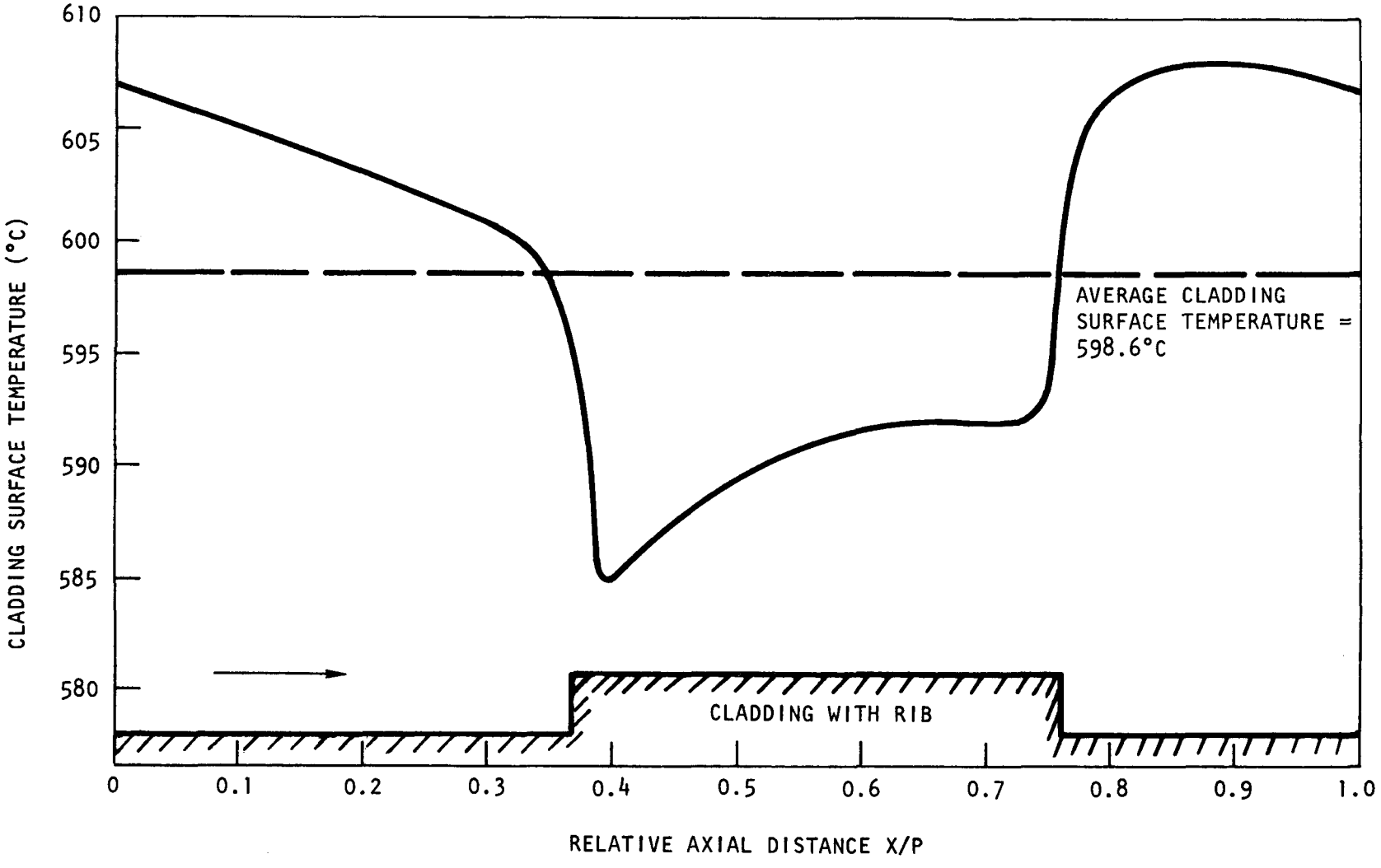

Fig. 2-6. Cladding surface temperatures

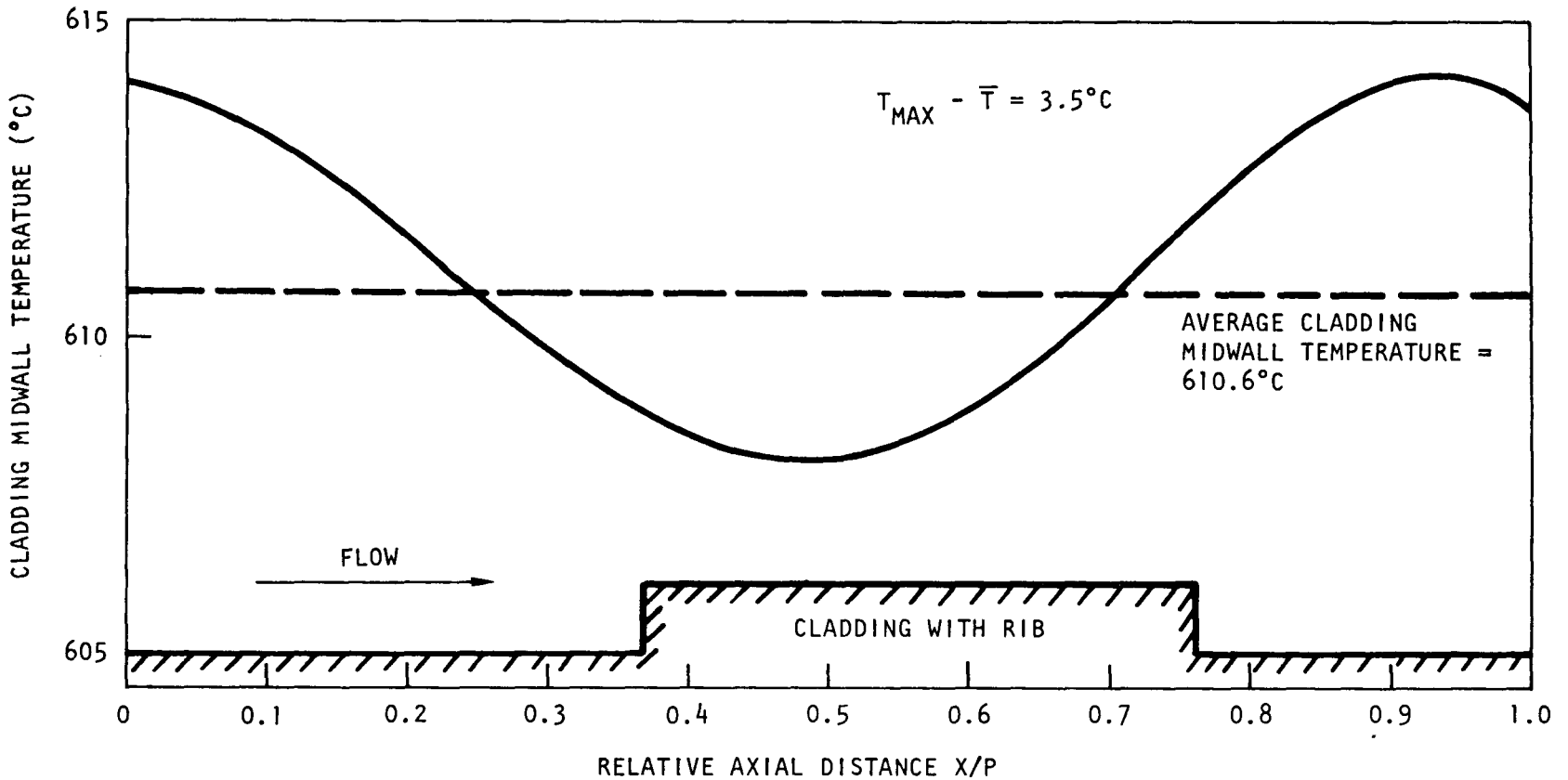

Fig. 2-7. Cladding midwall temperatures

blanket. The radial blanket design would change from the reference design because of the following reasons:

1. The pressure drop across the peak-powered blanket assembly must be equal to or less than the new ΔP across the core.

2. The low-ΔP core assemblies will have a larger duct, resulting in either larger blanket rods (if the number of rods and the pitch-to-diameter ratio are maintained) or a larger number of rods per assembly.

3. For the new design, the radial blanket will produce a larger percentage of the total power owing to larger neutron leakage of the more open lattice of the low-ΔP GCFR core.

2.2.1.1. Pressure Drop. The pressure drop across the blanket assembly with peak power was calculated using the COBRA code and the following correlation (Ref. 2-4):

$$\Delta P = M f_s \frac{L}{D_e} \frac{\rho V^2}{2g} \quad , \tag{2-7}$$

where $$M = \left[\frac{1.034}{(P/D)^{0.124}} + \frac{29.7(P/D)^{6.94} \, Re^{0.086}}{(H/D)^{2.239}} \right]^{0.885} \quad ,$$

ΔP = pressure drop (Pa),

f_s = smooth tube friction factor,

L = length of rod bundle (m),

D_e = equivalent hydraulic diameter of flow cell (m),

ρ = coolant density (g/cm^3)

V = bulk flow velocity (m/s),

g = gravitational constant (m/s^2)

P = pitch of rod bundle (m),

D = rod diameter (m),

H = wire wrap pitch (m),

Re = Reynolds number.

In each case, the flow was maintained so that the maximum midwall hot spot cladding temperature was less than 700°C.

Figure 2-8 shows the pressure drop across the radial blanket rod bundle as a function of wire diameter for 61 and 91 rods per assembly for a wire pitch of 300 mm. The total length of the rod is 2235 mm. As seen from Eq. 2-7, for a given number of rods and a given wire size, the pressure drop is also a function of wire pitch. Figure 2-9 shows the effect of wire pitch on the ΔP across the blanket for 61 rods per assembly and wire diameters of 1.4 mm and 2.00 mm. The pressure loss decreases considerably when the wire pitch is increased from 150 to 500 mm, but beyond that the gain is quite small.

2.2.1.2. Volume Fraction. An important parameter which affects the main purpose of the radial blanket (i.e., to convert fertile material to fissile material) is the volume fraction of the fertile material in the radial blanket. Figure 2-8 shows the relation between wire size and volume fraction for N = 61 (N = number of rods/assembly) and N = 91. A study of Fig. 2-8 shows that for a given ΔP across the radial blanket assembly, N = 61 has a larger volume fraction than N = 91; besides the fabrication cost of blanket assemblies for N = 61 is about 22% less than that for N = 91. Hence, N = 61 is preferable to N = 91.

2.2.2. Radial Blanket Hot Spot Subfactors

During the last quarter, a list of the subfactors influencing the radial blanket hot spot temperatures was compiled (Ref. 2-1). During this quarter, the influence of some of the uncertainties on the hot spot temperature was evaluated using the subchannel code COBRA. An analysis considering the worst possible combination of geometric tolerances on rod and wire diameters was used to obtain a channel and a film subfactor. Subfactors due to uncertainties in friction factor correlation and wire-wrap

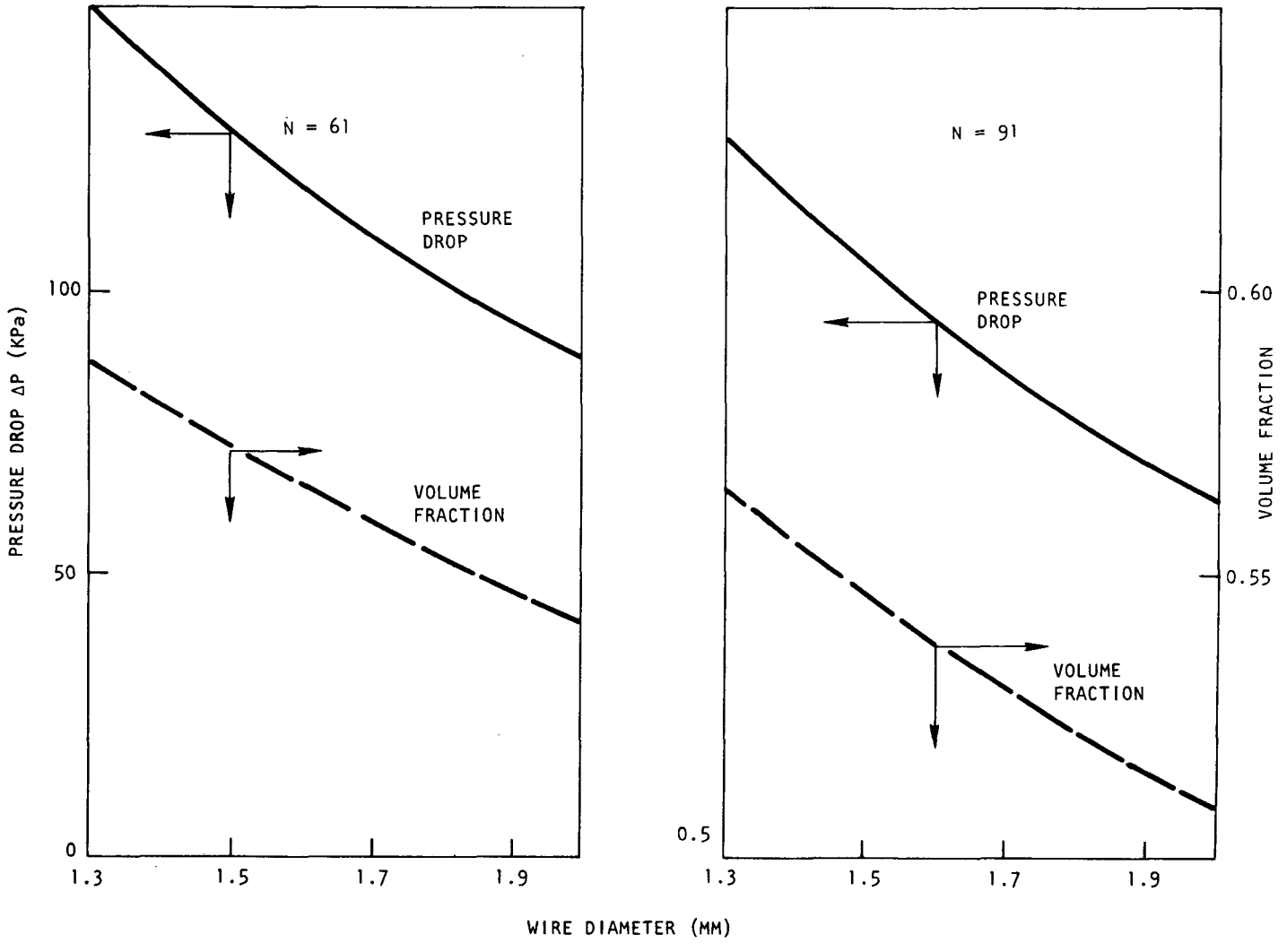

Fig. 2-8. Relationship between wire diameter, volume fraction, and pressure drop (rod bundle) for radial blanket (wire pitch = 300 mm)

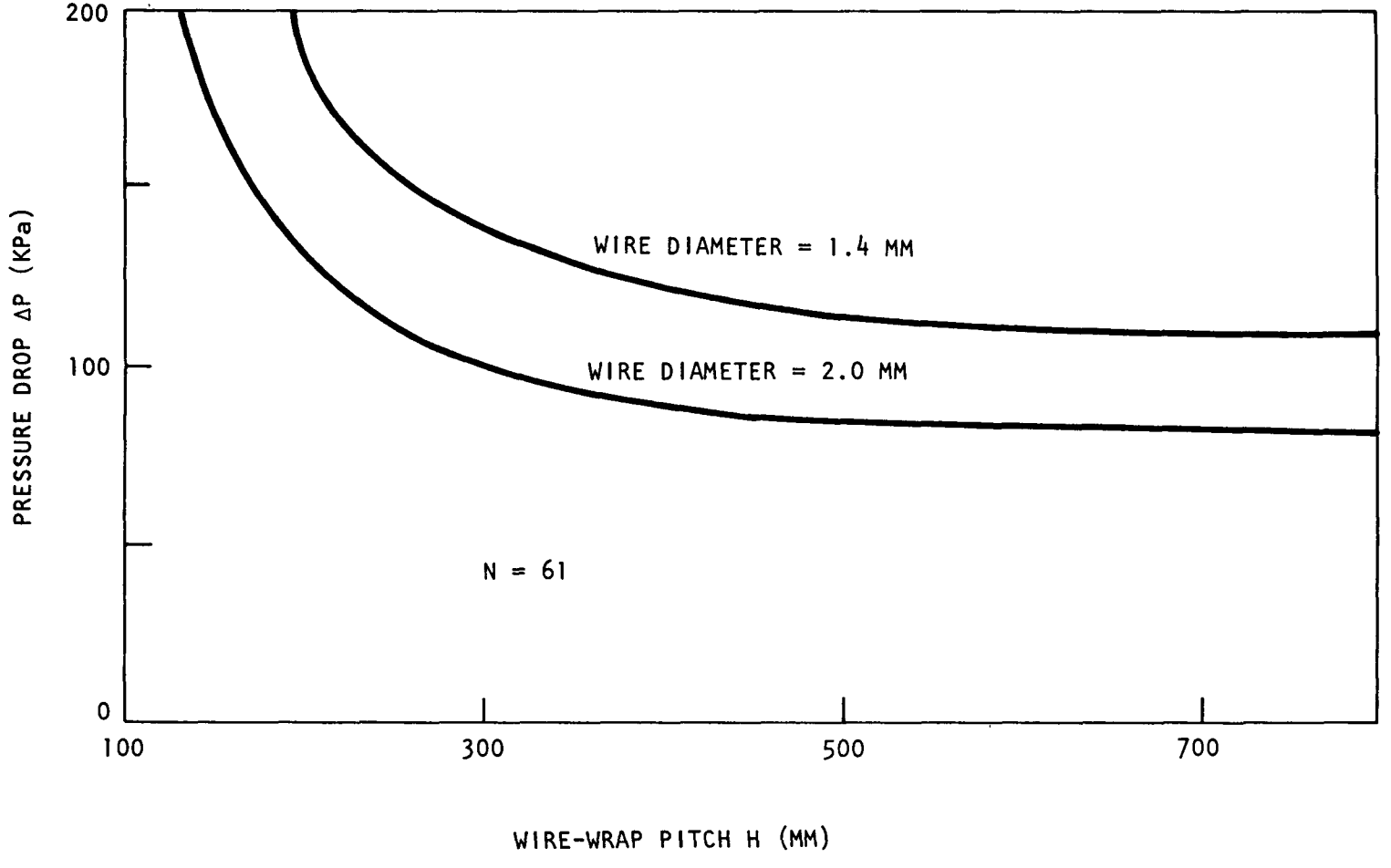

Fig. 2-9. Wire-wrap pitch vs pressure drop for radial blanket

mixing were similarly obtained. The uncertainties and the corresponding subfactors are as follows:

Parameter	Uncertainty (%)	Channel Factor F_c	Film Factor F_f	Cladding Factor F_{cl}
Cladding o.d. } rod Wire o.d. } pitch	0.06 0.90	1.071	1.013	1.00
Friction factor correlation	14	1.025	1.040	1.00
Flow sweeping correlation	50	1.034	1.00	1.00

2.3. ASSEMBLY MECHANICAL TESTING

The objective of this task is to conduct mechanical tests of core assembly components and subassemblies to simulate the mechanical loads expected during normal and abnormal reactor operating conditions. The current phase of the assembly mechanical testing program involves testing of fuel assembly components. The preliminary fuel rod/spacer interaction test using single spacer cells and rods was conducted during FY-76. The reproducibility testing of the hexagonal spacer cells was completed, and testing of a new modified hex design was initiated. The procurement of blanket assembly components for testing was initiated.

2.3.1. Fuel Rod/Spacer Interaction Test

The purpose of the rod/spacer interaction test is to evaluate the effect of interacting forces between the fuel rod and the spacers under the mechanical and environmental operating conditions expected in the GCFR. The interacting forces between the rod and the spacers are primarily caused by bowing induced by temperature gradients and irradiation-induced swelling. Reactor operational transients cause relative motion of the rod and spacer, which results in frictional forces. The frictional forces and relative motion cause wear of the rod and spacer pad surfaces.

Various spacer designs, spacer materials, and smooth or ribbed rods have been investigated in a simulated GCFR operational environment. Additional tests to investigate spacer contact surface geometry, surface roughness, and manufacturing techniques have resulted in specifications for spacer fabrication for optimum performance. Spacers fabricated by electrodischarge machining (reference technique) have been subjected to reproducibility tests in a typical GCFR environment. The effects of hydrogen/water content and dwell time between interacting relative motion on the friction and wear have also been investigated.

Reproducibility testing of the reference design hexagonal spacers was completed in FY-76. The hexagonal spacer design for a 12-rod cluster is shown in Figs. 2-10 and 2-11, and the cut-out spacer cells with the smooth rod are shown in Fig. 2-11. A summary report of the test is being prepared. During the FY-76 testing phase, a change of design was made to a modified hexagonal spacer. A 37-rod spacer using this design which was made for thermal-hydraulic testing in the AGATHE (EIR) loop is shown in Fig. 2-12. One of these spacers was obtained for rod/spacer interaction testing, and seven cells were cut out; a typical cell is shown in Fig. 2-13. A holder was fabricated, and two long-stroke tests were conducted in the rod/spacer interaction testing using smooth rods. The results were contradictory in that the first test resulted in friction and wear which was lower than that for the reference design hexagonal spacer. However, in the second test, the friction and wear were much higher. Careful dimensional measurements are being made on the tested and untested spacer cells before testing continues, and the spurious test results are being evaluated.

2.3.2. Component Tests

The conceptual design of blanket bundle assembly components was developed, and parts were ordered for fabrication. The blanket rods are wrapped with wire for spacing in the bundle assembly. An assembly of 61 rods will eventually be fabricated into a support plate to determine the problems associated with the assembly and the resulting stiffness of the bundle.

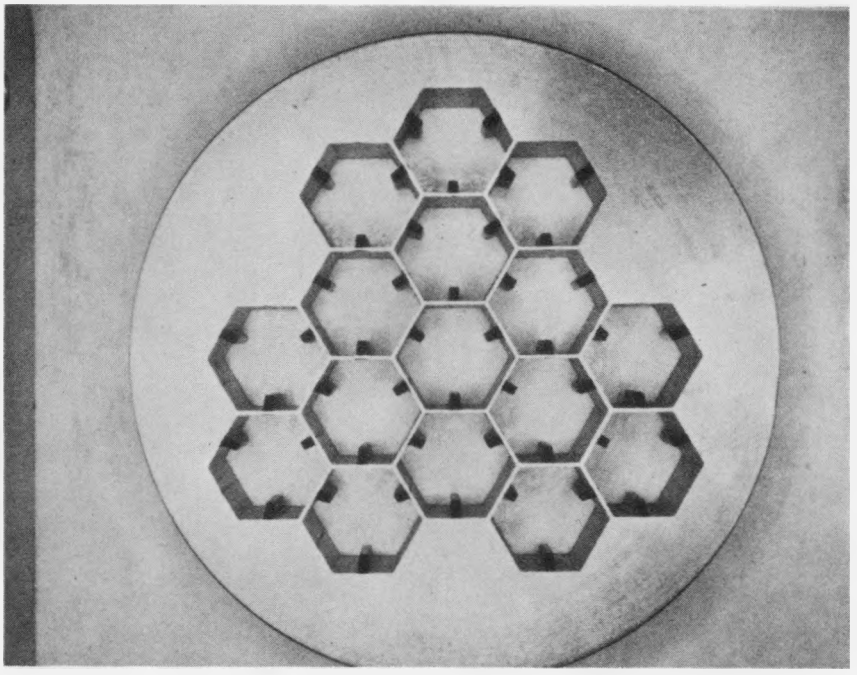

Fig. 2-10. Twelve-rod hexagonal spacer

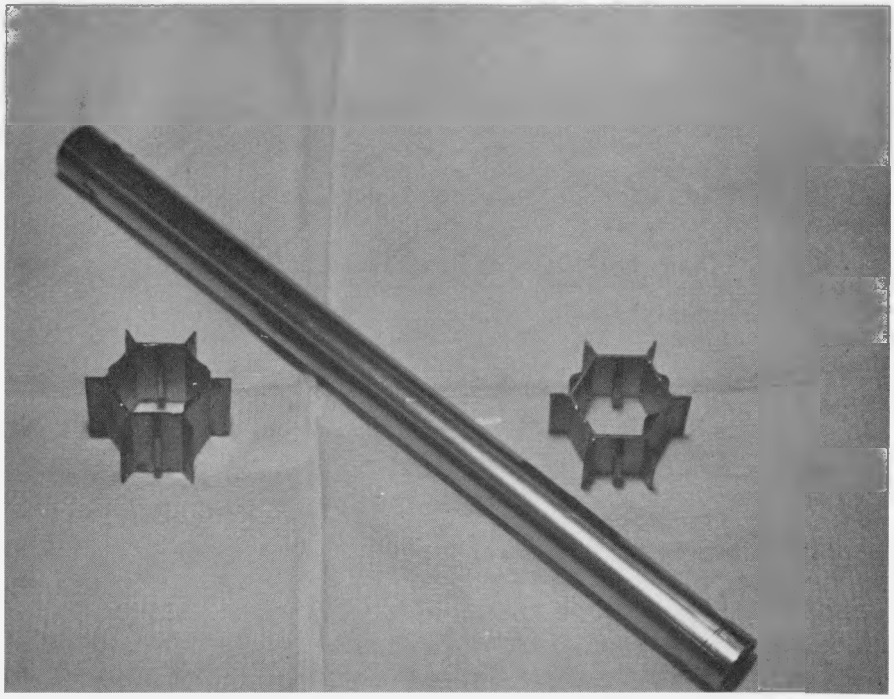

Fig. 2-11. Hexagonal spacer cells (from Fig. 2-10) with smooth rod

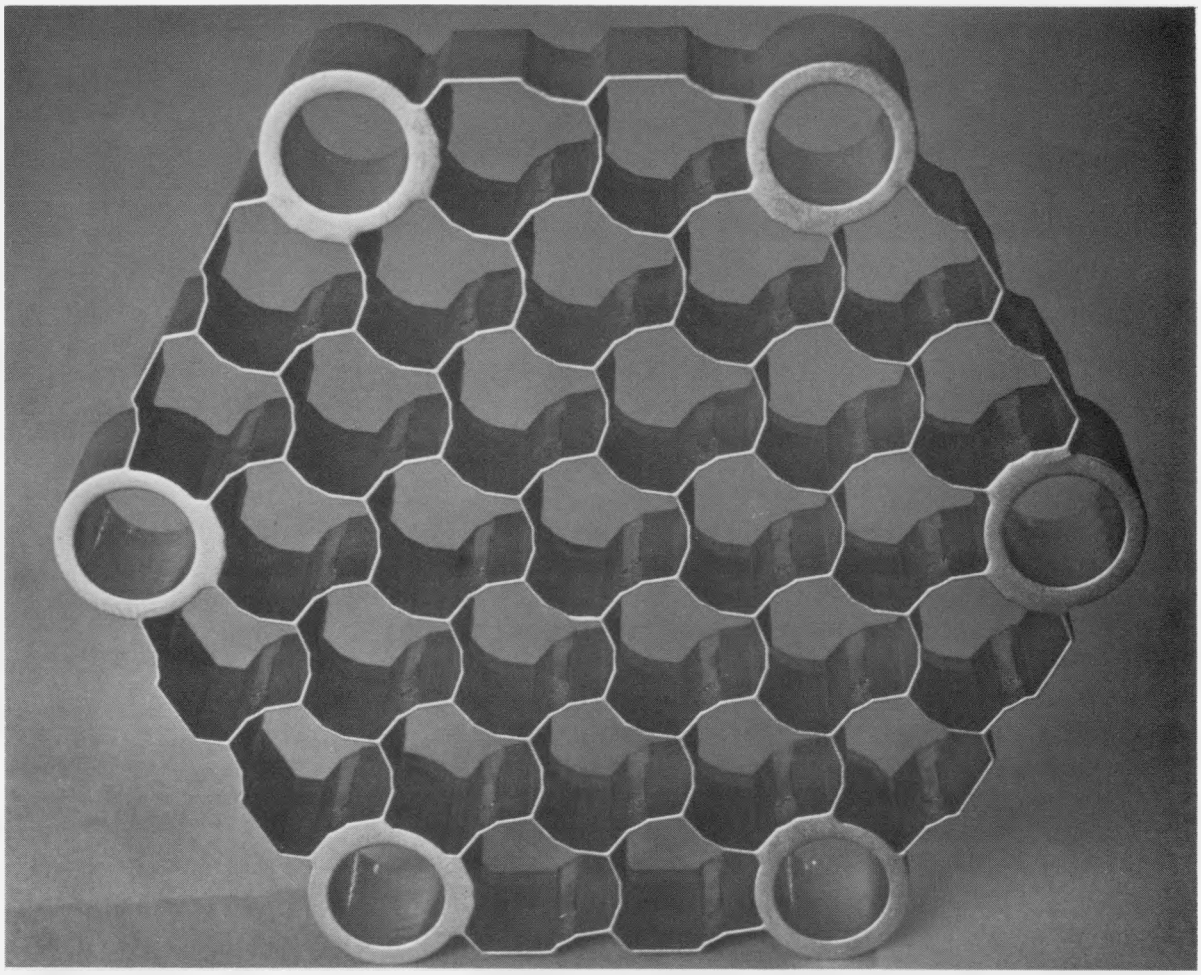

76G966-C

Fig. 2-12. Thirty-seven-rod spacer grid, modified hex design

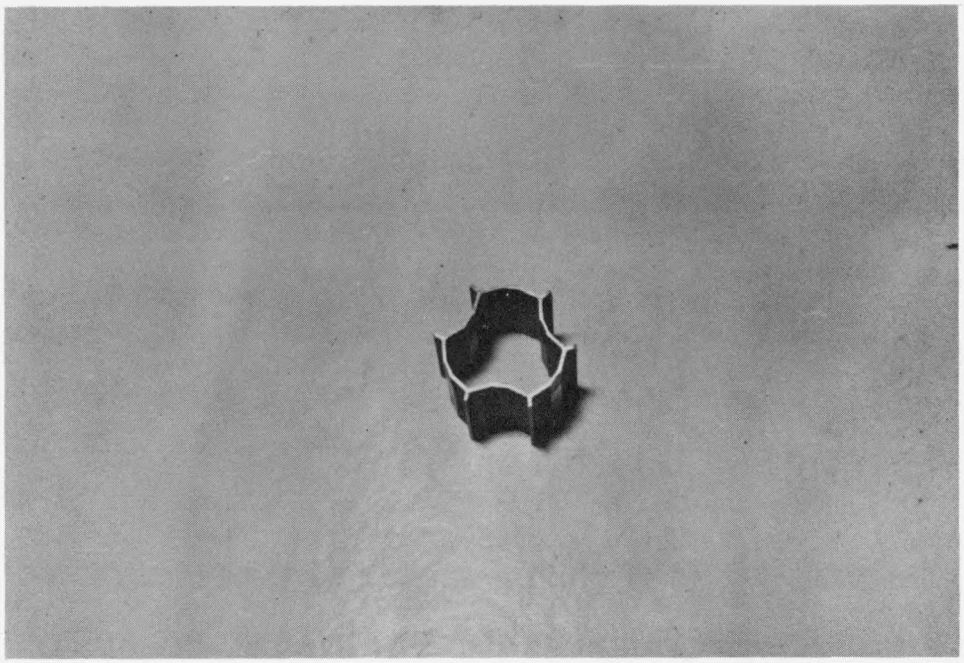

Fig. 2-13. Modified hex spacer cell for rod/spacer interaction test

The wire-wrapped rod design is shown in Fig. 2-14. The tubes, end plug material, and wire have been procured for two rod sizes and two reactor core designs.

Two of the fuel rod spacers with the modified hexagonal design shown in Fig. 2-12 were procured for structural testing. The spacers will be used in elastic load deflection tests for correlation with structural analysis. They may then be elastically distorted to determine structural limits. The tests are being planned.

2.4. CORE TEMPERATURE MONITORING

No work was done during the FY-76 transition quarter because of lack of funds. The work planned for FY-77 involves thermal analysis of the thermal probe and will be reported in the next quarterly report.

2.5. HEAT TRANSFER AND FLUID FLOW TESTING

The flow test assembly for the GCFR core assembly inlet nozzle was assembled with instrumentation by Experimental Engineering. The major subassemblies of the test mock-up are shown in Figs. 2-15 through 2-18. Figure 2-15 presents the upper fuel rod support grid and vent manifold assembled into the simulated hexagonal duct section; Fig. 2-16 shows the subassembly of Fig. 2-15 bolted to the inlet nozzle which contains the simulated grid shield and PES trap components; Fig. 2-17 shows the simulated upper inlet and assembly clamping section; and Fig. 2-18 presents the complete test assembly. The tests have been initiated and preliminary data at low flow have been obtained. The tests will be completed and data reduction accomplished during the next quarter.

The revised inlet nozzle design with new internal parts which simulate the shape of the redesigned grid shielding and the PES trap has been completed. The detail drawings are being reviewed, and fabrication will be completed during the next quarter.

1. WIRE MOUNTINGS IN LINE WITHIN 1 DEG
2. COMMERCIAL TUBE, 22.23 X 1.24 MM

   ASSEMBLY 1: TO 20.95 ± 0.02 MM O.D., 2153 ± 0.1 MM LENGTH;

   ASSEMBLY 2: TO 21.60 ± 0.02 MM O.D., 2153 ± 0.1 MM LENGTH

3. WIRE SIZE: ASSEMBLY 1 = ±0.025 MM; ASSEMBLY 2 = 1.4 ± 0.025 MM
4. WIRE WRAP 7 TURNS TOTAL, PULL THROUGH, WELD; WRAP AND WELD PROCEDURES TO BE DEVELOPED AND DOCUMENTED DURING ASSEMBLY OF FIRST 10 RODS

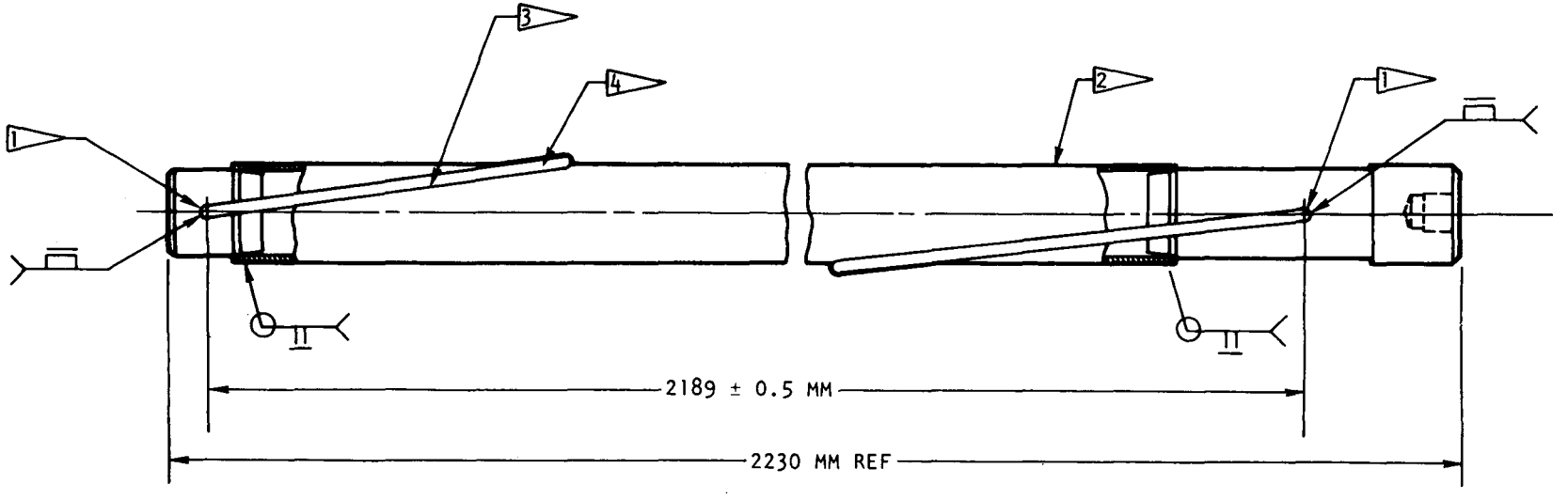

Fig. 2-14. Dummy blanket rod

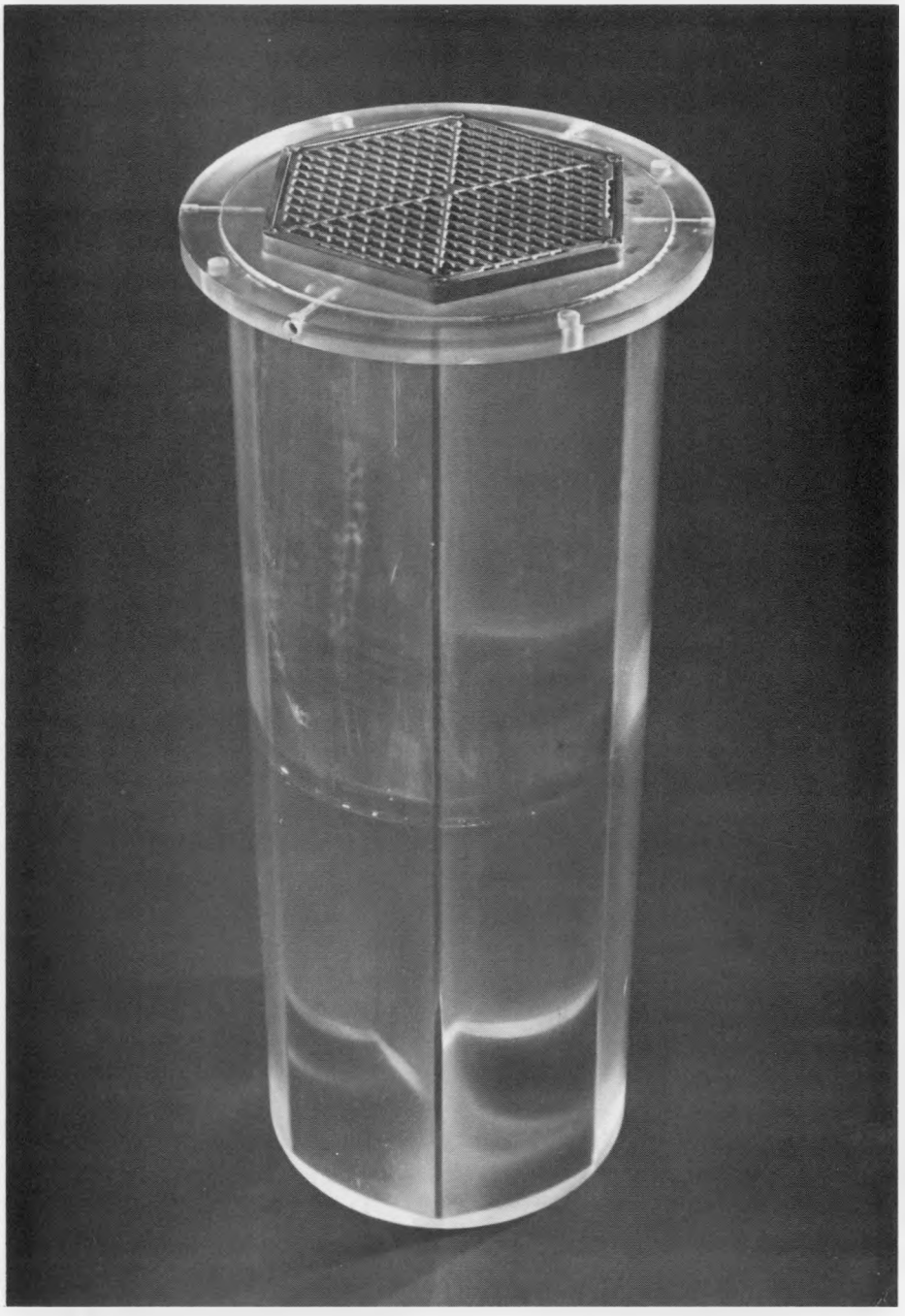

76G1606

Fig. 2-15. Fuel rod support grid and hexagonal duct section

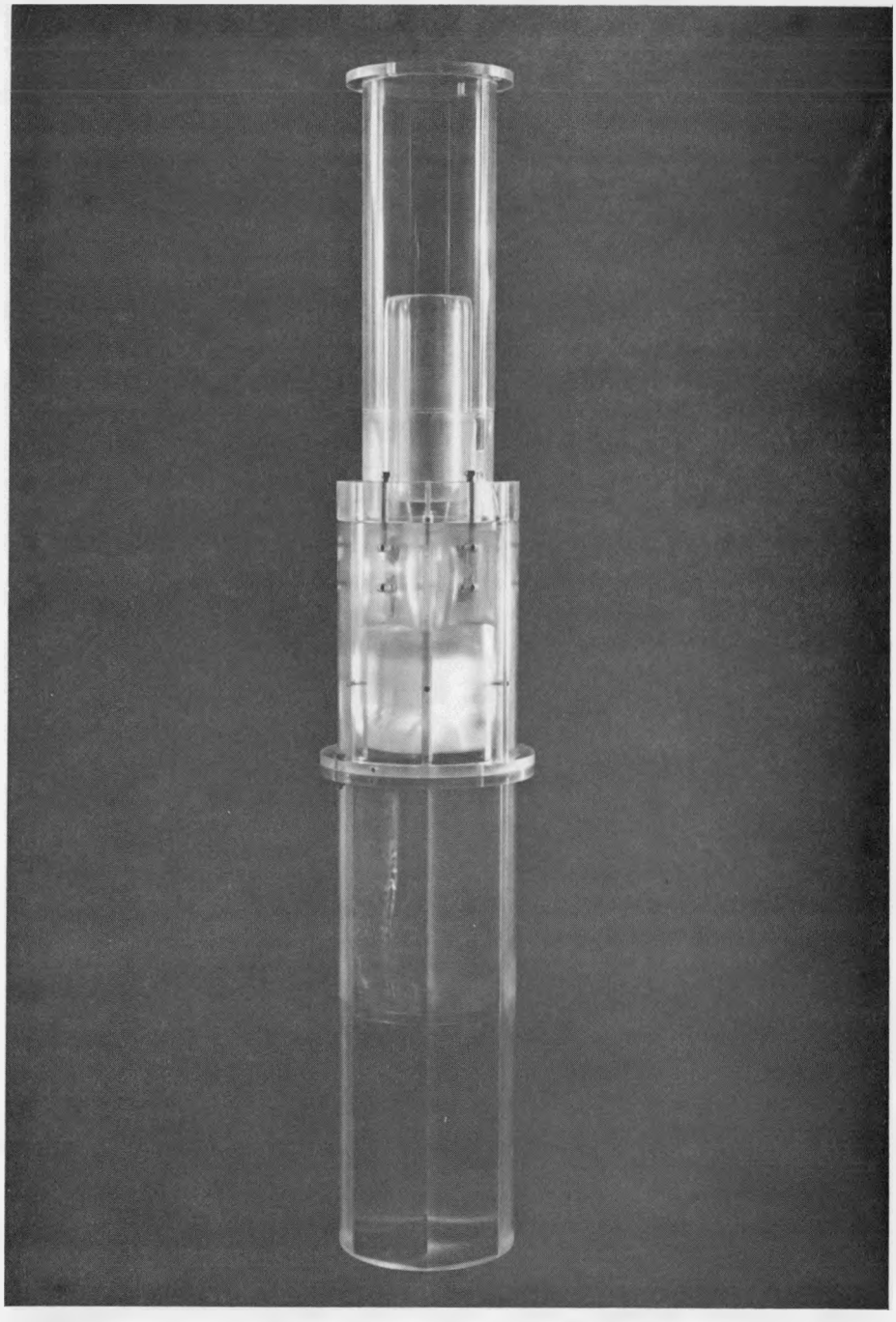

76G1605

Fig. 2-16. Inlet nozzle and grid shield components

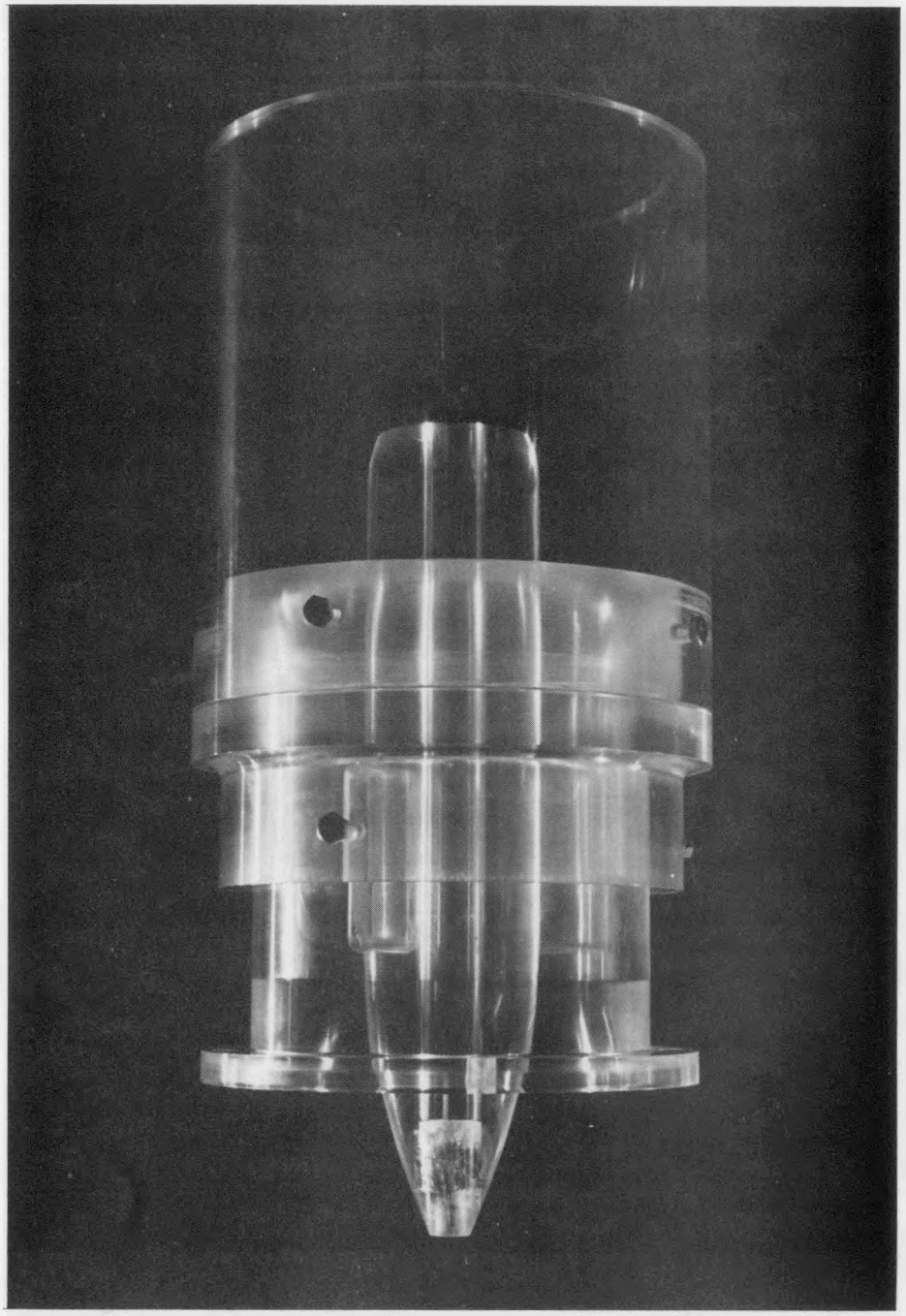

76G1609

Fig. 2-17. Upper inlet clamping section

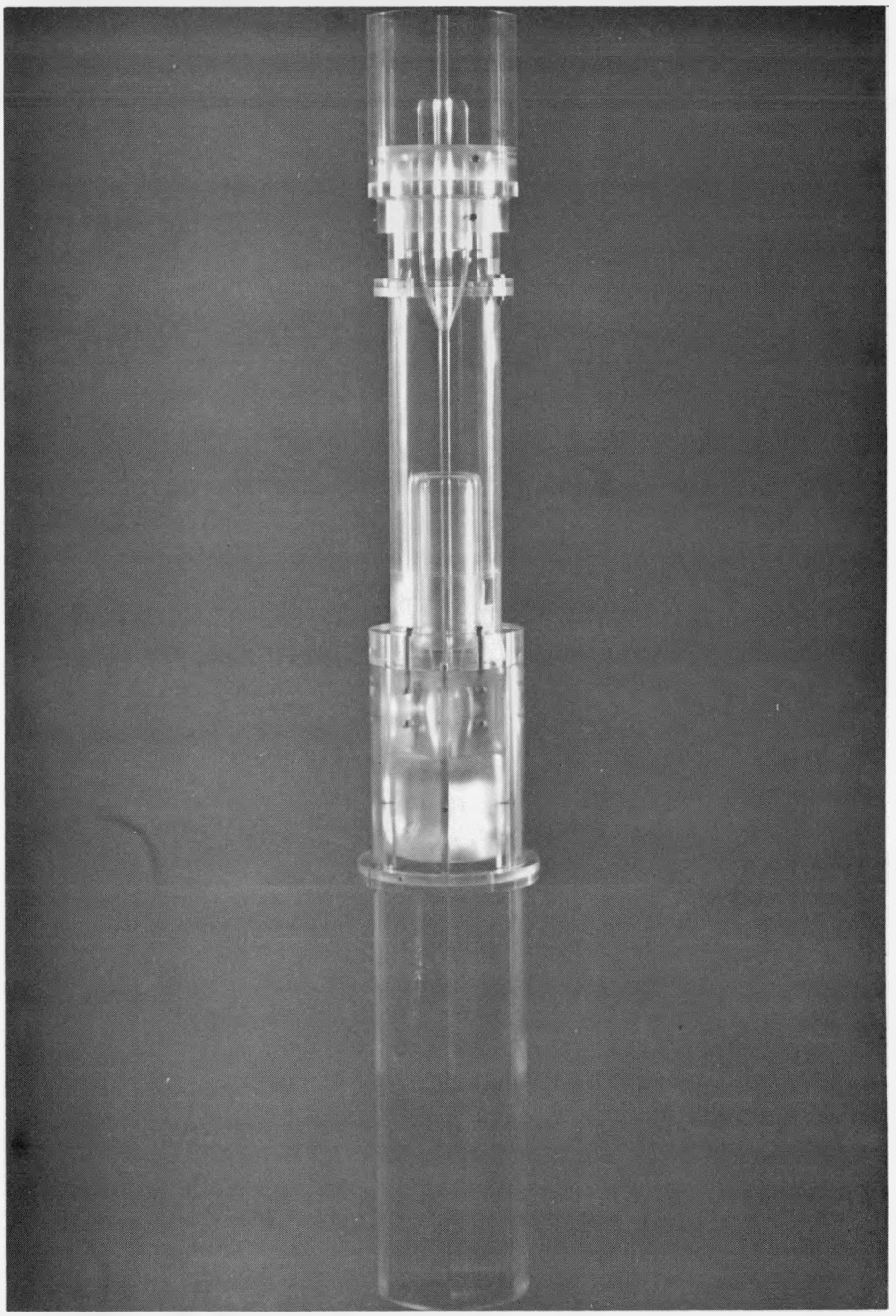

76G1611

Fig. 2-18. Flow test assembly

REFERENCES

2-1. "Gas-Cooled Fast Breeder Reactor Quarterly Progress Report for the Period May 1, 1976 Through July 31, 1976," ERDA Report GA-A13975, General Atomic, August 31, 1976.

2-2. Nathan, D. K., and M. Pirie, "On the Interpretation of Heat Transfer and Pressure Drop Tests on Roughened Rods in Smooth Circular Channels," Berkeley Nuclear Laboratories Report CEGB RD/B/N 1370, 1970.

2-3. Sparrow, E. M., A. L. Loeffler, and H. A. Hubbard, "Heat Transfer to Longitudinal Laminar Flow Between Cylinders," J. Heat Transfer 83, 415 (1961).

2-4. Novendstern, E. H., "Turbulent Flow Pressure Drop Model for Fuel Rod Assemblies Utilizing a Helical Wire-Wrap Spacer System," Nucl. Eng. Design 22, 19-27 (1972).

3. PRESSURE EQUALIZATION SYSTEM FOR FUEL (189a No. SU006)

3.1. FUEL ASSEMBLY AND VENT CONNECTION SEALS

The core assemblies (fuel, control, and blanket) in the GCFR are clamped at the conical surfaces of the assemblies to the matching surfaces in the grid plate with a force sufficient to support the assembly against side loading. The assemblies are cantilevered downward and must be sealed to the grid plate to limit the coolant flow bypassing the assemblies. The assembly vents must be connected and sealed to matching gas passages in the grid plate, and the seals must function at the coolant pressure difference between the reactor core inlet and exit plenums. The effectiveness of the seals over the life of the core is uncertain, not only because each assembly may be rotated several times over its useful life, but also because the seals must be effective in a high-purity, high-temperature helium environment while subject to mechanical, vibrational, and thermal effects. Most of the uncertainties are expected to be resolved in a two-part program: (1) a materials screening test program for the study of static adhesion of simulated fuel assembly and grid plate parts clamped together and (2) leakage tests of fuel assembly and vent connection seals to the grid plate. Current progress in these activities is described below.

3.1.1. Static Adhesion Tests

The first set of static adhesion tests was conducted in FY-75 on 316 and 304 stainless steel at various matching cone angles, contact loadings, and surface finishes. This was followed in FY-76 by a second set of tests using materials including couples of Inconel 718 - 316 stainless steel, Inconel 718 - 304 stainless steel, and 304 - 316 stainless steel. In FY-77, a third set of tests will be conducted to examine selected materials and processes for formation of hardened surfaces and their interface compatibility in the GCFR helium environment.

3.1.2. Fuel Assembly Ring Seal Leakage Tests

An alternative to the conical metal-to-metal core assembly seal design being developed uses piston rings as static sealing members. The test equipment, test grid parts, and core subassembly parts from the conical seal test have been modified, and the tests have been initiated. These tests include two ring designs provided by U.S. vendors (Stein Company and Dover Corporation) and one German design [Kraftwerk Union (KWU)]. The KWU design will be fabricated by KWU and one U.S. vendor for performance test comparisons. The piston ring designs are described below.

1. The Stein Company design is a 410 stainless steel single-piece seal ring with a step-cut joint.

2. The Dover Corporation design is a three-piece seal ring assembly; i.e., there are two outer rings and one inner ring. This ring assembly includes an axial wave spring and a radial (marcel) spring for assistance in applying ring contact loads. The backup springs may be unnecessary, as will be determined by testing. The design is fabricated from three materials: 410 stainless steel, Inconel 718, and S-Monel.

3. The KWU design is a double seal ring with straight-cut end joints. Each ring has a safety ring to prevent broken parts from falling out. The design is fabricated from Inconel 718.

Preliminary leakage tests of the Stein piston ring seals (Fig. 3-1) were conducted at room temperature. Three 410 stainless steel chrome-plated rings of the same design were tested. The test results are shown in Fig. 3-2. The test procedure for test No. 1 was to clamp the core subassembly test piece into the grid using a clamping load of 13,300 N and then increase the pressure differential. After reaching a ΔP of 340 KPa, the clamping load was reduced to zero. The leakage immediately decreased from 48 ℓ/min to 9 ℓ/min. The leakage was then measured as the ΔP was reduced by steps of 54 KPa down to a ΔP of 54 KPa, where it was about 4 ℓ/min, as shown

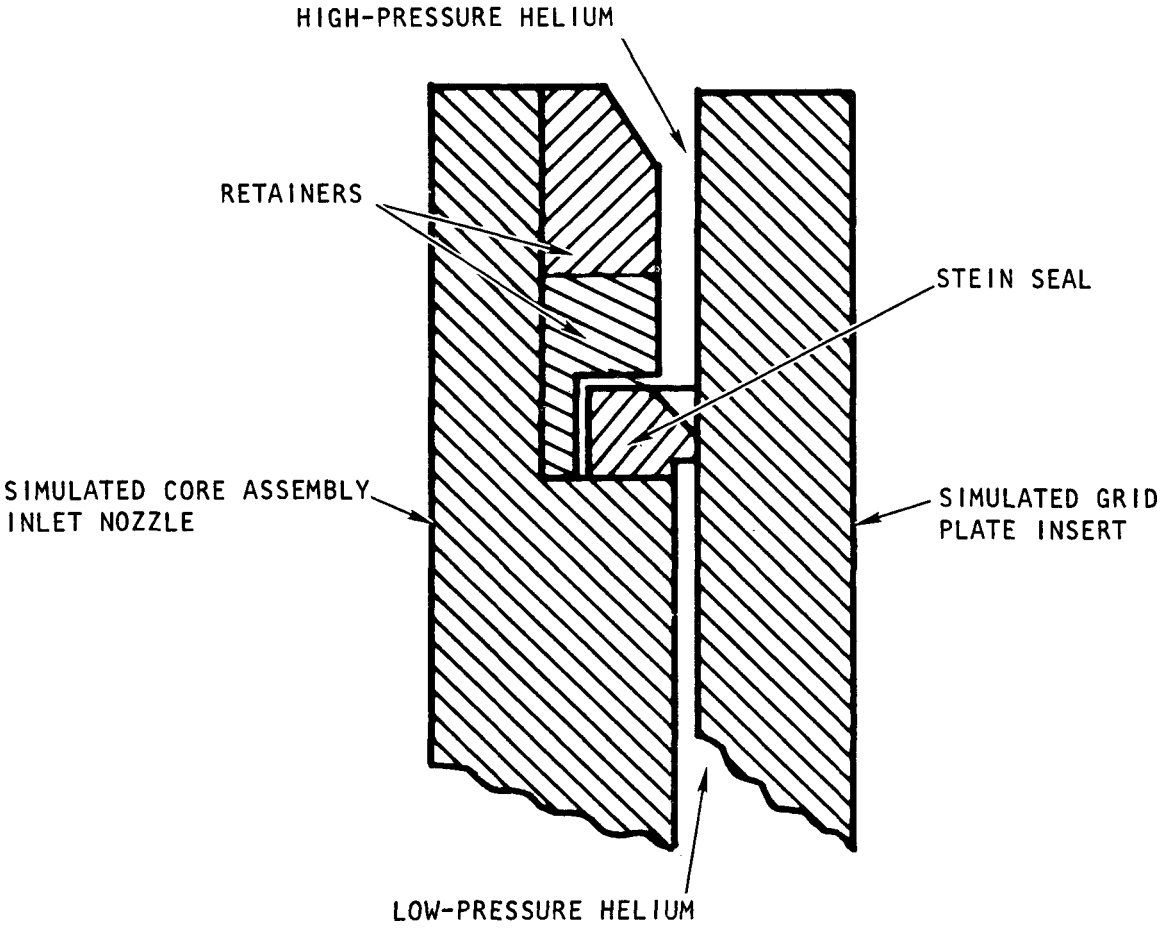

Fig. 3-1. Stein seal test

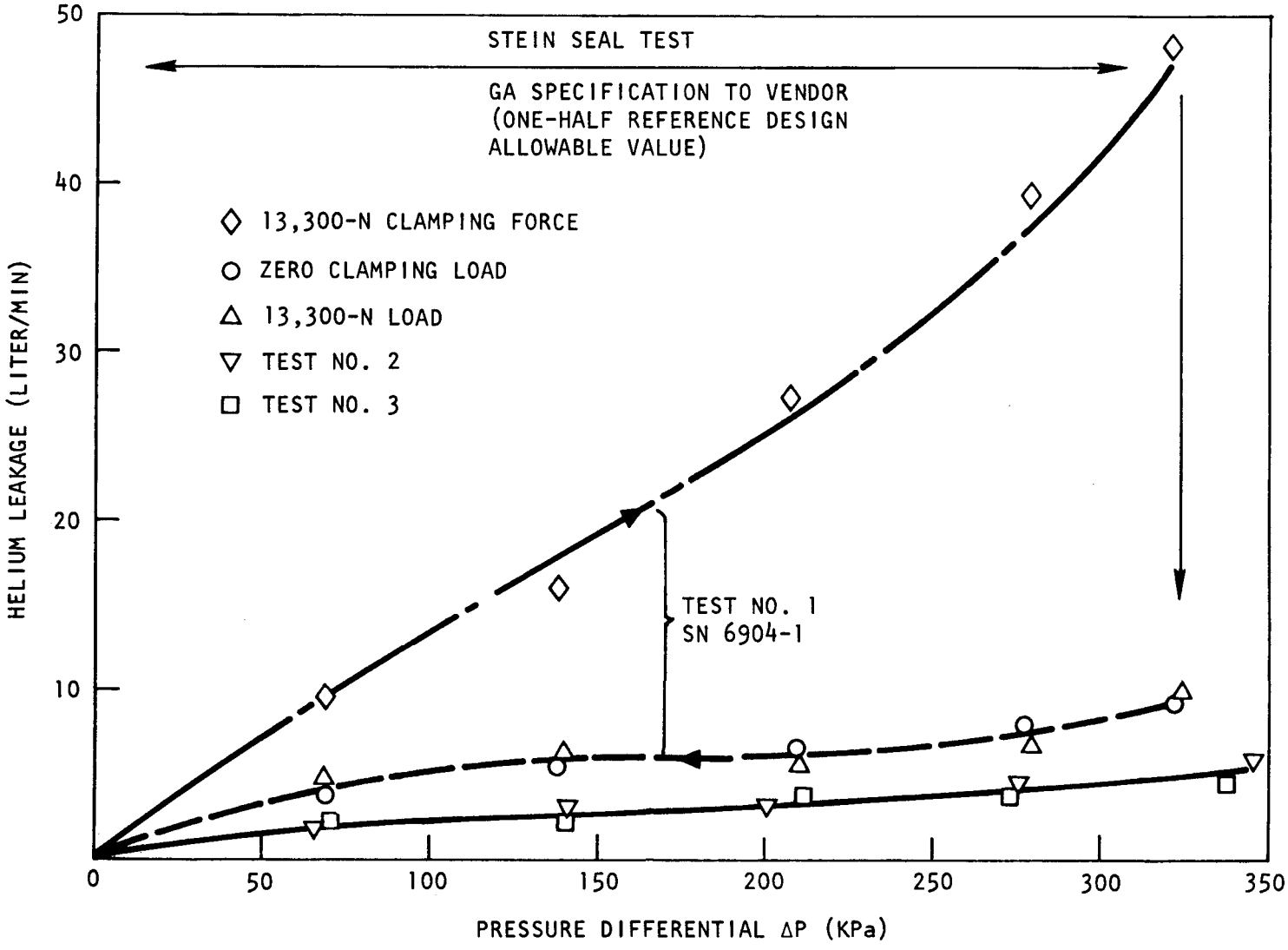

Fig. 3-2. Core assembly piston ring seal test

in Fig. 3-2. Next, a clamping load of 13,300 N was applied, and the ΔP was increased by steps of 54 KPa up to 350 KPa; the leakage was less than 9 ℓ/min at 350 KPa. Further clamping load changes only slightly affected leakage. The procedure used in subsequent tests (Nos. 2 and 3) of two different Stein piston rings was to increase pressure or ΔP to the maximum of ∿350 KPa at zero clamping force and then apply the clamping load. The results of these tests are shown in Fig. 3-2.

A conclusion which can be drawn from these tests is that the Stein seal rings meet GA design and purchase specifications at room temperature. Further leakage testing will be conducted with these rings at operating temperature after completion of room temperature testing. Testing of the Dover and KWU piston ring assemblies will be conducted at room temperature during the first quarter of FY-77.

3.1.3. Vent Assembly Seals

A vent assembly design concept is being developed for connecting the GCFR core subassembly vents to the passages in the grid plate and for sealing the core subassembly vents when the subassemblies are removed from the grid plate for handling, storage, and transport. Two design concepts (Figs. 3-3, 3-4) have been completed for installation of the vent assembly into the conical clamping surface of the fuel subassemblies. In Fig. 3-3, the vent assembly axis is located on a radial line perpendicular to the cone surface. A flat spot facing is machined on the cone surface to permit welding of the vent assembly into the core subassembly, and a mating spot facing is machined into the grid plate conical surface for seating of the seal. Vertical installation of the vent assembly in the conical surface is shown in Fig. 3-4. For testing purposes, the vent connection to the simulated grid plate part is made with a cylindrical tube screwed into the grid plate part with an O-ring seal. The vent connection torus in the vent assembly is then seated against the flat end of the tube in the grid plate test part.

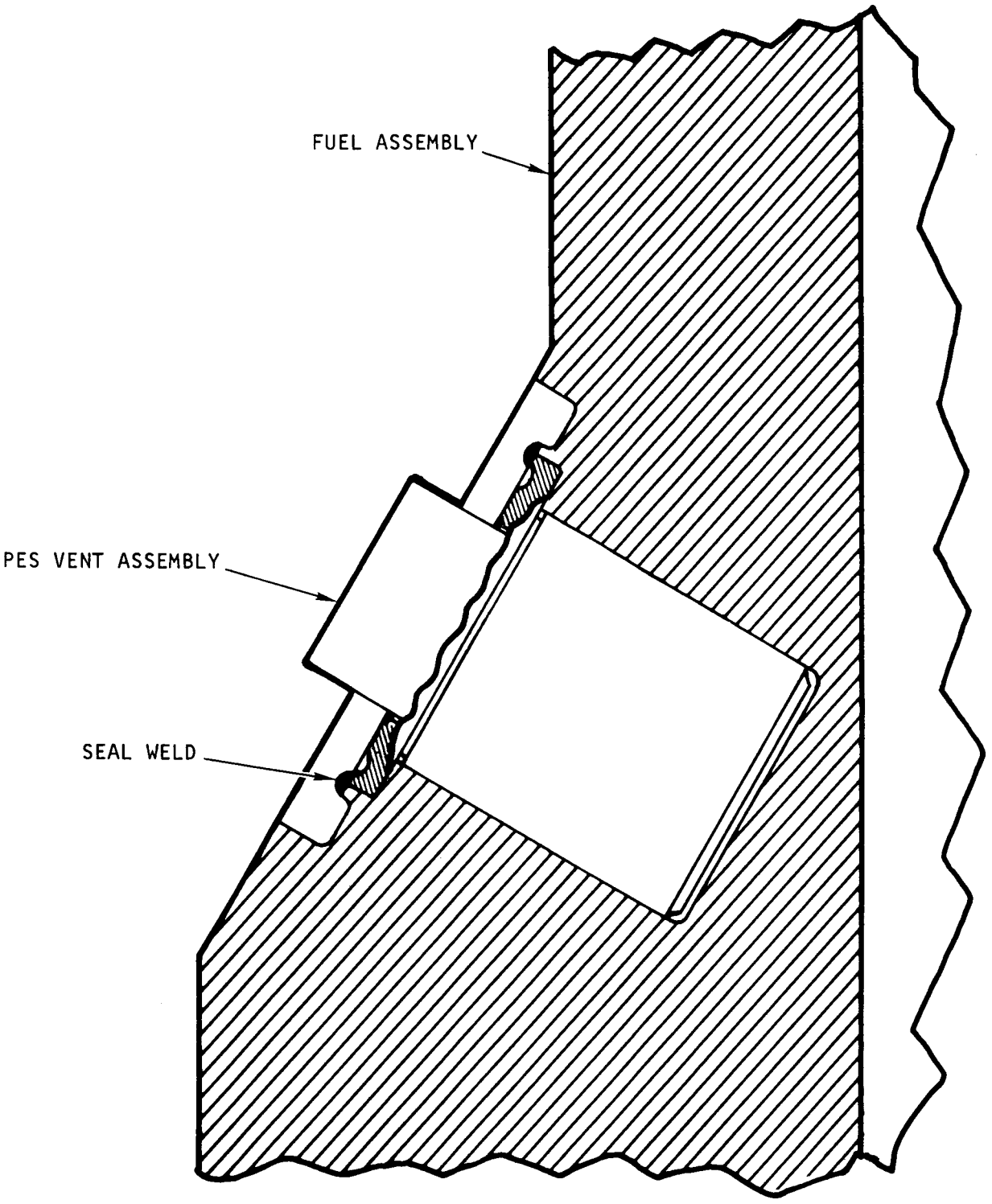

Fig. 3-3. PES vent assembly installation perpendicular to conical surface

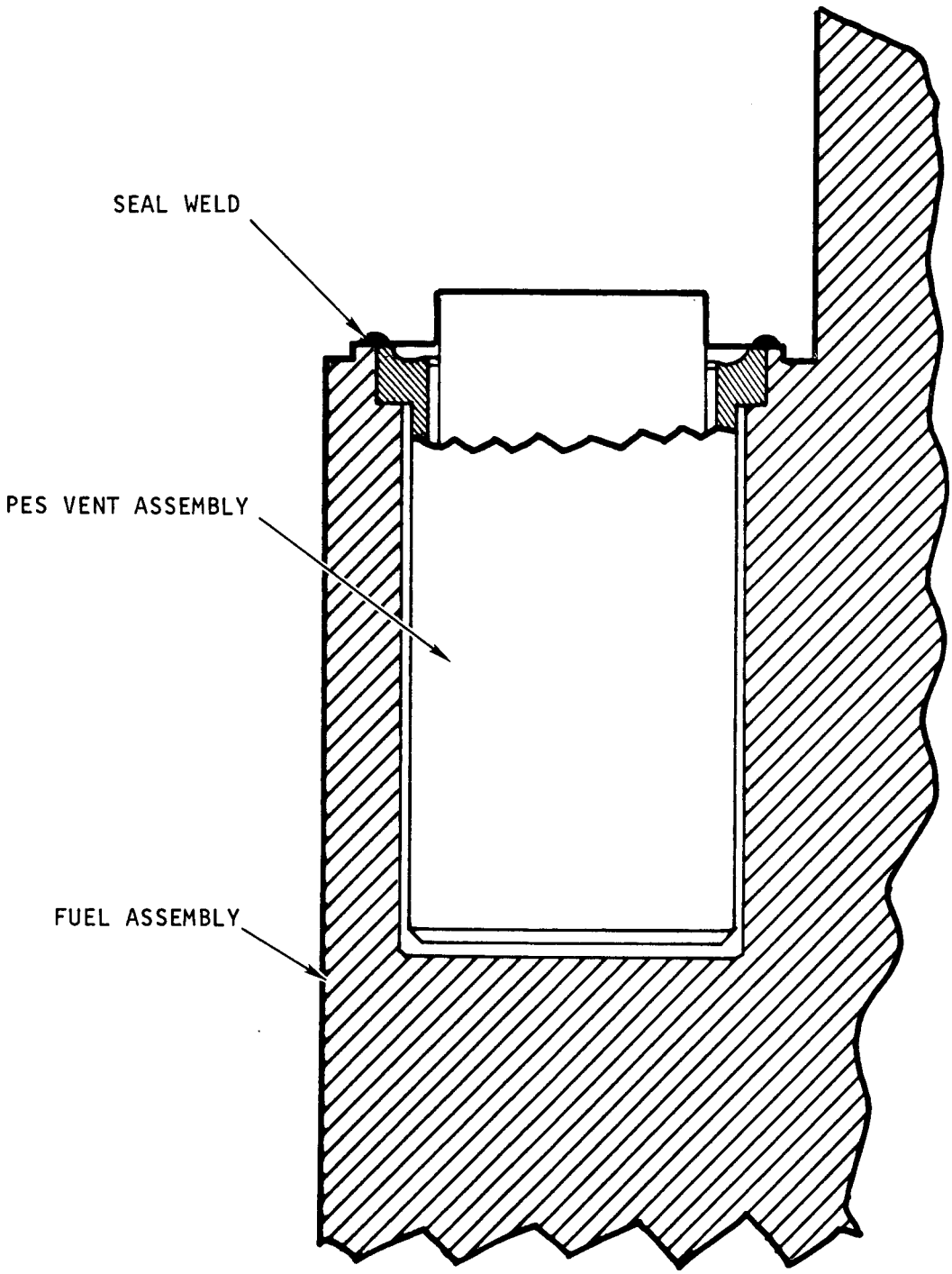

Fig. 3-4. PES vent assembly installation, vertical position

The vertical installation shown in Fig. 3-4 requires a smaller-diameter vent assembly compared with Fig. 3-3. The conceptual design of the assembly is shown in Fig. 3-5. The diameters of the assemblies in Figs. 3-3 and 3-4 are 15 and 11 mm, respectively. The design of the latter assembly requires smaller-diameter bellows and belleville springs. A bellows design was submitted to Servometer Corporation and the proper size bellows was fabricated using the electrodeposited nickel method. The belleville springs made of 17-7 PH stainless steel were procured from Associated Spring Corporation. The bellows and springs have been received and the design drawings completed. Fabrication of parts for the reduced-diameter assembly and laboratory testing of both assembly sizes will be completed during the next quarter. In addition, a plexiglass model of the connection of the core subassembly vents to the sweep gas passages in the grid plate is being fabricated.

3.2. ANALYSIS, MODELS, AND CODE DEVELOPMENT

The GCFR is designed with pressure-equalized and vented fuel and blanket assemblies. A PES is provided to perform these functions and contains one unit of the helium purification system (HPS). The PES previously described in Ref. 3-1 is a complex flow network consisting of manifolded fuel rods, fuel and blanket assemblies, monitor lines through which vented fission gases are swept by inflowing coolant, the HPS unit, and check valves leading to the suctions of the main and auxiliary circulators which power the system. The HPS unit contains two parallel trains of filters, heaters, and coolers. Only one train is in service at any time.

During this quarter, modeling and computer code development for design and transient analysis of the PES flow network continued. The code for the PES/HPS simulation which was developed last quarter was checked out by running a number of small test cases. Once satisfactory performance of the code was obtained, simulation of the actual GCFR PES/HPS was initiated.

At present, the HPS unit to be connected to the PES network is envisioned to be identical to the Fort St. Vrain HTGR HPS except that the

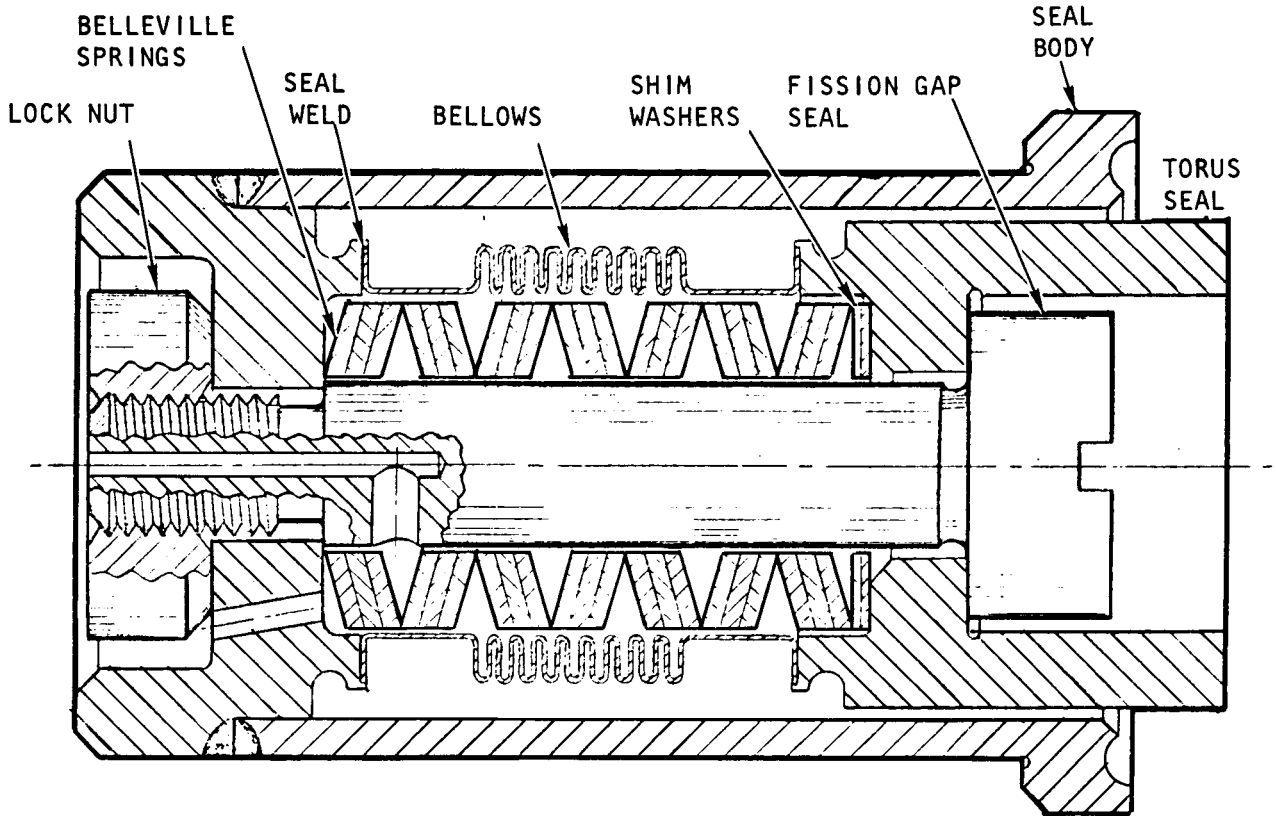

Fig. 3-5. PES vent assembly for vertical installation

GCFR HPS will not incorporate its own circulator to drive the system, but instead will rely on the main and auxiliary helium circulators of the coolant system. Drawings of the Fort St. Vrain HPS components were reviewed to determine the gas volumes of the components (see Table 3-1) and to estimate their pressure drops. Using these data and drawings of the core assemblies and the PES network, an analytical model of the GCFR PES/HPS was developed. This model contains 47 coupled, highly nonlinear differential equations. Initial runs with the model have met with numerical difficulties, which may be the result of the complexity of the network or the very small volumes involved in the short flow lines between nodes in the PES. Debugging of the model and the code is continuing.

3.3. PLATEOUT AND PLUGGING

Volatile fission products, particularly cesium and iodine, vented from the core assemblies and produced by gaseous precursor decay of fission products vented from the core assemblies may plate out on the walls of the monitor lines. These fission products are swept through the monitor lines into the HPS traps by helium entering at the core subassembly vent connections. Accumulation of deposited material may constrict the sweep gas flow passages and could potentially lead to plugging of the lines. The conditions under which plateout and plugging could occur in the GCFR, the means of minimizing or eliminating it, and the methods for removing deposits are being investigated. A small high-pressure loop has been built and is being used for this purpose. Development of components for injection, control, and measurement of impurities in the helium (i.e., H_2 and H_2O) and sources for simulating venting of the volatile fission products and their compounds is being examined.

3.3.1. High-Pressure Loop

Liquid-nitrogen-cooled charcoal traps were fabricated and installed in the high-pressure loop supply line. The traps were activated and their behavior characterized with regard to hydrogen breakthrough and oxygen removal. The cleanup system and loop were pressurized (8.6 MPa) and

TABLE 3-1
ESTIMATED PES COMPONENT VOLUMES

HPS Component	Description	Volume (m^3)	(%)
A2301	High-temperature filter adsorber	0.56	12
E2301	Helium purification cooler	0.41	9
A2303	Helium purification dryer	0.35	8
E2203	Low-temperature heat exchanger	0.40	9
A2305	Low-temperature adsorber	0.48	11
F2301	Purified helium filter	0.53	12
E2307	Hydrogen removal economizer	0.12	3
A2309	Hydrogen getter	0.09	--
F2304	Hydrogen removal filter	0.52	12
	Subtotal HPS	3.46	77
	91 fuel subassemblies	0.337	8
	27 control subassemblies	0.089	2
	90 blanket subassemblies	0.594	13
	Core assembly subtotal	1.02	23
	144 monitor lines	0.02	--
	Total PES gas volume	4.50	100

tested for leaks, and a number of leaks were found and fixed. Installation of the oxygen potential analyzer with the reference gas sleeve (currently out for repair) has been delayed (Section 3.3.2).

3.3.2. Oxygen Potential Analyzer

During the previous quarter (Ref. 3-1), the effect of an inherent oxygen leak into the oxygen potential analyzeer cell was discussed. Chromatographic analysis of the effluent gas from the cell revealed that this leak did exist and was of the order of magnitude to cause the deviations from linearity previously observed in the plot of log (H_2/H_2O) versus electromotive force. The leak was traced to the cell seal made of a silicone rubber adhesive material (the ThO_2 and ZrO_2 cells used incorporate this type of sealant). This material is notoriously permeable to oxygen. Before the leak could be satisfactorily eliminated, the cell being tested failed because of a faulty connection and had to be returned to the manufacturer for repair. Another oxygen potential analyzer from a different manufacturer was employed. This device uses a silicone rubber O-ring to seal the cell (ZrO_2, air reference), and the same type of oxygen permeation leak was found. However, when the original O-ring was replaced with a Viton O-ring, the permeation leak (O_2 and N_2 from the atmosphere) was eliminated. A study is now under way to evaluate what appears to be an electrochemical leak in this cell. This leak allows some oxygen ingress to the sample gas without concomitant transport of nitrogen (thus eliminating the possibility of a porous or permeation leak).

3.4. PES MANIFOLD FABRICATION

The following manifold fabrication efforts have been accomplished during this quarter:

1. Diffusion bonding of coupons to establish bonding parameters.

2. Bonding of one-third segment manifold samples.

3. Auger spectroscopy to establish the effect of impurities in the GCFR helium atmosphere on the behavior of the manifold material.

4. Overcheck chemical analyses of the full-size manifolds which were vacuum investment cast by Arwood.

5. Preparation of a summary topical report on manifold fabrication development.

In order to improve the quality of the diffusion bonding, several 645-mm coupons with fission passage grooves were bonded under a variety of conditions to select parameters for improved bonding. The conditions are given in Table 3-2. The results showed that a bonding pressure of 45 MPa and a temperature of 900°C for 2 hr were required to effect satisfactory diffusion bonding of the coupons. Two one-third segment manifolds were then diffusion bonded at DWA Composites under the conditions listed in Table 3-3.

Overcheck chemical analysis of the full-size manifolds vacuum investment cast by Arwood was obtained, and the results indicated that the chemistry was within specification.

REFERENCE

3-1. "Gas-Cooled Fast Breeder Reactor Quarterly Progress Report for the Period May 1, 1976 Through July 31, 1976," ERDA Report GA-A13975, General Atomic, August 31, 1976.

TABLE 3-2
DIFFUSION BONDING CONDITIONS AT GA

Atmosphere Inside Bonding Retort	Temperature (°C)	Compressional Stress (MPa)	Time (hr)	Results
Vacuum[a]	700	69	4	No bond
Vacuum[a]	800	69	1	Partial bond
Vacuum[a]	900	69	1	Excellent bond
Vacuum[a]	900	45[b]	2	Satisfactory bond
He + 3% H_2	900	45[b]	2	Unevenly loaded and nonuniform deformation; excellent bond on one side of the specimen, other side was unsatisfactory

[a]Evacuated to 10^{-3} Pa at 350°C and sealed.

[b]45 MPa was chosen to stay well below the strength limit of the ceramic plates in the bonding press at DWA.

TABLE 3-3
DIFFUSION BONDING CONDITIONS AT DWA

Atmosphere Inside Bonding Retort	Temperature (°C)	Compressional Stress (MPa)	Time (hr)	Results
Vacuum	950	90 to 99	2	Excellent bond but excessive deformation
Vacuum	900	69	2	Results not yet available

4. CORE FLOW TEST LOOP PROGRAM (189a No. SU006)

A series of out-of-pile simulation tests will be performed to (1) demonstrate the ability of the GCFR fuel, control, and blanket assembly designs to meet design goals and (2) verify predictions of analytical models which describe design operation and accident behavior. The test emphasis will be on obtaining thermal-structural data for steady-state, transient, and margin conditions using electrically heated rod bundles in a dynamic helium loop. The requirements include testing in the range of cladding melting and determining the consequences of local initiation of melting. The core flow test loop (CFTL) program plan (Ref. 4-1) presents the requirements for the test program to be conducted in the CFTL, which will be constructed and operated by Oak Ridge National Laboratory (ORNL). The principal work accomplished during this quarter was as follows:

1. CFTL operating requirements were reviewed and discussed with ORNL, and a technical basis for proceeding with the loop design was agreed upon.

2. A preliminary CFTL design for a 37-rod test bundle was completed and reviewed.

3. CFTL test performance predictions were completed for steady-state preliminary tests P-1 and P-2.

4. Possible loops for testing the prototype core assembly were evaluated, including an ongoing study on refurbishing the experimental beryllium oxide reactor (EBOR) equipment at Idaho Nuclear Engineering Laboratory (INEL).

4.1. PROGRAM PLANNING

4.1.1. Program Plan

During the previous quarter (Ref. 4-2) a draft revision to the CFTL program plan (Ref. 4-1) was issued for review and comment. All internal and ORNL comments are being evaluated, and the draft will be revised as appropriate. Specific revisions will be made as follows: (1) the difference between the generic loop performance, the loop design envelope, and the specific test parameters for the evolving GCFR core designs will be clarified, (2) the current reference fuel, control, and blanket assembly design will be illustrated in the plan if drawings are available, (3) a single-priority, one-test series which reflects the impact of replacement of six fuel rods with grid spacer tie rods will be defined, and (4) there will be more emphasis on the major program objective of performing structural-thermal-flow interaction tests.

4.1.2. CFTL Performance Requirements

The CFTL basic performance requirements have been given to ORNL so that the CFTL loop will meet the GCFR test requirements. The primary source of this information is Ref. 4-1 supplemented by a draft revision to the plan, meeting agreements, and internal GA memos. Recent GCFR design changes have resulted in change of the core design parameters, and consideration was given to changing the CFTL performance requirements. After reviewing these changes and the probability of further changes, it was agreed that the CFTL should be designed for a fixed set of performance requirements which will provide a CFTL operating envelope which encloses present and probably future desired test operations. Table 4-1 presents the GA-ORNL CFTL steady-state operating envelope; this is approximately the same as the parameter in the Ref. 4-1.

TABLE 4-1
CFTL STEADY-STATE OPERATING ENVELOPE

Coolant	Helium[a]
System pressure (MPa)	
Nominal	9.0
Minimum	0.10
Maximum	10.3
Test section	
Fuel assembly ΔP (kPa)	
Nominal	307 (at 9.0-MPa system pressure)
Fuel assembly ΔP/P	0.034
Inlet temperature (°C)	
Nominal[b]	350
Minimum[b]	325
Maximum[c]	350
Outlet temperature (°C)	
Nominal[b]	545
Maximum[b] (normal)	595
Maximum flow per rod (g/s)	30
Maximum power per rod (kW)	
Fuel	38
Blanket	45
Test section space envelope	
Total length (mm)	3000
O.D. (mm)	300

[a] With controlled and measured trace impurities.

[b] At maximum flow and power.

[c] Limited by helium circulators, not pressure boundary.

4.2. TEST ANALYSIS AND PREDICTION

4.2.1. Prediction Code TSPEC

The computer program TSPEC was developed to provide a relatively simple, approximate analysis for predicting the performance of GCFR model core assemblies in the CFTL. The principal simplification is to neglect cross flow within the bundle. The test specifications will list the steady-state and transient input parameters, including the time functions of power and flow for each test run; TSPEC will predict the resultant test parameters. The code performs four types of calculations:

1. Geometric bundle data.

2. Geometric bundle data and prediction of N steady-state runs.

3. Geometric bundle data and prediction of a series of steady-state runs, with linear interpolation between the first and last input values.

4. Geometric bundle data and N transient runs.

A topical report (Ref. 4-3) is being prepared in which the structure of the code is explained and the following user information is provided: input instructions, sample calculations, code listing, and index of code variables.

4.2.2. Performance Prediction for Tests P-1 and P-2

Test performance has been predicted for the steady-state tests listed below. The specific test conditions are listed in a Ref. 4-4, and the analysis was performed with TSPEC.

Test No.	Description
1.1.1	Flow only, 110% to 10%
1.1.2	Flow only, 10% to 1%

Test No.	Description
2.1.1	Uniform power, 110% to 10% power and flow
2.1.2	Overcooling, 100% flow, 100% to 10% power and flow
2.1.3	Afterheat, 10% to 1% power and flow
2.1.4	Afterheat, 10% to 1% power and flow, pressure = 0.2 MPa
2.1.5	Intermediate pressure level, 30 MPa
2.2.1	Skewed power, 0.5 kW per row
2.2.2	Skewed power, 1.0 kW per row
2.2.3	Skewed power, 1.5 kW per row
2.2.4	Skewed power, afterheat
2.2.5	Skewed power, afterheat, pressure = 0.2 MPa
2.3.3	Single heated rod, operating flow range
2.3.4	Single heated rod, afterheat flow range

The predictions for 143 test runs have been completed and entered into the CFTL data file. Sample predictions are included in Refs. 4-2, 4-4, and 4-5.

The results of a single heated rod calculation are given in Table 4-2. Although the simplified analysis does not treat cross-flow mixing, Table 4-4 gives the limiting possibilities of complete mixings, identified as average values, and no mixing, identified as maximum values. Because the limits show large temperature differences, the actual test results should be a relatively sensitive measurement of cross-flow mixing.

4.3. TEST SPECIFICATION

Comments were received from ORNL on the test specification draft described in Ref. 4-4 for the preliminary series of tests on models of test assemblies with fuel rod simulators. It has been determined that there is a need for generic CFTL test requirements which provide the operating envelopes for power, coolant flow, and pressure and the temperature parameters for the test program. The test specification draft will list proposed details for specific test runs.

TABLE 4-2
CFTL TEST SPECIFICATION FOR TEST P-2-3-3

BUNDLE DESIGN
BUNDLE TYPE - FUEL
BUNDLE IDENTIFICATION - C

BUNDLE DATA
RODS PER BUNDLE = 37. HEATED = 1. UNHEATED = 36.
BUNDLE OD = 83.4 MM
DUCT WALL THICHNESS = 2.500 MM
BUNDLE FLOW AREA = 2393. MM**2
DUCT PERIMETER = 235.20 MM
AVG BUNDLE HYDRAULIC DIAMETER = 8.67 MM

ROD DATA
ROD DIAMETER = 7.48 MM
ROD PITCH = 11.20 MM
HEIGHT OF ROUGHENING = .140 MM
PITCH OF ROUGHENING = 1.68 MM
FLOW AREA PER ROD = 64.69 MM**2
H T PERIMETER PER ROD = 23.50 MM
LOCAL HYDRAULIC DIAMETER = 11.01 MM
UPPER BLANKET LENGTH = 655.0 MM
HEATED LENGTH = 1130.0 MM
LOWER BLANKET LENGTH = 450.0 MM
TOTAL LENGTH = 2235.0 MM

ROUGHENING DATA
ROUGHENED FRACTION OF HEATED LENGTH = .765
ROUGHENED LENGTH = 864.4 MM
FRICTION FACTOR MULTIPLIER = 4.40
HEAT TRANSFER MULTIPLIER = 2.30
REFERENCE REYNOLDS NO = 100000.

SPACER AND FLOW COEFFICIENT DATA
NUMBER OF SPACER = 10.
SPACER COEFFICIENT = 1.372
SPACER SOLIDITY = .145
INLET COEFFICIENT = 1.000
OUTLET COEFFICIENT = .500

HEATER AXIAL POWER PROFILE
AXIAL QMAX/QAVG = 1.210
QX/QMAX = COS(1.049*(2*X/L - 1))

X/L	QX/QMAX
.000	.4984
.100	.6681
.200	.8084
.300	.9133
.400	.9781
.500	1.0000
.600	.9781
.700	.9133
.800	.8084
.900	.6681
1.000	.4984

TABLE 4-2 (Continued)

```
STEADY STATE TEST SERIES                    NO. OF RUNS -  1
                          POWER      FLOW
  SERIES FACTOR - (1)    1.000     1.000
  SERIES FACTOR - (2)     .100      .100

INPUT PARAMETERS FOR TEST RUN -   1
  TOTAL BUNDLE HEAT INPUT =  30.000 KW
  AVG POWER PER ROD = 30.000 KW
  MAX POWER PER ROD = 30.000 KW
  MIN POWER PER ROD = 30.000 KW
  MAX POWER DENSITY =  321.2 W/CM
  FLOW PER BUNDLE =  .7500 KG/SEC
  HELIUM INLET TEMPERATURE =  350.0 C
  HELIUM INLET PRESSURE =  9.000 MPA

THERMAL OUTPUT PARAMETERS
  AVERAGE BUNDLE OUTLET TEMPERATURE =  357.7 C      TEMPERATURE RISE  =    7.7 C
  OUTLET TEMPERATURE - AVG POWER ROD =  635.1 C      TEMPERATURE RISE  =  285.1 C
  OUTLET TEMPERATURE - MAX POWER ROD =  635.1 C      TEMPERATURE RISE  =  285.1 C
  OUTLET TEMPERATURE - MIN POWER ROD =  635.1 C      TEMPERATURE RISE  =  285.1 C
  MAX SURFACE TEMPERATURE =  698.3 C
  MAX SURFACE TEMPERATURE AT X/L =  .930
  SMOOTH ROD H. T. COEF.( X/L =  .234 ) =  4404. W/M*M/C     FILM DROP =  273.6 C
  ROUGHENED ROD H. T. COEF.(X/L =  .500 ) = 11074. W/M*M/C     FILM DROP =  128.2 C
  ROUGHENED ROD H. T. COEF.(X/L =  .930 ) = 11469. W/M*M/C     FILM DROP =   76.8 C

FLOW OUTPUT PARAMETERS
  AVG. BUNDLE RE =  83262.    LOCAL RE =  82775.
  BUNDLE PRESSURE DROP
    INLET =  7.512 KPA
    UPPER BLANKET =  10.828 KPA
    SMOOTH CORE LENGTH =  4.449 KPA
    ROUGHENED CORE LENGTH =  61.435 KPA
    LOWER BLANKET =  7.642 KPA
    ACCELERATION LOSS =  .094 KPA
    SPACERS LOSS =  20.704 KPA
    OUTLET LOSS =  3.852 KPA
  TOTAL BUNDLE PRESSURE DROP = 116.516 KPA

THERMAL EXPANSION PARAMETERS
  THERMAL INPUT     AS FABRICATED          TEST TEMPERATURES
                                          DUCT      ROD     DIFFERENTIAL
    AVERAGE            2235.0          2253.3    2255.3       2.0 MM
    HOTTEST            2235.0          2253.3    2255.3       2.0 MM
    COLDEST            2235.0          2253.3    2255.3       2.0 MM
  MAX BOW DISPLACEMENT =  .0 MM
  DIAMETRAL CLEARANCE =  83.4 MM
  MINIMUM DIAMETRAL CLEARANCE =  83.4 MM
```

TABLE 4-2 (Continued)

STEADY STATE RUN - 1

AXIAL PRESSURE, POWER, AND TEMPERATURE VALUES

LOCATION	X MM	X/L	DP KPA	AVERAGE POWER W/CM	AVERAGE HELIUM C	AVERAGE CLAD C	MAXIMUM POWER W/CM	MAXIMUM HELIUM C	MAXIMUM CLAD C	MINIMUM POWER W/CM	MINIMUM HELIUM C	MINIMUM CLAD C
INLET	.0		7.512	.0	350.0	350.0	.0	350.0	350.0	.0	350.0	350.0
CORE INLET	655.0	.000	24.408	160.1	350.0	501.6	160.1	350.0	501.6	160.1	350.0	501.6
SMOOTH	796.2	.125	28.093	226.8	350.7	575.0	226.8	376.1	599.1	226.8	376.1	599.1
SMOOTH	919.4	.234	31.306	272.5	351.5	628.9	272.5	405.5	679.0	272.5	405.5	679.0
ROUGH	921.7	.236	31.306	273.2	351.5	460.9	273.2	406.1	514.8	273.2	406.1	514.8
ROUGH	1220.0	.500	55.299	321.2	353.9	484.2	321.2	492.5	620.8	321.2	492.5	620.8
ROUGH	1333.0	.600	64.387	314.2	354.8	482.0	314.2	526.8	651.6	314.2	526.8	651.6
ROUGH	1446.0	.700	73.475	293.4	355.7	473.8	293.4	559.5	675.2	293.4	559.5	675.2
ROUGH	1559.0	.800	82.563	259.7	356.5	460.0	259.7	589.3	690.8	259.7	589.3	690.8
ROUGH	1672.0	.900	91.651	214.6	357.2	441.6	214.6	614.9	697.9	214.6	614.9	697.9
ROUGH	1728.5	.950	96.195	188.4	357.5	431.1	188.4	625.7	698.2	188.4	625.7	698.2
CORE OUTLET	1785.0	1.000	100.739	160.1	357.7	419.8	160.1	635.1	696.3	160.1	635.1	696.3
OUTLET	2235.0		116.516	.0	357.7	357.7	.0	635.1	635.1	.0	635.1	635.1

4.4. TEST BUNDLE DESIGN AND FABRICATION

A preliminary design of the test section for a 37-rod assembly with 31 fuel rod simulators (electrical heater rods) and 6 unpowered hanger rods was prepared, reviewed, and approved at GA. The drawings were sent to ORNL and ERDA for review and comment. Figure 4-1 shows a 37-rod assembly test section and parts list for which GA has the major design and fabrication responsibility, except for the fuel rod simulators. This figure denotes a GA-ORNL interface area requiring close coordination of design activities.

4.5. LIAISON WITH ORNL

A CFTL coordinating meeting was held in San Diego to review GCFR test requirements, compare them with the CFTL design, and reconcile all differences between requirements and capabilities. Structural-thermal-flow and safety results were presented by GA, and ORNL described the CFTL conceptual design and the practical operating limits. After a discussion of the CFTL test ranges, in particular modeling of the depressurization accident, the following agreement was reached between GA and ORNL: the CFTL conceptual design described in the draft sections of the system design description provides a completely acceptable basis for proceeding with CFTL design and fabrication. The CFTL requirements as defined in Ref. 4-1 and supplemented by the sample test specification (Ref. 4-4) are achievable with the CFTL.

4.6. GCFR PROTOTYPE CORE ASSEMBLY TEST PLANNING

The prototype core assembly tests will be conducted on full-size core assemblies to provide assurance that the core assemblies meet design qualification requirements prior to fabrication of the GCFR demonstration plant initial core. The objective of the prototype test program is to evaluate the preliminary design of the full-size assemblies by subjecting the assemblies to maximum GCFR helium flow conditions in a close simulation of the reactor core environment without radiation. One assembly of each type (fuel, control, and blanket) will be subjected to the equivalent of approximately 1 yr of reactor operation in a hot helium test loop.

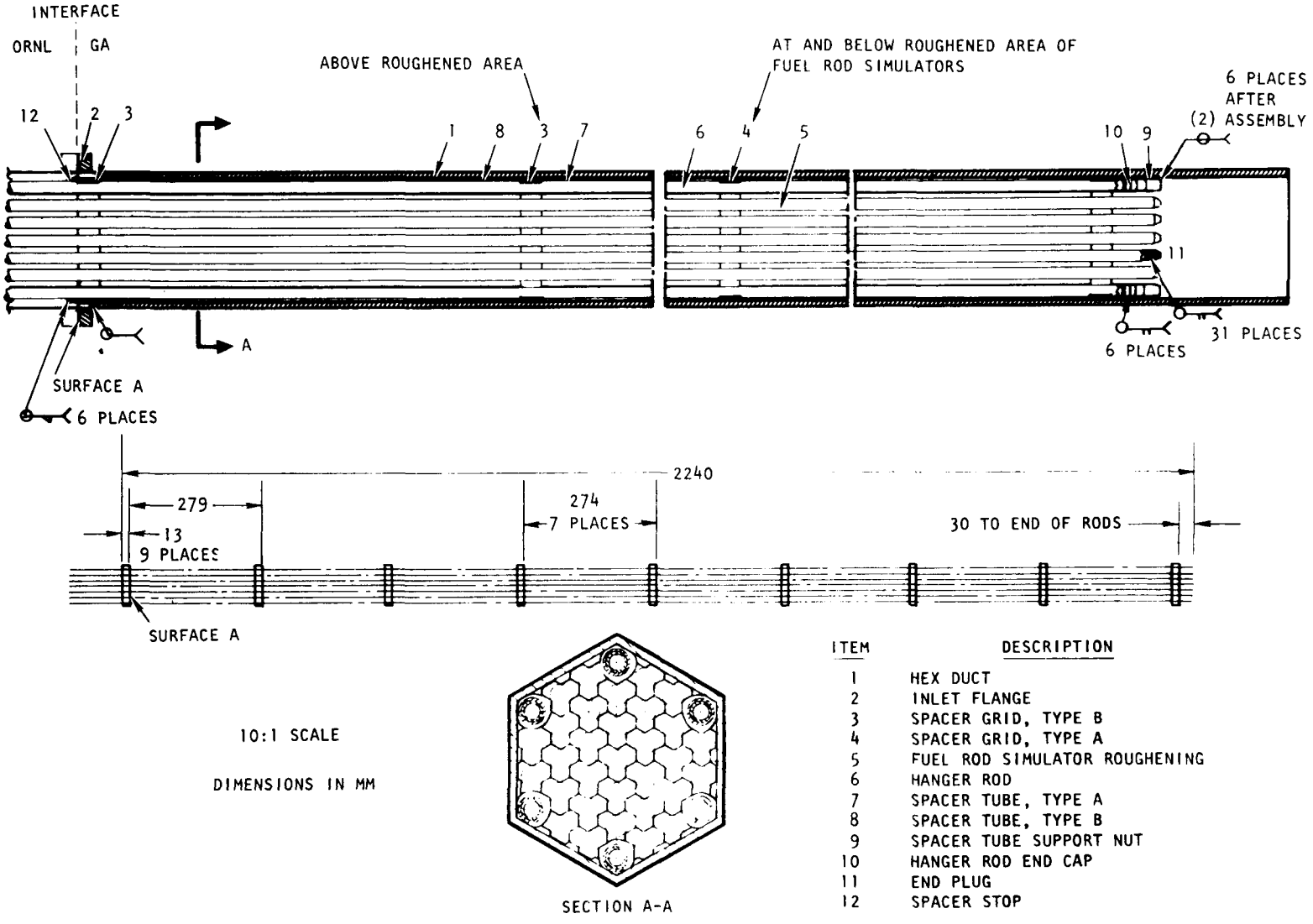

ITEM	DESCRIPTION
1	HEX DUCT
2	INLET FLANGE
3	SPACER GRID, TYPE B
4	SPACER GRID, TYPE A
5	FUEL ROD SIMULATOR ROUGHENING
6	HANGER ROD
7	SPACER TUBE, TYPE A
8	SPACER TUBE, TYPE B
9	SPACER TUBE SUPPORT NUT
10	HANGER ROD END CAP
11	END PLUG
12	SPACER STOP

Fig. 4-1. Thirty-seven-rod assembly test section

Program planning for testing of the full-size prototype core assemblies is continuing. The outline plan for the GCFR prototype core assembly test program submitted to ERDA in May 1976 has been reviewed by Aerojet Nuclear Corporation at ERDA's request, and specific comments have been forwarded to GA. These comments (mainly concerning program objectives) will be incorporated into the test program plan scheduled for completion in late FY-77.

The review of the test loop facility options for the prototype tests is continuing. This evaluation compares existing helium test loop facilities with each other and with a new facility designed especially for prototype testing. The first loop to be considered was the HHV loop in Jülich, Germany. As shown in Table 4-9 of Ref. 4-2, the HHV pressure capability is much lower than that required for prototype testing, and the flow rate capability is much higher. An engineering evaluation of these mismatches in pressure and flow revealed that the loop would provide only 60% gas density simulation of GCFR operating conditions and would be very expensive to operate. These factors plus scheduling uncertainties have caused the HHV loop to be removed from active consideration as a possible site for prototype testing.

Several other loop siting options for prototype testing are being evaluated, including the EBOR facility at INEL and the CARMEN-2 loop at Saclay, France. Ideal prototype test loop conditions versus EBOR and CARMEN-2 capabilities are shown in Table 4-3. The practicality of converting EBOR from an experimental reactor facility to a hot helium test loop for prototype testing is currently being investigated at INEL. Review of the test capabilities of the CARMEN-2 loop indicates that it is quite suitable for prototype testing. At this time, there is no agreement under which prototype testing could be conducted in the CARMEN-2 loop. A study is also being initiated to determine the feasibility of constructing a new loop (either in Europe or the U.S.) in which to conduct the prototype tests.

TABLE 4-3
PROTOTYPE TEST LOOP COMPARISON

Parameter	Ideal Prototypical Condition	EBOR	CARMEN-2[a]
Flow (kg/s)	(b)	8.8	10.8
Pressure (MPa)	9.1	7.69[c]	9.0
ΔP (KPa)	155	$\sim$200	165
Temperature (°C)	350 to 550	691 maximum	500

[a] These values may slightly change following receipt of additional information from CEA.

[b] One fuel assembly = 7.2; one control assembly = 6.2; one blanket assembly = 1.6; concurrent testing = 15.0.

[c] Individual component pressure ratings which may allow EBOR loop pressure rating to be raised are being checked.

REFERENCES

4-1. Hopkins, H. C., Jr., "Program Plan for GCFR Core Flow Test Loop," USAEC Report GA-A13080, General Atomic, August 9, 1974.

4-2. "Gas-Cooled Fast Breeder Reactor Quarterly Progress Report for the Period May 1, 1976 Through July 31, 1976," ERDA Report GA-A13975, General Atomic, August 31, 1976.

4-3. Hopkins, H. C., Jr., TSPEC - A Computer Program to Predict Approximate Model Performance in the Core Flow Test Loop," General Atomic, to be published.

4-4. "Gas-Cooled Fast Breeder Reactor Quarterly Progress Report for the Period November 1, 1975 Through January 31, 1976," ERDA Report GA-A13815, General Atomic, March 22, 1976.

4-5. "Gas-Cooled Fast Breeder Reactor Quarterly Progress Report for the Period February 1, 1976 Through April 30, 1976," ERDA Report GA-A13868, General Atomic, May 31, 1976.

5. FUELS AND MATERIAL ENGINEERING (189a No. SU007)

5.1. OXIDE FUEL, BLANKET, AND GRID PLATE SHIELDING MATERIALS TECHNOLOGY

It is the responsibility of this subtask to maintain liaison with and surveillance of other ERDA and non-ERDA programs, especially the liquid metal fast breeder reactor (LMFBR) program, to ensure the availability of all relevant information for the GCFR design. The areas included in this subtask are

1. Oxide fuel technology.
2. UO_2 (axial) blanket technology.
3. ThO_2 (radial) blanket technology.
4. Grid plate shielding technology.

During this quarter, it was decided to replace the ThO_2 in the radial blanket of the GCFR demonstration plant with UO_2. The principal reason for this change is the expected lack of reprocessing facilities for ThO_2 until the mid-1990s. Thus, the U-233 bred in the ThO_2 blanket could not be recovered and used to fuel HTGRs until the late 1990s. Work on this phase of the subtask will therefore be terminated. However, it is anticipated that test blanket assemblies containing ThO_2 will be irradiated in the demonstration plant.

5.2. CLADDING TECHNOLOGY

5.2.1. Mechanical Testing Program at Argonne National Laboratory

The purpose of this program is to determine the effects of the following factors on the behavior and mechanical properties of GCFR cladding:

1. Ribs, rib geometry, and fabrication technique.
2. Helium impurity levels typical of the GCFR environment.

The first biaxial creep rupture test (ANL test 1) was conducted to determine the effect of the end cap design and the length of the specimen. In accordance with the second test matrix, ANL test 2 was completed. Both tests were performed at 650°C at a hoop stress of ∿238 MPa in a purified helium atmosphere, ribbed and smooth claddings were tested.

During this quarter, ANL provided a draft copy of the test reports for the first and second tests. These reports are being reviewed by GA prior to publication. The important findings from the second test are given below.

1. Ribs produced by mechanical grinding have a reinforcing effect; i.e., they strengthen the cladding with respect to mechanically ground smooth cladding of the same root diameter.

2. Ribs produced by electrochemical etching at GA also appear to reinforce the cladding with respect to smooth electrochemically etched cladding of the same root diameter.

3. Electrochemically etched cladding (ribbed or smooth) appears to reduce creep rupture life relative to mechanical grinding. The quantitative effect is not greater than 10%.

These preliminary results should be viewed with some caution since the electrochemically etched surface of the specimens used in the second tests was not of an acceptable quality, having undercut ribs and pits caused by a finishing etch at an extremely high removal rate (high current density). The etched tubes currently being produced are of a better quality. The test report being prepared by ANL contains all the detailed information, including descriptions of the failures.

Preparations for the third test have been completed. Impurity monitoring devices such as gas chromatographs have been installed, and the test is expected to be started soon. This test will be conducted in helium containing 300 Pa of H_2 and 30 Pa of H_2O.* The results from this test will be compared to the Pacific Northwest Laboratory (PNL) helium loop test results.

5.2.2. Helium Loop Test Program at Pacific Northwest Laboratory

The primary objective of this program is to compare the mechanical properties determined in recirculating helium at PNL with those determined in quasistatic helium at ANL. The scope of work has been agreed upon, and evaluation of techniques for detection of pinhole leaks and ruptures has been completed. In preparation for the test program, the loop has been modified for unattended operation. The impurity monitoring system has been installed, and the loop has been satisfactorily operated with desired impurities.

During this quarter, the first biaxial creep rupture test (PNL test 1) in the helium loop was initiated. This test is being conducted at 650°C and includes ribbed cladding fabricated by electrochemical grinding and mechanical grinding in addition to smooth cladding fabricated by mechanical grinding. The hoop stress is 238 MPa. Two interim examinations at 50 hr and one at 100 hr have been completed. Although there are 20 specimens in the test, only 10 were stressed for the 100 hr; 5 were not stressed at all because of faulty welds in the capillary lead tubing (these have been repaired); and 5 were not stressed during the first 50 hr owing to leaks in the connecting lines and pressure gauges external to the loop.

Impurity monitoring and control has not been satisfactory. At different times in the test, the instruments used, i.e., a Thermox oxygen analyzer, a gas chromatograph, a parametric moisture monitor, did not work adequately. In addition, over the past year, the parametric moisture

*Recently changed from 300 MPa of H_2 and 85 MPa of H_2O as a result of initial results from PNL.

monitor has been found to be unreliable. The loop intervals oxidize continuously, and the loop leak rate is approximately 2% of the loop helium inventory per hour. Only best estimates for the hydrogen and water levels during the operation have been made; these uncertainties are probably responsible for the unusual behavior of the oxidation specimens.

The oxidation specimens (0.25-mm-thick 20% cold-worked 316 stainless steel) showed a weight gain of $\sim$11 mg/dm^2 at the end of 50 hr of exposure. The same specimens had a weight loss of $\sim$3 mg/dm^2 at the end of 100 hr of exposure. Oxidation of iron in addition to chromium during the first 50 hr and reduction of spinel to a lower oxidation state during the next 50 hr of exposure is thermodynamically feasible. This could be the explanation for the weight loss, because other mechanisms such as oxide spallation have not been observed.

To enable accurate measurement of moisture levels in the future, an EG&G model 880 dew point meter is being procured. Testing is being delayed until this instrument is installed.

5.3. F-1 FAST FLUX IRRADIATION EXPERIMENT

Postirradiation examination of the encapsulated seven-fuel-rod F-1 (X094) experiment, which achieved a maximum burnup exposure of 121 MW/kg, has been initiated at Argonne National Laboratory East (ANL-E). One capsule, G-12, is being retained at Argonne National Laboratory West (ANL-W) because neutron radiography has not yet been performed on that capsule. Gamma scanning of all the capsules was performed at ANL-W prior to shipment to ANL-E. De-encapsulation and initial destructive postirradiation examination will be started early next quarter.

The approximate length of charcoal in various sections of the upper and lower active charcoal traps of capsules G-4, G-8, G-9, G-10, G-11, and G-13 and in the sealed trap from G-8 were measured after irradiation using neutron radiographs. These lengths were compared to the original lengths measured from preirradiation x-radiographs. The results are listed in Table 5-1.

TABLE 5-1
CHANGES IN THE ACTIVE CHARCOAL BED LENGTHS OF F-1 CAPSULES G-4, G-8, G-9, G-10, G-11, AND G-13 (X094)

Capsule	Trap Location	Volume Shrinkage (%)
G-4	Upper	58.5 ± 2.1
	Lower	55.3 ± 1.6
G-9	Upper	51.2 ± 2.1
	Lower	36.2 ± 2.8
G-10	Upper	50.7 ± 0.7
	Lower	38.4 ± 7.9
G-11	Upper	50.3 ± 2.6
	Lower	40.8 ± 8.1
G-13	Upper	52.0 ± 3.7
	Lower	41.7 ± 5.5
G-8	Sealed trap	
	Upper	59.1
	Lower	51.5

The amount of charcoal shrinkage in the traps of capsules G-9, G-10, G-11, and G-13, which had fuel burnups of 71 MWd/kg, was less than that in the traps of capsules G-4 and G-8, which had fuel burnups of 121 MWd/kg and 96 MWd/kg, respectively. In addition, charcoal shrinkage was less in the lower traps than in the upper traps; this difference was greater in capsules G-9, G-10, G-11, and G-13 than in capsules G-4 and G-8. Less charcoal shrinkage in the lower traps can be attributed to settling of the charcoal into a cooler temperature region and a lower fluence zone farther from the fuel core. Conversely, more shrinkage in the upper traps can be attributed to settling of the charcoal into a hotter temperature region and a higher fluence zone closer to the fuel core.

Fuel particle analysis for tritium fast fission yield is continuing. Selected particles from capsules G-1, G-2, G-5, and G-7 were shipped to Allied Chemical, Idaho Falls, for additional heavy metal isotopic analysis.

Impurity analysis of fuel particles irradiated in the F-1 fuel rods indicated that lithium, boron, and nitrogen can be eliminated as sources for production of tritium. This further supports the higher ternary fission yield values observed for U-238 and Th-232 (Ref. 5-1). These yield values are being assessed for fractional contributions of bred Pu-239 and U-233.

Dimensional changes in passive silicon carbide (SiC) temperature monitors were determined by postirradiation isochronal annealing. The annealing temperature at which a recovery in length of the SiC monitor begins to occur is indicative of the irradiation temperature during the last cycle of irradiation. The preliminary temperatures for monitors from capsules G-1 and G-6 at the inlet and outlet ends are about 50°C higher than the known coolant inlet temperature and calculated outlet temperature. These temperature monitors are doubly encapsulated in gas-filled subcapsules, and the indicated exposure temperature may be influenced by gamma heating and a thermal resistance path to the static sodium bond. An analysis of this heating source is now being performed.

5.4. F-3 FAST FLUX IRRADIATION EXPERIMENT

The F-3 capsules were irradiated in location 4B3 in EBR-II to an exposure of 46 MWd/kg; the burnup goal was 100 MWd/kg. These capsules shared a type J19A subassembly (X206) with the ANL group-08 high-temperature chemistry experiment, as reported in Ref. 5-2. The experiment reached an exposure of 46 MWd/kg on February 11, 1976, at which time it was removed from the core for a planned interim examination.

As reported in Ref. 5-1, nine of the ten GA fuel rods failed, as indicated by Xe-133 gamma counting of the capsule plena, which was confirmed by neutron radiography of the capsules. Reference 5-2 discusses analysis of the neutron radiographs and the findings of eddy current testing at ANL-E of capsule G-18, which contained the intact fuel rod. The ANL findings indicate that the failures may have been caused by inadequate capsule sodium bonds.

The upper dosimeter, shield material subcapsule, and lower charcoal trap dosimeter assemblies were cut out of failed capsules G-14, G-19, and G-20, and the upper dosimeter and shield material subcapsules were loaded into a cask for shipment to GA. Difficulty was encountered in removing the charcoal and dosimeter tube from the trap assembly owing to sodium intrusion into the traps. The end caps of the traps were removed by circumferential cuts, but the contents could not be pushed out even when the assembly was heated to melt the sodium. The contents did not become free when a longitudinal cut in the trap tube was made, and the charcoal and sodium remained intact and adhered to the dosimeter tube. The charcoal samples have been loaded into aluminum tubes for gamma scanning of the charcoal. Continuous gamma scan chart records for these capsules have been received from ANL and are being analyzed at GA.

During removal of the upper capsule tube from the intact G-18 rod, in preparation for puncturing of the rod plenum for extraction of the plenum gas, the circumferential cut through the capsule tube at the elevation of the holddown spring was inadvertently made too deep because

the capsule and fuel rod cladding came away from the lower capsule as a unit, exposing the holddown spring inside the fuel rod. As a result, the fission gas sample was lost from the G-18 fuel rod. Preparations are under way to make additional cuts (three longitudinal cuts 120 deg apart) in the G-18 capsule tubing using guard rings to limit the depth of the saw cut to the capsule wall thickness.

5.5. F-5 PROTOTYPE IRRADIATION EXPERIMENT

Design work and ordering of materials continued for the F-5 prototype design fuel rod experiment to be carried out for experimental study of performance of fuel rods irradiated under simulated GCFR conditions to high burnups for the purposes of (1) determining the reliability of the GCFR fuel rod design, (2) discovering what failure modes may exist, and (3) studying the effect of a step power increase which simulates the 180-deg rotation of a subassembly at the core blanket interface in the proposed GCFR demonstration plant.

Initially, the F-5 experiment was planned to be done in a single 31-rod subassembly because of concern for reactivity effects in EBR-II. However, because the EBR-II project does not now expect reactivity to be a problem and because of the desire to perform the steady-state testing portion of the experiment in a subassembly separate from that in which the step power change is performed, the experiment has been redesigned as a double 19-rod subassembly experiment. The new schedule for F-5 is given in Fig. 5-1. The December 1980 planned shutdown for EBR-II corresponds to an exposure of 100 MWd/kg for the F-5 experiment.

Design drawings have been completed for fission product traps (lower end plug assemblies), dosimeter assemblies, and ribbed cladding. Drawings must be completed for special blanket pellets to be used at the fuel blanket interface and shield material test capsules to be included in the subassembly hardware.

An analysis was initiated to determine the design requirements for the special blanket pellets at the fuel blanket interface for accommodating

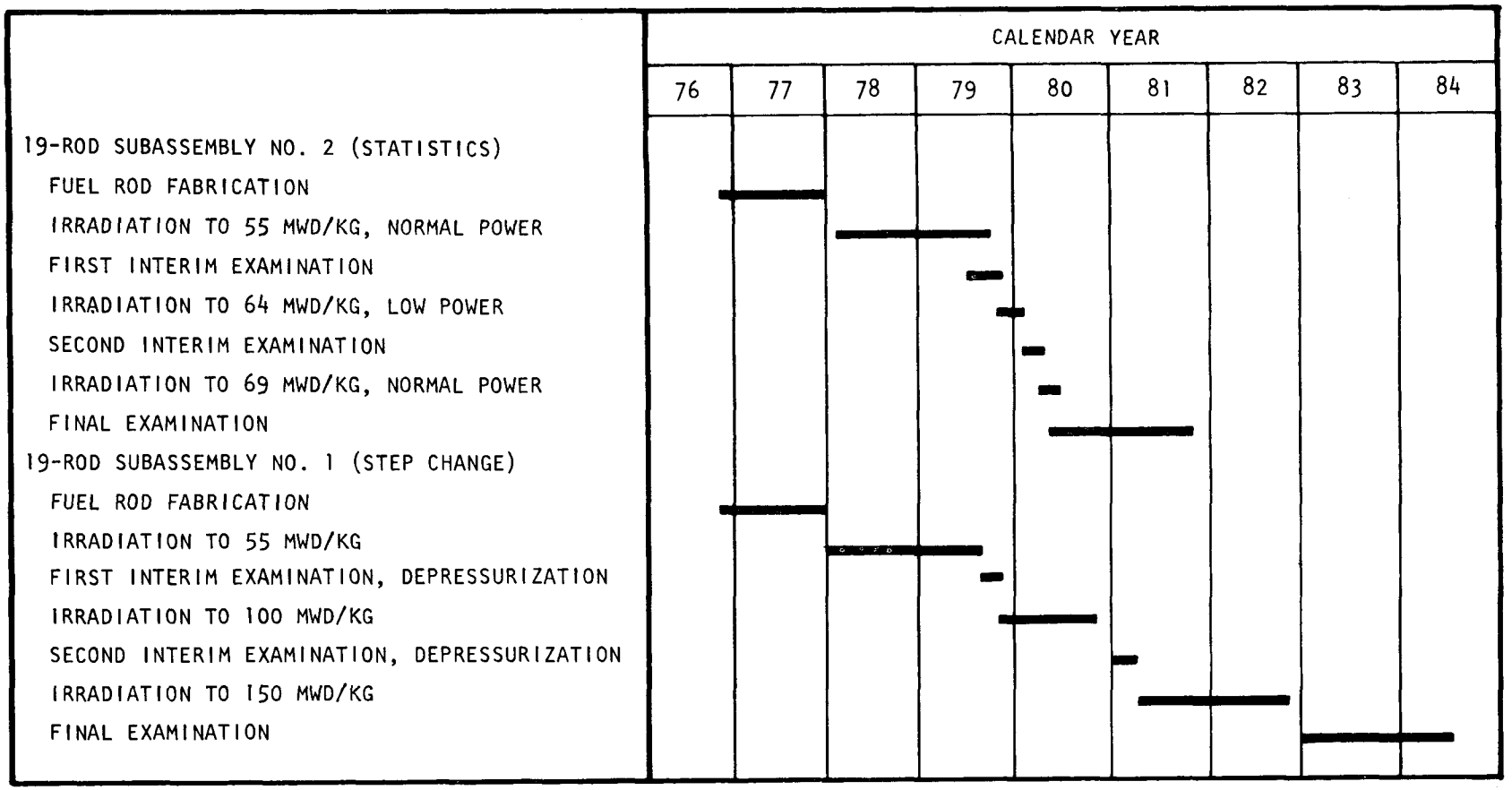

Fig. 5-1. F-5 experiment schedule based on starting with two 19-rod subassemblies

volatile fission product transport to the interface during fuel rod irradiation. These analyses are described in Section 6.

5.6. GB-10 VENTED FUEL ROD EXPERIMENT

Irradiation of the GB-10 sweep gas fuel rod capsule experiment has been completed. Fission product release and transport in GCFR fuel were measured in capsule GB-10, which was irradiated in the Oak Ridge reactor (ORR). Burnup of the pressure-equalized and vented fuel rod in capsule GB-10 reached approximately 100 MWd/kg, the revised exposure goal. The first 27 MWd/kg were accumulated at a heat generation rate of 39.4 kW/m and a cladding outside surface temperature of 565°C; from 27 to 75 MWd/kg have been accumulated at 44.3 kW/m at a cladding outside surface temperature of 630°C, and from 75 MWd/kg to the current burnup have been accumulated at 48 kW/m and a cladding outside temperature of 685°C.

The fuel rod was successfully de-encapsulated at ORNL, where it was neutron radiographed, and a preliminary gamma scan was made to determine the distribution of relatively short-lived iodine fission products. The fuel rod, thermal sleeve assembly, pieces of sweep gas lines, Na-K, and washings have been shipped from ORNL to ANL, where further nondestructive examination has begun; destructive examination will follow. The charcoal trap and flux monitor wires (after separation from the fuel rod and thermal sleeve assembly) will be returned to GA for analysis.

5.7. HEDL CLADDING IRRADIATIONS

The test plan for the GCFR cladding irradiation and postirradiation test program has been formulated. The objectives of the test program are as follows:

1. Determine if mechanical behavior, in terms of load-carrying ability, of irradiated GCFR ribbed cladding is different from that of irradiated smooth cladding under biaxial loading

conditions. The stress state, but not the absolute level of stresses expected in the GCFR, will be simulated.

2. Determine if mechanical properties such as rupture life and creep ductility measured under the expected GCFR stress state (i.e., hoop to axial tensile stress ratio of unity) are equal to or significantly different from those determined under internal pressure loading conditions (hoop to axial tensile stress ratio of 2).

3. Using a statistically meaningful test program, determine the quantitative effects of ribs and stress state on the creep rupture behavior of irradiated GCFR cladding.

Some ribbed and smooth GCFR cladding specimens have already been irradiated, and some are being irradiated as part of Hanford Engineering Development Laboratory (HEDL) cladding irradiation test capsules. Additional irradiation is considered necessary because the limited number of specimens in the initial test matrix do not cover the temperature range or the fluence levels typical of the GCFR. For these reasons, a preliminary second irradiation test matrix has been formulated and is in the process of being finalized.

GA has documented and provided ANL-E with detailed postirradiation test requirements for the 15 smooth and ribbed cladding specimens which have been irradiated. The unirradiated control specimens have been shipped from HEDL to ANL-E, where work has begun on testing the control samples in preparation for postirradiation tests.

The postirradiation test matrix for the second irradiation test has not been formulated. This test will include biaxial creep rupture testing at hoop to axial tensile stress ratios of 2 and 1 as well as pure tensile testing. Formulation of the postirradiation test matrix will be delayed until input from the initial tests is obtained.

REFERENCES

5-1. "Gas-Cooled Fast Breeder Reactor Quarterly Progress Report for the Period May 1, 1976 Through July 31, 1976," ERDA Report GA-A13975, General Atomic, August 31, 1976.

5-2. "Gas-Cooled Fast Breeder Reactor Quarterly Progress Report for the Period February 1, 1976 Through April 30, 1976," ERDA Report GA-A13868, General Atomic, May 31, 1976.

6. FUEL ROD ENGINEERING (189a No. SU007)

The objective of this task is to evaluate the steady-state and transient performance of the fuel, blanket, and control rods for the determination of performance characteristics, operating limits, and design criteria. To this end, analytical tools (such as the LIFE-III code) are being adapted and/or developed and applied to the analysis of the GCFR prototypical rods and experimental rods. In addition, continuous surveillance of the LMFBR fuels and materials development program and technology is maintained to maximize the use of development technology and material properties. Support is also given for the planning and designing of irradiation experiments.

6.1. FUEL, BLANKET, AND CONTROL ROD ANALYTICAL METHODS

6.1.1. Fuel Rod Analytical Method

A new version of the LIFE code known as LIFE-IIIA, has been developed and approved by the LIFE Working Group and placed on file at the Berkeley computer facility for review. It is available from the LIFE library as subset L3PL3 (source file) and subset L30B3 (object file). The LIFE-III master version (L3PL2 and L30B2), which LIFE-IIIA replaces, has been removed from the LIFE library and placed on magnetic tape in storage.

The draft of the LIFE-III fuel assembly performance code user's manual was received from ANL and reviewed. The major improvements contained in LIFE-IIIA are (1) updated materials properties, (2) anisotropic fuel swelling model, (3) finite deformation model for the fuel, and (4) lifetime analysis. The new materials properties used in LIFE-IIIA reflect the current state-of-the-art in Ref. 6-1. The anisotropic fuel swelling developed by Westinghouse Advanced Reactors Division represents a substantial improvement over the very simple LIFE-III model. The anisotropic fuel

swelling model introduces two significant changes in the prediction of thermal performance: a slower fuel-cladding gap closure rate and an increase in center void size. Although small deformation theory is adequate for cladding and outer fuel regions, the strains are large (>10% are commonplace) in the high-temperature region of the fuel. Therefore, a finite deformation theory is required for an accurate and realistic analysis.

A new subroutine FRACT has been included in LIFE-IIIA to evaluate cladding lifetime. Two lifetime criteria based on cumulative time to rupture and total thermal creep strain are included. The lifetime analysis is peripheral to the LIFE mechanical analysis, and no action is taken if lifetime is exhausted.

6.1.2. Blanket Rod Analytical Methods

A preliminary evaluation of blanket rod analytical methods was completed. It has been concluded that with some necessary modifications, the LIFE code can be adopted for blanket rod performance analysis. Since the LIFE code was developed for prediction of the performance of the LMFBR fuel rod which used mixed oxide for the fuel material, it is necessary that the built-in mixed oxide fuel properties in the code be replaced by those of uranium oxide, which is the current blanket rod pellet material. As a result, the main effort in adopting the LIFE code for the GCFR blanket rod performance analysis is to compile UO_2 properties such as mechanical, thermal, and irradiation performance and rearrange them in a functional form which can be incorporated into the LIFE computer program. This effort will be undertaken in the coming fiscal year.

6.2. ANALYSIS OF IRRADIATION TESTS

6.2.1. Preliminary Evaluation of Cesium Migration Effects on F-5 Blanket Rod Pellet Design

The transport and reaction of fission product cesium in a fuel rod during irradiation may affect fuel rod performance in various ways, one

of which is the formation of cesium uranate (Cs_2UO_4) owing to the reaction of cesium and axial blanket urania pellets. Formation of Cs_2UO_4 is of interest because it leads to swelling of the blanket pellet, which could cause failure of the cladding. Design alternatives may provide the solution to this problem. For instance, the formation of Cs_2UO_4 in the blanket region might be chemically reduced by (1) containing the cesium in the fuel region by providing a hyperstoichiometric mixed oxide in the fuel region, or (2) decreasing the condensed cesium chemical reactivity by supplying a low oxygen/uranium ratio. It may also be physically possible to provide an adequate void in the first blanket pellet to accommodate the volume increase due to the formation of Cs_2UO_4. The void and oxygen/uranium ratio of the blanket pellet of the F-5 experimental rods have been determined to be a possible means of reducing the pellet-cladding interaction from excessive Cs_2UO_4 swelling.

6.2.1.1. Porosity Analysis. Throughout fuel rod lifetime, total cesium yield Y can be expressed by

$$Y = y \cdot F \cdot V_f \quad ,$$

where y = cesium isotope yield per fission (atoms/fission),
F = total fission density (fissions/cm^3),
V_f = total volume of fuel region (cm^3).

By definition, fission density is related to the burnup β and initial density of heavy metal atoms N_f by

$$\beta \equiv F/N_f \quad .$$

Therefore,

$$Y = y \cdot \beta \cdot N_f \cdot V_f \quad .$$

For the F-5 experimental rods,

$$\beta = 150 \text{ MWd/kg (maximum planned burnup)} \quad ,$$

$$N_f = \frac{(0.91)(10.98)(6.02 \times 10^{23})}{270} = 2.23 \times 10^{22} \text{ atoms/cm}^3 \quad ,$$

$$V_f = \frac{\pi}{4} (0.24)^2(13.5)(2.54)^3 = 10 \text{ cm}^3 \quad ,$$

and from Ref. 6-2,

$$y = 0.209 \text{ atoms/fission} \quad .$$

Consequently,

$$Y = (0.209)(0.165)(2.23 \times 10^{22})(10) = 7.69 \times 10^{21} \text{ atoms}$$

$$= 1.73 \text{ grams} \quad .$$

The chemical reaction for the formation of Cs_2UO_4 by reaction of gaseous cesium with urania may be written as

$$2Cs(g) + O_2(g) + UO_2(s) = Cs_2UO_4 \quad .$$

To be conservative, it is assumed that all cesium generated in the fuel region migrates equally to the lower and upper blanket regions. Furthermore, it is assumed that the oxygen potential in the blanket regions is greater than the free energy of formation of Cs_2UO_4, so that all cesium will be converted into Cs_2UO_4 at the first blanket pellet next to the fuel column. Thus, the amount of Cs_2UO_4 formed is

$$W_{max} = \frac{7.69 \times 10^{21}}{2 \times 2} = 1.92 \times 10^{21} \text{ molecules}$$

$$= \frac{1.92 \times 10^{21}}{6.02 \times 10^{23}} [2 \times 135 + 238 + 16 \times 4] = 1.82 \text{ grams} \quad .$$

This is the maximum amount of Cs_2UO_4 that can be formed at the lower or upper blanket regions if cesium is assumed to migrate equally in both rod axial directions.

The relative distribution of Cs-137 radioactivities in an irradiated fuel rod has been studied by gamma scanning in the F-1 experiment and is reported in Table 7.2 of Ref. 6-3. Although gamma scanning was done only for Cs-137, it is believed that the result is applicable to the distribution of all cesium isotopes in the fuel because of the similar chemical behavior of Cs-133, Cs-135, and Cs-137. Based on this, the fraction of total cesium produced in the fuel region which migrates to the upper and lower blanket regions is taken to be approximately equal to 0.2. Thus, the amount of Cs_2UO_4 which can be formed is

$$W_{F-1} = 0.2W_{max} = 3.84 \times 10^{26} \text{ molecules} = 0.364 \text{ grams} \quad .$$

The maximum void (P_{max}) of the first blanket pellet required to accommodate Cs_2UO_4 swelling is

$$P_{max} = \frac{\frac{1.92 \times 10^{21}}{6.02 \times 10^{23}} \left(\frac{135 \times 2 + 238 + 16 \times 4}{6.65} - \frac{238 + 16 \times 2}{10.98} \right)}{\frac{\pi}{4} (0.629)^2 (0.9)}$$

$$= 0.70 \quad .$$

Based on F-1 experimental results, the required void is

$$P_{F-1} = 0.2 \times 0.76 = 0.152 \quad .$$

6.2.1.2. Stoichiometric Analysis. The formation of Cs_2UO_4 in urania blanket pellets also depends on the stoichiometry of the urania. Thermodynamically, the reaction of cesium with hyperstoichiometric urania is limited by the excess oxygen in the urania, as indicated by the reaction

$$X\ Cs + UO_{2+x} = \frac{X}{2}\ Cs_2UO_4 + \frac{2 - x}{2}\ UO_2 \quad .$$

The difference ΔV between the volume of the products of the above reaction and the initial pellet volume V_p is

$$\Delta V = V_p\left\{\frac{f}{V_{UO_{2+x}}}\left[\frac{x}{2}\,V_{Cs_2UO_4} + \left(1 - \frac{x}{2}\right)V_{UO_2}\right] - 1\right\} \quad ,$$

where f = fraction of theoretical density of blanket pellet,

$V_{UO_{2+x}}$ = molar volume of UO_{2+x},

$V_{Cs_2UO_4}$ = molar volume of Cs_2UO_4,

V_{UO_2} = molar volume of UO_2.

The maximum initial value of the deviation from the exact stoichiometry X_{max} necessary for the reaction to form a mixture which precisely fills the available void in the pellet can be obtained by setting ΔV equal to zero; thus,

$$X_{max} = 2\left(\frac{1}{f} - \frac{V_{UO_2}}{V_{UO_{2+x}}}\right)\frac{V_{UO_{2+x}}}{V_{Cs_2UO_4} - V_{UO_2}} \quad .$$

From Ref. 6-4,

$$V_{UO_{2+x}} = V_{UO_2} = 24.6\ cm^3/mol \quad ,$$

$$V_{Cs_2UO_4} = 85.3\ cm^3/mol \quad .$$

Thus,

$$X_{max} = 0.81 \left(\frac{1}{f} - 1 \right) \quad .$$

For the F-5 experiment blanket pellet,

$$f = 0.933 \quad .$$

Therefore,

$$X_{max} = 0.058 \quad .$$

6.2.1.3. Conclusions. In the preceding analyses, it was found that the blanket pellet-cladding interaction due to the formation of Cs_2UO_4 at the fuel-blanket interface can be avoided provided that (1) the void of the first blanket pellet is at least 14%, or (2) the oxygen/uranium ratio of the first blanket pellet is at most 2.058. The formation of Cs_2UO_4 at the fuel-blanket interface depends very much on the transport of cesium in the fuel rod, a complicated physical-chemical phenomenon whose theory is not presently well developed. As a result, the analysis is based on available experimental results and simplifying assumptions.

The porosity analysis is based on the F-1 experimental results. The calculated 15.2% porosity to accommodate Cs_2UO_4 swelling can be incorporated into the first blanket pellet in a variety of ways. For instance, a lower pellet density, a smaller pellet diameter, or a combination of both may be used for the design. In addition, special pellet configurations such as annular pellets or axial serrations and slots may be considered as alternatives. However, the choice of pellet geometry must be based on a thermal mechanical analysis of the pellet.

In the stoichiometry analysis, it is assumed that the only available oxygen for Cs_2UO_4 formation comes from the excess oxygen in the urania. This may not be the case in view of possible oxygen migration from the

fuel region. However, to take this into account requires a complicated theory of oxygen redistribution inside the fuel rod; this theory is not presently well formulated.

6.3. DESIGN CRITERIA

A set of design criteria has been assembled under Subtasks 23.21.200.76 and 23.23.100.76 for the GCFR fuel rod cladding and the GCFR fuel blanket and control assemblies. These criteria were to be put together in three phases: (1) review of LMFBR criteria and extraction of applicable criteria, (2) generation of unique GCFR criteria, and (3) verification of criteria by trial application to current GCFR component designs and LMFBR and GCFR test components.

The first attempt to assemble a set of GCFR structural criteria involved modification of the existing Westinghouse and General Electric criteria to fit GCFR needs. After review, it was determined that the modification was adequate, but important aspects were missing. Concurrent with this effort, GA was asked to participate in the National Working Group structural design criteria effort. Progress on this unified set of design rules was monitored to ensure that the critiera would be applicable to the GCFR system.

As a result of participation in and review of the activities of the National Working Group, it was determined that this unified set of criteria would be adequate for the preliminary GCFR core consumable (combined fuel rod and core assembly) structural design criteria because the actual design rules and limits are written in general terms. Particularization occurs when the components under consideration are classified according to the reliability required for off-normal conditions of various severities. This classification will vary from manufacturer to manufacturer and among different types of systems. Once this component classification is made, a table of design margins can be consulted to determine the numerical values for the limits proposed in the criteria. These limits and the

material properties data may require modification for GCFR use. However, because of the lack of experience in using such a set of design rules and the limited analyses performed with LMFBR data, no judgments can be made at this time concerning the applicability of these limit values to the GCFR system. Consequently, the design rules and margins have been accepted as written for the preliminary GCFR structural design criteria.

In order to justify the selection of these criteria for GCFR application and verify their adequacy for ensuring structural integrity, a trial application program is being undertaken. The experience gained and the results obtained from this program will be combined with the National Working Group's activities on improvement of the design criteria. In addition, work will begin near the end of FY-77 on an analysis procedures manual to be used in the application of the design criteria. Future accomplishments will be reported in a separate section devoted to the design criteria of all core components and assemblies.

6.4. ROD ANALYSIS AND PERFORMANCE

6.4.1. Comparison of LIFE-III and LIFE-IIIA Predictions of GCFR Fuel Rod Performance

Owing to the introduction of LIFE-IIIA into the LIFE master file at the Berkeley CDC-7600 computer, a study was conducted which compared the differences in prediction of GCFR fuel rod performance between LIFE-III and LIFE-IIIA. In this study, the rod fuel region was divided into three equal axial sections in accordance with the LIFE code model. An additional, arbitrarily large plenum section was connected to the rod to simulate pressure equalization of the GCFR vented rod. The reactor power was taken to be 300 MW (full power) for 750 days, and three 15% overpowers were arbitrarily superimposed on the reactor power history. The maximum fuel rod linear power was taken to be 377 W/cm. Because the code provides the capability of simulating a vented rod by specifying plenum pressure as an input, an additional LIFE-IIIA analysis was performed using this option so that the plenum volume represents all the voids available in the GCFR fuel rod design except those in the fuel region.

The results of this study indicate that LIFE-IIIA predicts a nonclosed, decreasing fuel-cladding gap throughout lifetime in contrast to the gap closure after full power predicted by LIFE-III. Thus, the fuel centerline temperature predicted by LIFE-IIIA is higher, but the circumferential creep strain predicted by LIFE-IIIA is significantly reduced because there is no fuel-cladding mechanical interaction. Furthermore, owing to a lack of fission gas pressure buildup in the case of constant plenum pressure input, the circumferential creep strain becomes negative as a result of the small pressure differential between the external and internal pressures. These results seem to be in good agreement with what was intended for the new version of LIFE-IIIA as a consequence of the introduction of the anisotropic fuel swelling model. LIFE-IIIA is currently being calibrated and checked out, and therefore these results are preliminary.

6.4.2. Design Evaluation of Absorber Materials for the GCFR Control Rod

The primary concern in selecting an absorber material for control rods is the nuclear reactivity worth necessary for safe reactor control and compensation of fuel burnup. Once these criteria are satisfied in the nuclear analysis, the design of a control rod which possesses adequate structural integrity and performance reliability through its lifetime becomes a thermomechanical problem.

The limitations imposed on control rod design for various fast reactors are generally similar to each other. According to the current design of the fast flux test facility, these limitations are loss of reactivity worth (10%), cladding permanent strain ($\leq$0.2% for steady-state operation and $\leq$0.3% during operation, including transients), hoop stress ($\leq$0.9 yield stress), and gap closure (Ref. 6-5). Control rod cladding strains and stresses could be caused by internal gas pressure or absorber pellet swelling. These limitations imply that the rates of generation and release of gas from and swelling of absorber materials are important in selecting an absorber material.

The compatibility of the absorber and cladding must also be considered since chemical reactions could embrittle and weaken the cladding, making it more susceptible to deformation or rupture. Since pellet swelling, gas release, and compatibility are temperature-dependent phenomena, knowledge of the heat generation rate and the thermal conductivity of the absorber is also extremely important for control rod analysis and design. These basic characteristics impact the lifetime and design of control rods.

In view of these requirements for absorber material, boron carbide (B_4C) has become the leading candidate for control rods in all fast reactors because of the satisfactory neutron absorption cross section afforded by B-10 and the form and stability of the material; in addition, the fabrication technology is far more advanced than that for any other candidate material. However, a major concern is that B_4C control rod lifetimes may be unsatisfactorily short (e.g., less than one effective full-power year) owing to loss of reactivity worth. Thus, the interest in other materials is primarily to extend control rod lifetimes.

The primary backup absorber material being considered for fast reactor application is europium, generally in the form of europium oxide (Eu_2O_3). The main advantages of this material are (1) gas is not generated during irradiation and (2) the neutron absorption cross section should not appreciably diminish during service because the transmutation product isotopes have high absorption cross sections. Possible disadvantages of this material are high afterheating, gamma activity, and lower thermal conductivity relative to B_4C.

In order to establish a rational basis for selecting the absorber material for the GCFR control rod, a literature review and evaluation has been performed to summarize nuclear characteristics, thermal and mechanical properties, compatibility with cladding materials, and irradiation performance of B_4C and Eu_2O_3, and the following conclusions have been drawn:

1. To obtain the required reactivity worth lifetime, natural or, if necessary, enriched B_4C is recommended as the GCFR control rod

absorber material, at least for the initial core, on the basis of its satisfactory material properties, compatibility with the cladding, the advanced fabrication technology, and the available knowledge of B_4C in-reactor performance behavior. Furthermore, since the GCFR control rod is designed to be vented, the problems of helium gas release associated with B_4C are eliminated.

2. The features of Eu_2O_3 which make it a potential absorber material cannot be overlooked, especially its slower loss of reactivity worth. Therefore, it is recommended that Eu_2O_3 technology development be closely followed so that it can be the primary backup absorber material for the GCFR control rod.

3. In order to be able to perform detailed anlaysis of in-reactor control rod behavior and future irradiation tests, it is recommended that performance analysis computer codes such as CONROD (Ref. 6-6) SIEX/PECT (Refs. 6-7, 6-8) and ABSORB (Ref. 6-9) be acquired and adapted to GCFR control rod design. This is important because only with adequate computer codes is it possible to perform the parametric studies necessary for attaining the optimal design of the GCFR control rod.

6.4.3. Review of Fast Reactor Grid Spacers

Various grid-spaced fuel assembly designs for fast reactors were reviewed to determine the criteria used to select the grid-to-grid axial pitch. Criteria exist which limit flow-induced vibrations and changes in coolant flow channel geometry caused by rod bowing. Similar criteria are proposed for use in selecting the pitch of spacer grids in GCFR fuel assemblies.

A number of foreign and domestic LMFBRs have or will use grid spacers to maintain rod spacing in their fuel assemblies (Ref. 6-10), including KNK-2 (Karlsruhe, Germany), PFR (Dounreay, Scotland), and FERMI and SNR-300 (Kalkar, Germany). In addition, selected driver assemblies in the fast test reactor (FTR) will employ the grid-spaced design.

The KNK-2 and SNR-300 fuel assemblies use full spacer grids which are very similar in design and manufacture to those of the GCFR. The average grid-to-grid pitch through the assembly is about 170 mm, with the grids in the core region being spaced closer together and the grids for the axial blankets being spaced further apart.

Development of a grid-spaced driver assembly for the FTR has been in progress for some time. An early design (circa 1968) utilized full grids on a 250 mm pitch. The spacer grids were designed to constrain the rod laterally and rotationally. The calculations presented in Ref. 6-11 indicate that flow-induced vibrations were considered to be the design limiting deflection mechanism, and the design criterion applied limited the amplitude of vibration to less than 0.0254 mm based on successful light water reactor experience.

In more recent designs, the importance of limiting rod bowing which is due to the temperature dependence of irradiation swelling became recognized, and additional spacers were added to better restrain the rod. The latest FTR grid spacer driver assembly design (Ref. 6-12) utilizes staggered (rhombic) grids located on a 75-mm pitch in the active core region (full honeycomb grids on a 150-mm pitch are considered as an alternate). These grids provide only translational constraint and are not designed to provide rotational restraint.

The FTR criterion for selecting grid pitch limits deflections due to flow-induced vibrations and rod bowing. Specifically, the criterion states that flow-induced vibration amplitudes must be limited to 0.0254 mm and rod bowing due to temperature dependence of irradiation swelling must be restricted so that the area change in an adjacent flow channel is less than 10% of the original flow channel area.

The CRASIB code was used to determine spacer rod bowing, and it was found that the bowing criterion resulted in a maximum allowable full grid spacer pitch of 165 mm. Additional analysis indicated that the bowing criterion could also be met with staggered (rhombic) grids on a 75-mm pitch.

The latter analysis is considered weak, however, because of the incorrect and possibly nonconservative way in which the one-way support offered by rhombic spacer grids was modeled. It was noted that the FTR driver assembly edge rods are undercooled over their whole length, whereas the edge rods in a GCFR fuel assembly are undercooled in the smooth section of the core but overcooled in the roughened section. A typical value for the maximum temperature gradient across an FTR edge rod is about 33°C; for a GCFR edge rod it is about 22°C.

In conclusion, it was found that for current fast reactor grid-spaced fuel assembly designs, the axial spacing between spacer grids is typically between 150 and 170 mm when full honeycomb grids are used and approximately half this value if rhombic supports are used. The criterion used to select the spacing limits rod bowing and flow-induced vibrations to acceptable values. The following criteria have been recommended for setting the grid-to-grid spacing in GCFR fuel assemblies:

1. Flow-induced vibrations (root mean square peak-to-peak amplitude) must be less than 0.025 mm.

2. Flow channel area changes due to rod bowing must be less than 10% of the original flow channel area.

6.4.4. Fuel Rod Bowing Study

A study of fuel rod bowing characteristics was performed to (1) verify the CRASIB computer code by reproducing 1972 results, (2) compare the effects of the 1975 and 1976 estimates of the axial temperature profile, and (3) determine the success of decreasing the spacer pitch as an effective method of attenuating bowing distortion. The results indicate that the code is consistent with 1972 predictions, the rod bowing distortion is very sensitive to the axial temperature profile, and decreasing the spacer pitch to 150 mm reduces the maximum deflection to 1972 levels.

6.4.4.1. Verification of Code. An attempt was made to reproduce the bowing distortion results originally obtained by the code in 1972 in order to verify that the minor modifications made to CRASIB were done correctly. The data used in this verification are contained in Ref. 6-13. The model consisted of 36 node points extending over the rod length of 207.87 mm. The axial mean temperature profile contained three discontinuities: at the upper and lower fuel-blanket interface and at the smooth-rough transition. The radial gradient used was linear over the active core region from 0°C/cm to 17.5°C/cm. The neutron flux profile was cosinusoidal with a maximum of 3.44×10^{15} n/cm^2-s (E > 0.1 MeV), and the flux gradient was 2.2%/cm. The irradiation creep and swelling correlations were taken from Ref. 6-14. The slight differences in maximum deflection are due to the graphical approximation of the input data from the figures in Ref. 6-13.

6.4.4.2. 1975/1976 Temperature Profile Evaluation. A new model (Fig. 6-1) consisting of 43 equally spaced nodes was developed to evaluate the current axial temperature profiles. Eight grid spacer constraints were included at 250-mm intervals. The temperature profiles were generated by the COBRA code for a 100%-power edge rod with a 10-mm rod pitch, a 40% rod-to-duct clearance, and a 276-kPa pressure-drop core. The two profiles shown in Figs. 6-2 and 6-3 were generated using different thermal-hydraulic assumptions and boundary conditions; the flux profile is given in Ref. 6-15. The creep and swelling correlations used were either from Ref. 6-1 or are being considered for incorporation into Ref. 6-1.

The critical CRASIB results for the 1975 and 1976 temperature profiles are given in Table 6-1. The disparity between these results is caused by two major developments: the swelling correlation, which is an important distortion mechanism, was modified by HEDL to include the latest data, and the re-evaluated rod temperature profile (1976) is significantly different from previous calculations (1975). As a result, the maximum rod displacements and reactions have changed. More significantly, the distorted profile of the rod is entirely different, with the maximum distortion now occurring near the core midplane.

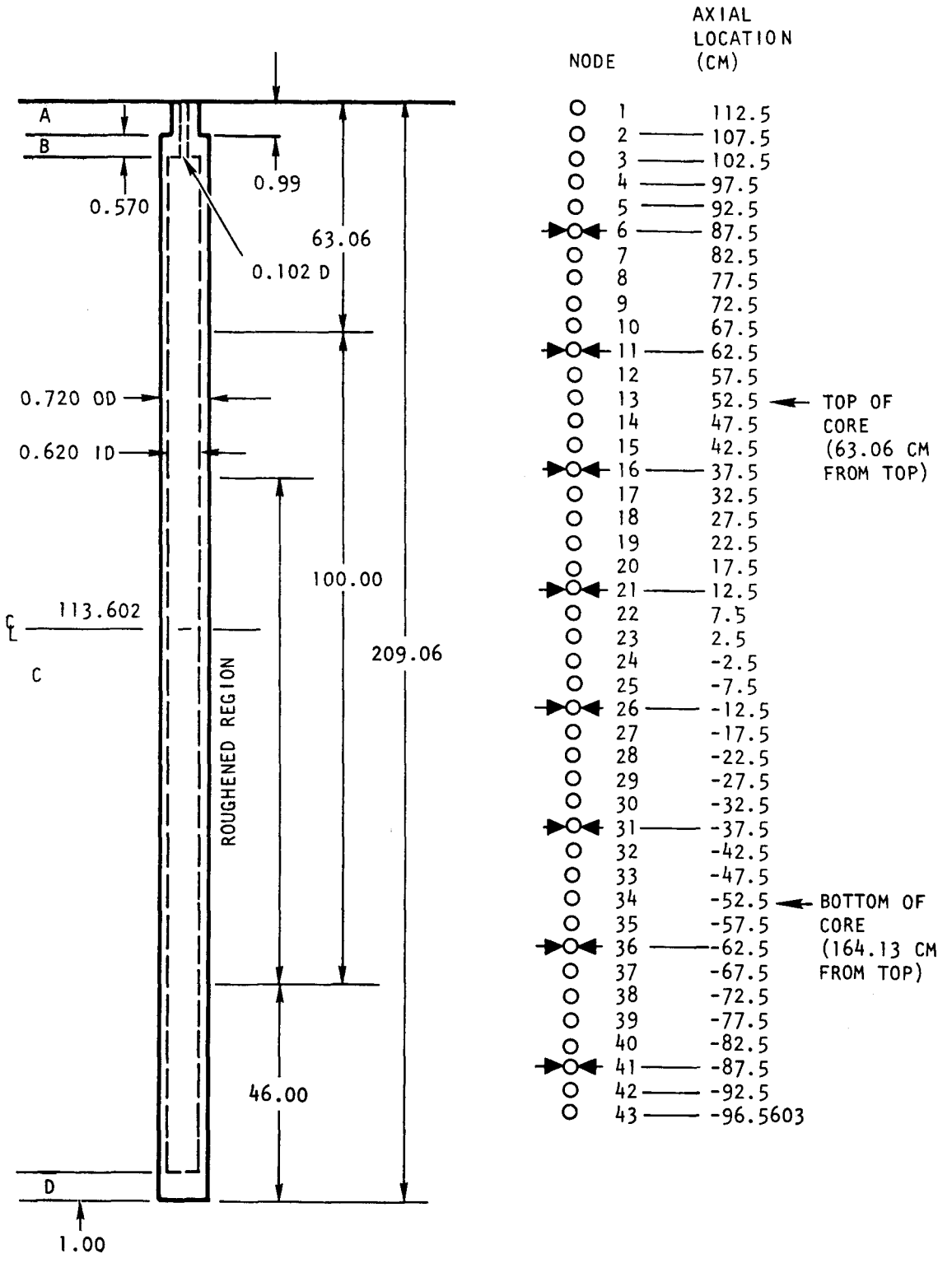

Fig. 6-1. Fuel rod CRASIB model

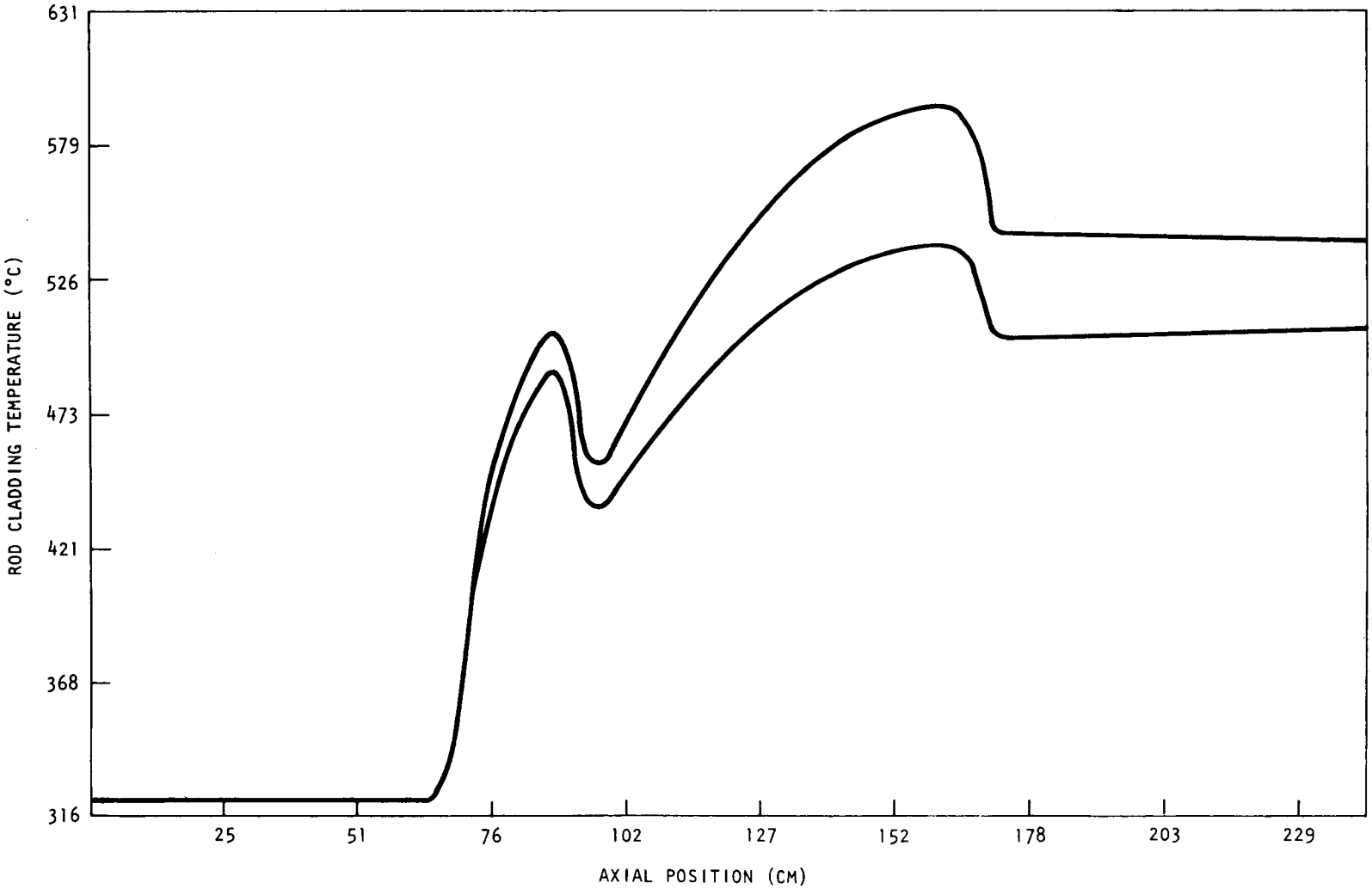

Fig. 6-2. 1975 rod temperature profile

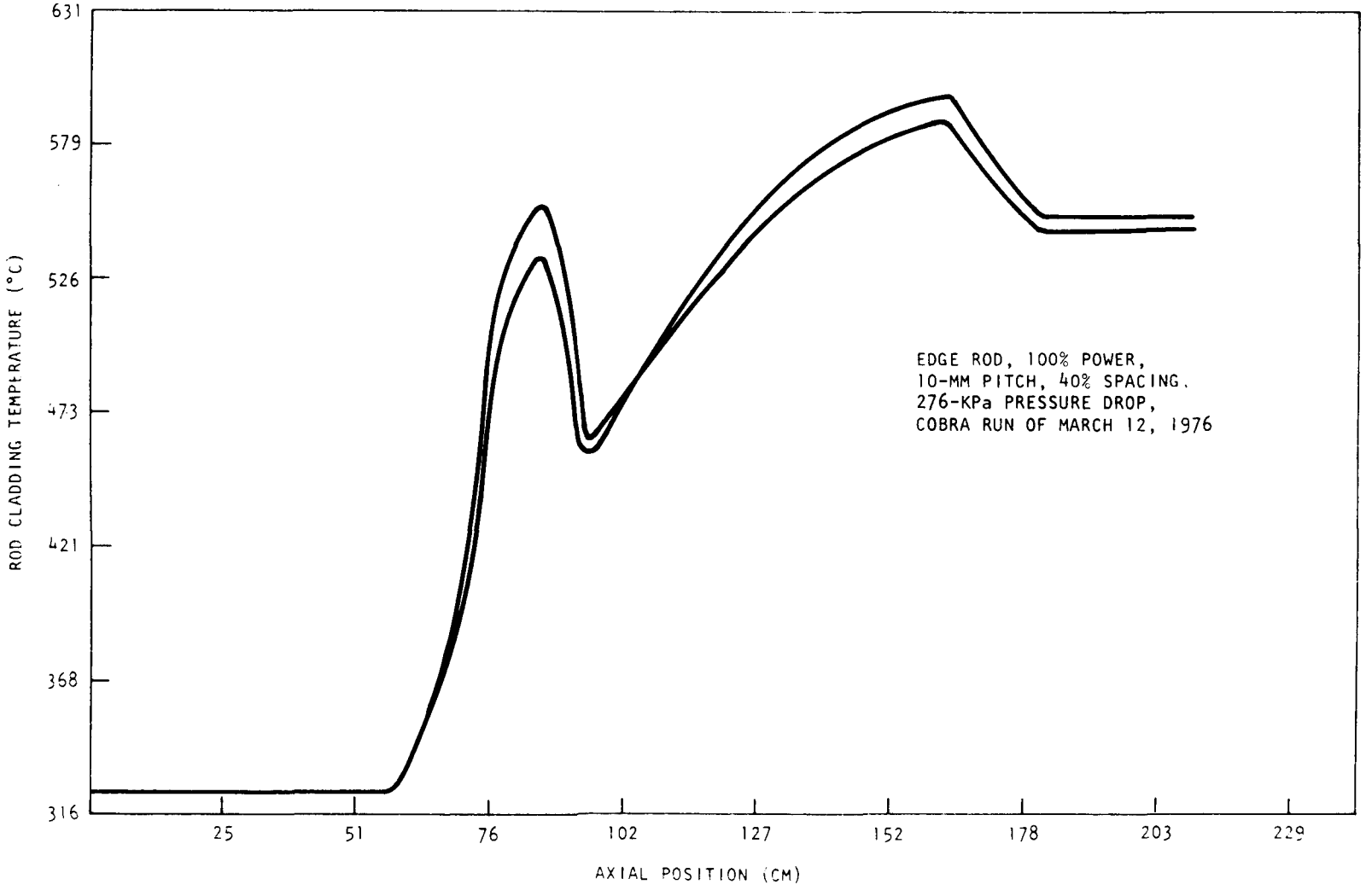

Fig. 6-3. 1976 rod temperature profile

TABLE 6-1
CRITICAL CRASIB RESULTS FOR 1975 AND 1976 TEMPERATURE PROFILES

	Maximum Distortion (mm)	Location (From Grid Plate) (mm)	Maximum Reaction Load (N)	Location (From Grid Plate) (mm)	End Reaction (N)	End Displacement (mm)
1976						
Beginning of life	0.16	2100	3.91	750	-0.93	0.16
6,000 hr	0.21	2100	2.76	1250	-0.09	0.21
12,000 hr	0.83	900	-3.91	1500	-0.67	0.10
18,000 hr	-1.37	1100	-3.91	750	-0.00	0.11
1975						
Beginning of life	-1.00	2100	4.98	2000	4.98	-1.00
6,000 hr	1.23	2100	1.69	1750	-0.22	1.23
12,000 hr	1.23	2100	1.24	1750	-0.67	1.23
18,000 hr	1.19	2100	0.18	1750	-0.09	1.19

6.4.4.3. Spacer Location Study. In an effort to reduce the large deflections given in Table 6-1, parametric study of the spacer locations was performed. The bowing distrotion using the reference design 250-mm spacer pitch and the 1976 temperature data is shown in Fig. 6-4. Figure 6-5 shows the results of introducing additional spacers and shortening the pitch. A 150-mm pitch gives deflections which are close to the 1972 predicted pitch.

6.4.4.4. Conclusions. The following conclusions were reached from this study:

1. Despite modifications, the CRASIB code presently operates in the same basic manner as it did in 1972.

2. The axial temperature profile has a pronounced effect on the bowing distortion in regard to magnitude and distorted shape. Greater accuracy in future thermal analysis (i.e., finer finite element grid) is warranted.

3. A reduction in grid spacer pitch to 150 mm in the fuel region should immediately be made since it requires only two additional spacers. Further study is required to determine the optimum location of these spacers and their effect on breeding ratio.

REFERENCES

6-1. Nuclear Systems Materials Handbook, Hanford Engineering Development Laboratory (TID-26666).

6-2. Olander, D. R., Fundamental Aspects of Nuclear Reactor Fuel Elements, 1976 (TID-26711-P1).

6-3. "Gas-Cooled Fast Breeder Reactor Quarterly Progress Report for the Period February 1, 1974 Through April 30, 1974," USAEC Report GA-A13021, General Atomic, June 1974.

6-4. "Reactor Development Program Progress Report," Argonne National Laboratory Report ANL-RDP-18, July 1973.

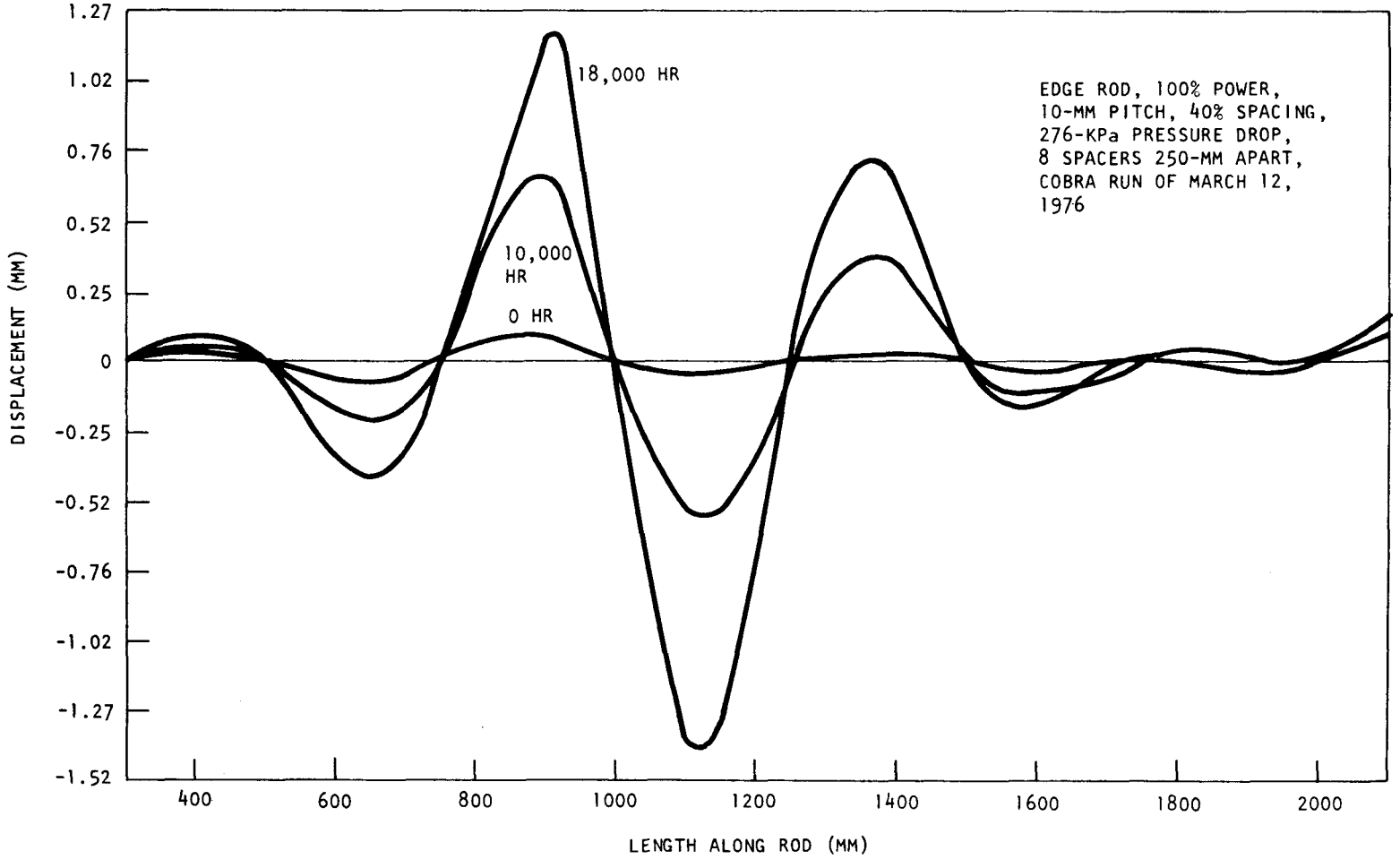

Fig. 6-4. Fuel rod bowing

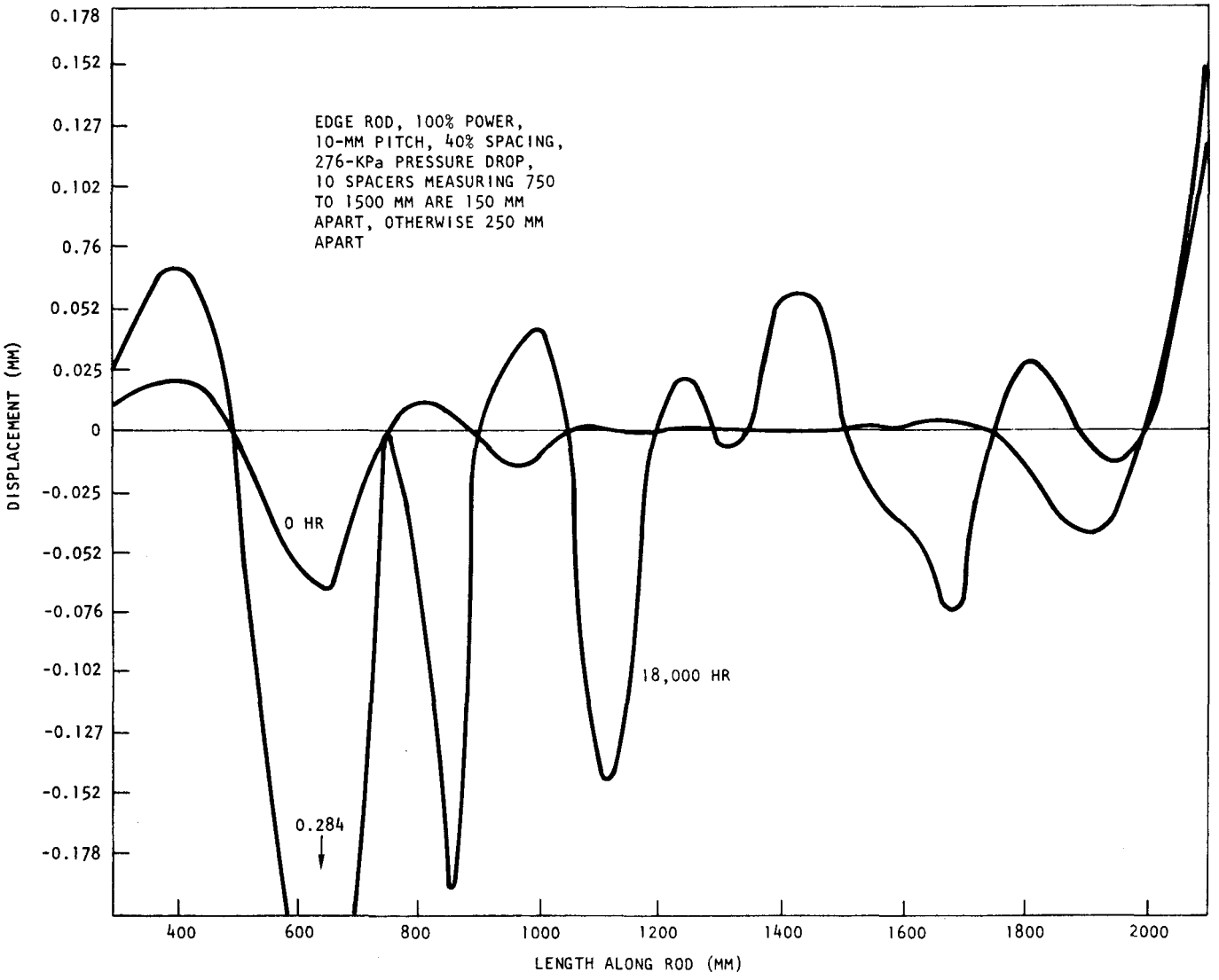

Fig. 6-5. Fuel rod bowing

6-5. Evans, E. A., "HEDL Quarterly Technical Report October, November, December 1974," v. 1, Hanford Engineering Development Laboratory Report HEDL-TME-74-4, February 1975.

6-6. Birney, K. R., and A. L. Pitner, "User's Manual for CONROD - A Computer Program for the Design Analysis of LMFBR Control Elements," Hanford Engineering Development Laboratory Report HEDL-TME-75-13, 1975.

6-7. Dutt, D. S., and R. B. Baker, "SIEX - A Correlated Code for Prediction of Liquid Metal Fast Breeder (LMFBR) Fuel Element Thermal Performance," Hanford Engineering Development Laboratory Report HEDL-TME-74-55, 1975.

6-8. Bard, F. E., Jr., "PECT-I: A FORTRAN IV Computer Program to Determine the Plastic-Elastic Creep and Thermal Deformations in Thick-Walled Cylinders," USAEC Report BNWL-1171, Battelle Northwest Laboratory, December 1969.

6-9. Homan, F. J., "Performance Modeling of Neutron Absorbers," Nucl. Technol. 6, 216-225 (1972).

6-10. "Compilation of Data and Descriptions for United States and Foreign Liquid Metal Fast Breeder Reactors," Hanford Engineering Development Laboratory Report HEDL-TME-75-12, August 1975.

6-11. "Evaluation of Compliant Grid Type Fuel Rod Spacers for FTR Fuel Assembly," Westinghouse Advanced Reactors Division Report WARD-3684-5, November 1968.

6-12. Kaplan, S., et al., "FTR Grid-Spaced Assembly Design Basis Report," General Electric Report GEAP-14002, May 1975.

6-13. "Gas-Cooled Fast Breeder Reactor Quarterly Progress Report for the Period August 1, 1972 Through October 31, 1972," USAEC Report Gulf GA-A12421, December 1972, pp. 10-21.

6-14. Jankus, V. Z., and R. W. Weeks, "LIFE-I: A FORTRAN-IV Computer Code for the Prediction of Fast-Reactor Fuel-Element Behavior," Argonne National Laboratory Report ANL-7736, November 1970, pp. 48, 49.

6-15. Cerbone, R. J., "Axial Fast Flux Distribution," General Atomic, private communication.

7. NUCLEAR ANALYSIS AND REACTOR PHYSICS (189a No. SU008)

The scope of activities planned under this subtask encompasses the validation and verification of the nuclear design methods which will be applied to the GCFR core design. This will primarily be done by direct evaluation of the methods with a critical assembly experimental program specifically directed toward GCFR development. Program planning and coordination activities, critical assembly design and analysis, and the necessary methods development will be carried out during the course of this program.

The major effort during the previous quarter was directed toward postanalysis of the as-built configurations of the phase II GCFR critical assembly, including the effect of a steel reflector added around the blankets. The effects of the ZPR-9 steel structure surrounding the phase I configuration were also studied. The phase II work included studies of neutron balance and the core-center conversion ratio. Analyses of steam worths in phases I and II continued. Cross-section preparation was completed for the pending postanalysis of phase III, which went critical on June 25, 1976. The prime accomplishment in methods development was a revision to the GFE4 code to enable self-shielding of resonance cross sections for the structural and fertile materials.

During this quarter, efforts were primarily directed toward postanalysis of experiments conducted in the phase II assembly. A major portion of this effort was concerned with refining the steam flooding calculation in the dry and the poisoned core configurations. Preliminary analyses of Doppler worth in the dry and the steam-filled core show reasonable agreement with experimental results. The calculations of boron control worths were also in good agreement with experimental results.

7.1. PHASE I GCFR CRITICAL ASSEMBLY

Work continued on refinements to the calculational methods for determining the worth of CH_2 insertion into the 5 x 5 drawer central zone of the phase I core. Twenty-eight-group 2DB calculations were carried out using two different sets of cross sections for the substitution region: one set used 28-group cell flux-advantage factors derived from a 28-group DTFX slab calculation, and the other used previously derived 10-group factors extended to the subgroups in the 28-group structure. The purpose of this study was to determine the sensitivity of the steam worth calculations to the precision of the heterogeneity adjustments applied to the cross sections. For the surrounding dry core media, the cross-sections were shielded with the 10- to 28-group expanded factors in both calculations.

A preliminary comparison of the DTFX-generated fuel plate shielding factors revealed that the expanded 10-group factors were suitable averages of the subgroup 28-group factors. This was borne out in the 2DB diffusion calculations for the 0.035 g/cm^3 CH_2 flooding worth, as shown in Table 7-1, where there was no difference due to the more approximate 10- to 28-group expansion for the heterogeneity factors. The variances from the earlier ADGAUGE cases cited in Table 7-1 are due to slight model differences and convergence problems encountered with ADGAUGE.

7.2. PHASE II GCFR CRITICAL ASSEMBLY

7.2.1. Postanalysis of Steam Entry Configurations

A detailed analysis of the full-core steam entry experiments in the 1300-liter phase II assembly was completed. Parallel 10- and 28-group calculations were carried out using cross sections based upon the same core and blanket GGC5 runs with ENDF/B-4 data; these were the spectrum calculations carried out for the preanalysis and do not include the effects of recent upgrading of GGC5 or the use of the more appropriately shielded cross sections generated with GFE4 for steel, uranium, and oxygen. Cell

TABLE 7-1
COMPARISON OF 28-GROUP RZ DIFFUSION CALCULATIONS OF CH_2 FLOODING WORTH IN CENTRAL ZONE OF PHASE I

Case	Diffusion Code	Calculation Method	Shielding Factors	Convergence	CH_2 Worth (Ih)
1	ADGAUG/STOER	Exact perturbation	10-group	10^{-5}	239.6
2	ADGAUG	Δk difference	10-group	10^{-5}	266.0
3	2DB	Δk difference	10-group	10^{-6}	253.4
4	2DB	Δk difference	28-group	10^{-6}	253.4

flux advantage factors for the 28-group cross sections were adopted from the 28-group phase-I DTFX results cited above with adjustments to the phase II cell based on 10-group phase I comparisons. Calculations with the Benoist formulism code PLADIF were run in both group structures to obtain the directional diffusion modifiers to account for streaming effects in the core and blanket void channels with and without the CH_2 inserted.

The analysis involved 2DB calculations for each of a dozen configurations constructed on ZPR-9 during the course of the flooding experiments using polyethylene foam. The variations included core radius, CH_2 loading, and installation of B_4C rods at the core center and in a seven-rod ring pattern. To maintain consistency with the calculations for the CH_2 flooded cases, the cross-section sets for the dry and wet media were derived from the GGC5 cases for which the "definition 2" option was chosen for evaluating transport cross sections. For the basic dry configuration (case A in Table 7-2), the switch from definition 1 to 2 reduced the 10-group eigenvalue from 0.99767 to 0.99675. Table 7-2 gives the 2DB results for the configurations, and the worths derived for specific configuration changes are discussed in the following sections.

7.2.2. Full-Core Steam Ingress Worth

Full-core and blanket steam ingress was simulated in phase II using polyethylene foam. A maximum channel density of about 0.0175 g/cm^3 was achieved with perforated foam slabs inserted into all void channels. These experiments were carried out in the reflected phase II configuration, but no CH_2 additions were made in the reflector regions. The GA-planned loading sequence in Table 7-2 gives steam worth data under a variety of conditions; of primary importance is the effect of poison rod loadings upon steam worth, a situation directly comparable to conditions in an operating reactor.

Table 7-3 compares the results of calculations and measurements for the worth of the maximum-density CH_2 flooding in the configurations. As in the phase I scoping studies, the worths were positive and increased with CH_2 density. Also similar to the phase I study, the 28-group analysis gave

TABLE 7-2
SUMMARY OF CALCULATIONS FOR PHASE II STEAM WORTH EXPERIMENTS

Configuration	Core Radius (cm)	B_4C Rods Installed	CH_2 Density in Voids (g/cm^3)	Measured k[(a)]	Calculated Eigenvalues, 2DB Diffusion (RZ) With Definition 2 σtr	
					10-Group	28-Group
A	56.88	None	0	1.00068	0.99675	0.99798
B	54.79	None	0	~0.9891	0.98207	0.98338
C	54.79	None	0.0088	~0.9912	--	--
D	54.79	None	0.175	~0.9945	0.99343	0.99604
E	56.10	None	0.175	1.00134	1.00214	1.00468
F	56.10	Center	0.175	0.99573	0.99548	0.99809
G	56.10	Center + 7-rod ring	0.175	0.9805	0.97326	0.97586
H	59.38	Center + 7-rod ring	0.175	0.99880	0.99341	0.99580
I	59.38	Center + 7-rod ring	0.0088	--	--	--
J	59.38	Center + 7-rod ring	0	0.99671	0.99084	0.99183
K	56.10	Center + 7-rod ring	0	0.9769	0.96929	0.97038
L	56.10	Center	0	0.99138	0.98587	0.98712
M	56.10	None	0	0.99631	0.99141	0.99266

(a) Using ANL conversion factor, i.e., 974.8 Ih per $\Delta k/k$.

TABLE 7-3
ANALYSIS OF STEAM FLOODING EXPERIMENTS IN FULL CORE
AND BLANKETS OF PHASE II GCFR CRITICAL ASSEMBLY

Assembly Configuration		Measured Worth 0.0175 g/cm CH_2 in Void Channels[a] (Ih)	Flooding Worths Calculated by Δk Difference, RZ Diffusion Calculation			
			10-Group Calculation		28-Group Calculation	
Core Radius (cm)	Simulated B_4C Control Rods Installed		Ih	C/E	Ih	C/E
54.79	None	528 ± 10	1096.6	2.08	1218	2.31
56.10	None	488.8 ± 2.0	1017.3	2.08	1135	2.32
56.10	1 at core center	428.2 ± 4.0	922.4	2.15	1049	2.45
56.10	Center + 7-rod ring	361.4 ± 46	396.4	1.10	545	1.51
59.38	Center + 7-rod ring	203.4 ± 2	246.0	1.21	378.6	1.86

[a] Reference 7-1.

consistently more positive CH_2 worths than the 10-group analysis. It is encouraging to note qualitative agreement of the calculations with experimental results for the negative effect on flooding worth of B_4C poisoning and increased core radius. However, for the clean configurations, the factor of two calculational discrepancy is disappointing, considering the relative success of the phase I analysis for central-zone flooding. The discrepancy in phase II can most likely be traced to diffusion parameters for the full core and blankets since leakage played a minor role in the central-zone study.

7.2.3. Worths of Simulated B_4C Control Rods

The steam flooding program for phase II included installations of simulated control rods to determine the influence of steam on control performance. Each mock-up rod consisted of a core-length (121.9 cm) column of 1.27 x 5.08 x 15.24 cm plates (steel clad) of natural B_4C with a total loading of about 220 g of B-10 per column. The rods were installed in place of 1.27-cm columns of steel void sleeves in core drawers at eight locations, i.e., the central core drawer and a ring of seven drawers at a radius which was 70% of the core radius.

Table 7-4 gives the calculated rod worths derived from differences in eigenvalues for the Table 7-2 configurations and compares them with the experimental worths. Only minor differences were noted between the 10- and 28-group results. In general, the agreement with the measurements was good, considering that no exact rod cell calculations were performed to determine self-shielding factors for the boron cross sections. Further studies are required for proper evaluation of the self-shielding effects and determination of a possible discrepancy introduced by the asymmetric seven-rod ring pattern.

7.2.4. Uranium Doppler Coefficient at Core Center

The Doppler effect in uranium over a temperature range of 300 to 1100 K was measured at the core center in the unreflected, dry phase II

TABLE 7-4
ANALYSIS OF SIMULATED B_4C CONTROL ROD WORTHS IN PHASE II
GCFR ASSEMBLY WITH AND WITHOUT STEAM INGRESS

CH_2 Density in Void Channels (g/cm^3)	B_4C Rods Inserted (220 g B-10 in Core-Length Column)	Total Worth of Installed B_4C Rods (Ih)			28-Group Calculated-to-Experimental Ratio
		Measurement[a]	Diffusion Theory Calculations		
			10-Group	28-Group	
None	Core center	-484 ± 2	-534	-533	1.10
None	Center + ring	-1934 ± 35	-2168	-2177	1.13
--	--	--	--	--	--
0.0175	Core center	-545 ± 4	-629	-619	1.14
0.0175	Center + ring	-2061 ± 47	-2789	-2769	1.34

[a] Reference 7-1.

configuration and the 0.0175-g/cm^3 CH_2-flooded configuration with reflector. The UO_2 sample used was about 2.5 cm in diameter and 30.5 cm long, giving a measured effect over ±15 cm from the midplane. Exact modeling of this sample in spectrum and transport cell calculations has not yet been carried out. However, the GGC5 cases for the U_3O_8 plate in the phase II core cell with and without CH_2 were rerun with the U_3O_8 at 1100 K. Table 7-5 compares the analysis for the 300- to 1100-K Doppler effect in U-238 (using the hot U_3O_8 cross sections) with ANL measurements. Both group structures give reasonable predictions for the Doppler effect in the dry case, but the effect in the steam-flooded configuration is better calculated using the finer group structure.

In these experiments, doubling of the uranium temperature feedback effect due to 0.0175 g/cm^3 of CH_2 ingress (equivalent to 0.0225 g/cm^3 of H_2O in coolant channels) is adequately predicted and lends credence to the negative steam ingress reactivity effect expected in a hot, operating GCFR demonstration plant. Indeed, calculations for the phase II rodded configuration with hypothetical heating of all the core U_3O_8 to 1100 K (using the above-cited hot U-238 cross section) gave a flooding worth reduction of \$0.77 to \$0.17; extrapolation to all the core uranium (in U_3O_8 and Pu-U-Mo plates) indicates a -\$0.76 worth in a hot, rodded core having a volume of 1300 liters.

7.3. ANALYSIS OF SAFETY PARAMETERS

A paper on the analysis of safety-related physics measurements in the initial GCFR critical experiments (Ref. 7-2) was prepared for presentation at the International Meeting on Fast Reactor Safety and Related Physics. This paper followed an ANL paper on the measurements and experimental results (Ref. 7-3). Reference 7-1 summarizes the conclusions of the critical experiments to date as follows:

1. Fuel and cladding worths can be predicted with approximately the same confidence for the GCFR as for the LMFBR; i.e., there are similar bias factors.

TABLE 7-5
ANALYSIS OF 300- TO 1100-K URANIUM DOPPLER EFFECT AT CENTER OF PHASE II GCFR ASSEMBLY WITH AND WITHOUT SIMULATED STEAM INGRESS

Assembly Configuration	Measurement in Depleted Uranium Sample (Ih/kg)[a]	First-Order Perturbation Calculations for U-238			
		10-Group Analysis		28-Group Analysis	
		Ih/kg	Calculated/Experimental	Ih/kg	Calculated/Experimental
Unflooded					
Core radius = 58 cm, no reflector outside blankets	-0.623 ± 0.009	-0.612	0.98	-0.654	1.05
Flooded with 0.0175 g/cm^3 of CH_2 in channels					
Core radius = 56 cm, with steel reflector	-1.200 ± 0.010	-1.507	1.26	-1.302	1.08

[a]Reference 7-1.

2. The worth for helium depressurization in a GCFR is adequately predicted.

3. Individual control rod worths appear to be predicted reasonably well by eigenvalue difference techniques, although more rigorous analyses as well as studies of rod banks and rod interactions in future GCFR critical assemblies are needed.

4. Accurate calculation of steam ingress effects requires that careful attention be paid to energy mesh, spectrum averaging, and leakage parameters. Investigations of the methods involved are needed to reduce the calculational discrepancy for full-core flooding.

5. Steam entry into a hot, poisoned GCFR, expected to be a negative worth, will increase the negative prompt temperature feedback coefficient via the increased U-238 Doppler effect, thus enhancing safety performance. Conversely, however, the hot-to-cold shutdown rod worth requirements are slightly greater.

7.4. METHODS DEVELOPMENT

7.4.1. Cross-Section Processing (GFE4)

Work continued on the revision and debugging of the GFE4 code which processes ENDF/B-4 tapes to produce 99-group data for the GAM tapes used by GGC5. A minor error was found which required reprocessing of some recently processed ENDF/B-4 data sets for self-shielded materials. Memos were issued with input instructions for the current production version.

Studies were initiated toward expansion of GFE4 code dimensioning to accommodate expected revisions to version 5 of ENDF/B. The potential for a finer GAM group spacing, e.g., the 239-group 4-C structure, is also being explored.

7.4.2. Broad-Group Cross-Section Production (GGC5)

A number of changes were made in the GGC5 broad-group cross-section code. The major items included

1. Correction of a long-standing error in the B_2 and B_3 solution algorithms which had caused discrepancies in the generation of microscopic transport cross sections.

2. Addition of a broad-group-dependent input buckling option.

3. Addition of an option to mix fission spectra.

4. Elimination of the use of the fast results tape as an internal scratch file for greater reliability and speed.

5. Addition of extended edits for 1-group macroscopic parameters.

The group-dependent buckling option has been tested with GGC5 runs for typical radial and axial blanket configurations in which there are severe positive and negative variations of the region-average bucklings with energy. Before broad-group averaging of the transport cross sections, all the fine-group currents are set positvie to assure positive transport cross sections. This procedure yields good agreement of GGC5 broad-group spectra with corresponding region-average spectra output from diffusion calculations.

7.4.3. Diffusion Theory Codes (2DB, 3DB)

Final modifications were made to the new version of 2DB which incorporated Chebyshev extrapolation of fluxes instead of fission sources, multiple file flux input/output tapes, upscatter capability, atom density restart capability, and several improved edits. A production version was checked out during regular usage and has been added to the GA Computer

Center Archive Library. An updated manual of input instructions for this version of 2DB has been drafted. As part of the effort to further extend available diffusion theory methods, work was initiated on a subregion capability in 2DB, and the 3DB code was compiled and indexed.

7.4.4. Perturbation Theory Codes (PERT-5)

Revisions to the Battelle Northwest Laboratory PERT-5 code were completed, which rendered the package compatible with output tapes from the updated version of 2DB, i.e., with multiple-problem flux files, upscatter capability, etc. A much faster calculational algorithm was developed for evaluating effective delay neutron parameters, and a regionwise reactivity coefficient option was added. A production version of PERT with all new capabilities has also been added to the Computer Center Archive Library, and a revised input manual is in preparation. Newer revisions to PERT under study include a groupwise edit of region leakage parameters.

REFERENCES

7-1. Bhattacharyya, S. K., Argonne National Laboratory, private communication.

7-2. Moore, R. A., and A. L. Hess, "Analysis of Safety-Related Physics Measurements in the Initial Gas-Cooled Fast Breeder Reactor Critical Experiments," in Proceedings of the International Meeting on Fast Reactor Safety and Related Physics, Chicago, October 1976.

7-3. Bhattacharyya, S. K., et al., "Experimental Studies of GCFR Safety Physics Parameters in the ZPR-9 Critical Assemblies," in Proceedings of the International Meeting on Fast Reactor Safety and Related Physics, Chicago, October 1976.

8. SHIELDING REQUIREMENTS (189a No. SU008)

The purposes of the shielding task are to verify the adequacy of the methods and data (physics and engineering) for the design of GCFR shields and to evaluate the effectiveness of various shield configurations. This task also coordinates and provides liaison with the analytical and experimental GCFR shielding activities at ORNL.

During the last quarter, grid plate shielding studies were continued to obtain a revised design which satisfied the grid plate design criterion requiring a minimum residual ductility of 10% based on total elongation; analysis of a revised upper axial shield was also initiated. The results of the grid plate shield calculations provided a source for bootstrapping two-dimensional transport calculations.

During this quarter, a topical report summarizing the physics design of the revised grid plate shielding conducted during FY-76 was prepared. A Monte Carlo calculation of the revised grid plate shielding, including the fuel rod lattice, was initiated to assess the effect of rod streaming on neutron-induced damage to the grid plate. The DOT-III two-dimensional calculations of the revised lower shield and wraparound shield performed by ORNL were received, and the first set of DOT-II two-dimensional calculations of the revised upper axial shield were completed.

8.1. GRID PLATE SHIELDING DESIGN

Results of analyses leading to an optimum revised grid plate shielding design satisfying the conflicting requirements of shielding and helium flow were reported during the last two quarters (Refs. 8-1 and 8-2). These analyses are presented in detail in Ref. 8-3. Discrete ordinate transport theory was used to estimate the maximum neutron flux and the neutron spectrum at the grid plate. Calculational uncertainties were incorporated by

applying a bias factor of two to the calculated grid plate fluence. Damage function analysis was utilized to evaluate the lower-bound (95% confidence) fluence limit corresponding to the limiting grid plate material property level of 10% residual ductility based on total elongation.

The primary uncertainty associated with the grid plate shielding design is the assumption of a homogenized core and blanket, which neglects the effect of neutron streaming in the rod lattice and between adjacent fuel assembly walls on the source emerging at the top of the axial blanket. In order to assess the impact of rod streaming on the grid plate, a Monte Carlo analysis of grid plate irradiation was initiated.

8.1.1. Overview of Rod Streaming Effects

Radiation streaming is a primary consideration in the shielding design for the GCFR. Neutron streaming in the rod lattice of the core and blankets increases the neutron source for the grid plate shield region, which in turn impacts the flux levels in the upper plenum region and the ducts leading to the helium circulators. The neutron source for the lower plenum is similarly increased as a result of axial neutron streaming.

Since two-dimensional discrete ordinate methods are not adequate for calculation of rod streaming, the cumbersome Monte Carlo method must be utilized. Rod streaming is limited to neutrons which suffer no, or perhaps only one or two, collisions in the forward direction, so that they leave the rod lattice in a small solid angle in the upward direction, toward the grid plate. Results reported in Ref. 8-4 for a MORSE Monte Carlo calculation for the GCFR rod geometry case indicate that neutron streaming increases axial leakage from the axial blanket by about 25% (95% confidence) when compared with a corresponding Monte Carlo calculation assuming a homogenized core and blanket. This additional leakage results in a similar increase in the flux impinging on the grid plate. However, since the increase in leakage due to rod streaming results in a harder spectrum emerging from the blanket and incident on the grid plate, the damage response would increase by somewhat more than 25% at the 95% confidence level. The Ref. 8-4 Monte

Carlo analysis did not yield statistics which were adequate for quantifying the effect of rod streaming on the leakage spectrum.

The shielding program comprises concurrent efforts at GA and ORNL to quantify the effect of rod streaming early in the shield development in order to avoid costly design margins. Validation of available Monte Carlo methods for calculating rod streaming is being provided by a GCFR rod streaming experiment recently completed at the ORNL tower shield facility (Ref. 8-5). General Atomic and ORNL will perform Monte Carlo analyses of rod streaming problems during FY-77 to determine suitable Monte Carlo techniques and the extent of additional experimental efforts required to validate calculational methods.

Section 8.1.2 describes the initial calculation, which is designed to estimate the effect of rod streaming on the energy-dependent angular flux emerging from the axial blanket. The results of this calculation together with the results of Ref. 8-3 will provide the knowledge necessary for developing methods, such as biasing procedures, to be used in more extensive analyses.

8.1.2. Analysis of Rod Streaming

8.1.2.1. Transport Calculations. In order to assess the effect of rod streaming on the energy-dependent angular neutron flux emerging from the axial blanket, two Monte Carlo calculations were performed using the MØRSE program (Ref. 8-6). The first calculation was for the GCFR heterogeneous rod geometry, and the second was for a homogeneous geometry. In both cases, advantage was taken of the symmetry in the central fuel assembly in order to model a 30-deg segment of the central fuel assembly (Fig. 8-1) extending from the core midplane to the top of the inlet manifold. The following three axial zones were considered for both geometries (Fig. 8-2):

1. Beginning of life, core zone 1.
2. Axial blanket, including equilibrium Pu-239.
3. Spring, fission product trap, and inlet manifold region.

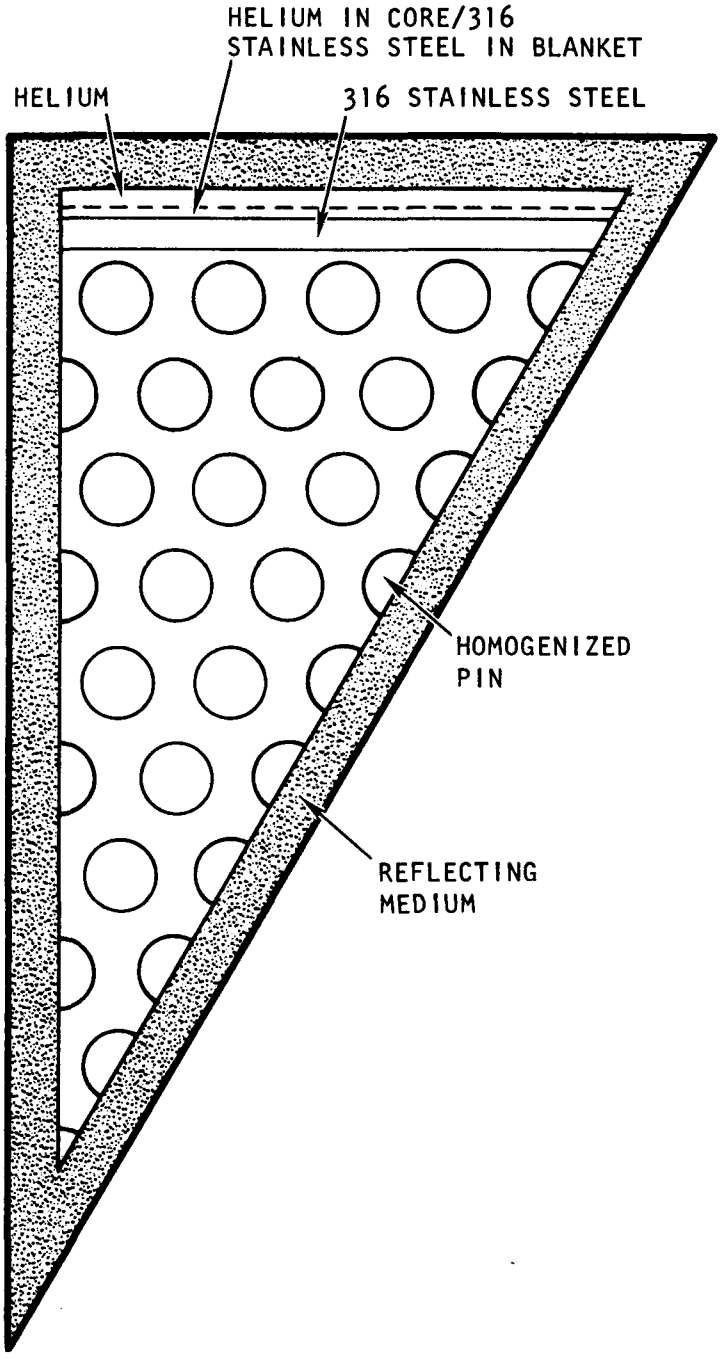

Fig. 8-1. Horizontal cross section of heterogeneous model for MORSE calculation

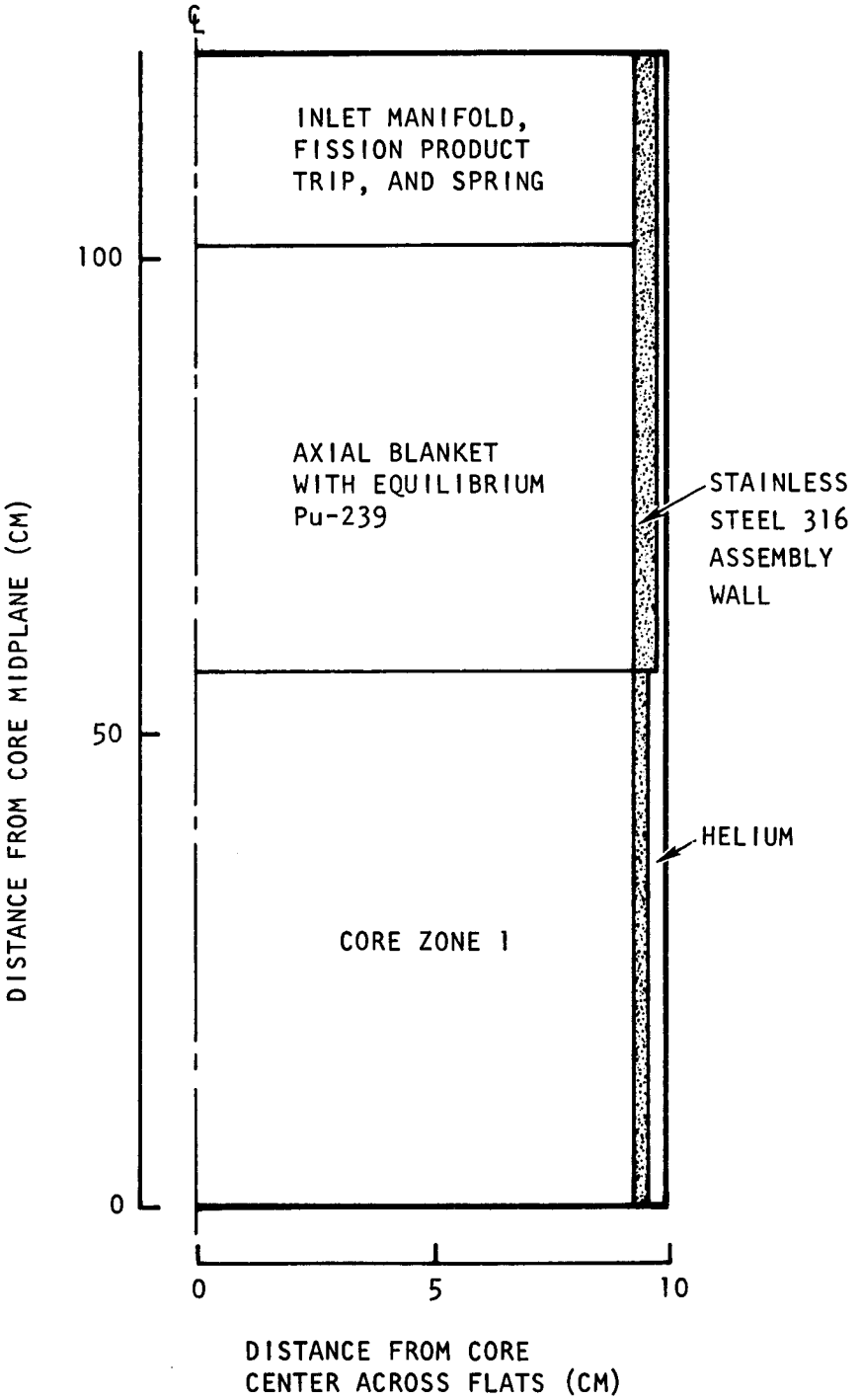

Fig. 8-2. Axial zoning for heterogeneous and homogeneous MORSE calculations

The equilibrium Pu-239 was uniformly distributed in the axial blanket; this distribution is conservative because a large portion of the blanket fission source is located near the top of the rod lattice. The geometrically complex inlet manifold was represented by the rod geometry. For the heterogeneous case, the fuel assembly wall and the helium gap between adjacent assembly walls were also modeled. For both geometries, a reflective medium was assumed at the 30-deg-segment boundaries; specular reflection was also assumed.

The distributed fission source was obtained from the 1DFX calculation described in Ref. 8-3. The calculation used ten-group (nine fast, one thermal) P_3 cross sections. Source position biasing was employed so that more particles were selected near the top of the core and blanket. Source direction biasing was employed to enhance the sampling of upwardly directed particles. Source energy biasing was deemed unnecessary since the fission spectrum was peaked over the important energy range. Each calculation utilized 17 particle batches, with 75 particles per batch. Splitting, Russian roulette, and exponential transform with PATH = 0.5 were employed.

8.1.2.2. Results. Results were obtained for total flux, energy spectra, and angular distributions (with respect to the +z axis only) for the six detector positions indicated in Table 8-1. Table 8-1 also gives the total fluxes for the two geometries. All results were normalized to one source particle per second, so that the absolute flux values may be obtained by multiplying the normalized results by the total number of fissions in the 30-deg fuel assembly section. The fractional standard deviations vary from 0.13 to 0.44 and increase, as expected, with increasing z.

Rod streaming increases the total flux at the top of the inlet manifold (detector 5) by 5% for the nominal result and by $[1.05\ (1.44)^2 - 1]100 = 118\%$ at the 2σ confidence level. These statistics are inadequate for design purposes but enable some qualitative conclusions to be drawn. Note that the ratio of the fluxes for the heterogeneous to homogeneous cases is 1.17 at the top of the core (detector 1) and 1.70 at 15 cm above the

TABLE 8-1
TOTAL FLUX RESPONSE FOR MORSE CALCULATIONS

Detector	Detector Type	Distance From Core Midplane (cm)	Detector Position	Response (n/cm^2-s)		
				Homogeneous	Heterogeneous	Heterogeneous/ Homogeneous
1	Flux	56.5	Top of core	6.65-2 (9)[a]	7.75-2 (10)	1.17 (13)
2	Flux	71.5	15 cm above core - axial blanket interface	3.71-2 (10)	6.30-2 (14)	1.70 (17)
3	Flux	86.5	30 cm above core - axial blanket interface	2.73-2 (18)	3.83-2 (17)	1.40 (25)
4	Flux	101.5	Top of axial blanket	1.39-2 (21)	1.49-2 (25)	1.07 (33)
5	Flux	121.5	Top of inlet manifold	2.33-3 (35)	2.45-3 (27)	1.05 (44)
6	Current	121.5	Top of inlet manifold	1.18-3 (26)	1.60-3 (26)	1.36 (37)

[a] Read as 6.65×10^{-2}. Numbers in parentheses indicate percent standard deviation.

core - axial blanket interface. This ratio decreases with increasing z to 1.05 at the top of the flow manifold. The variation of the ratio can be understood by realizing that the flux in the blanket near the core - axial blanket interface is dominated by neutrons originating in the core. Source neutrons from the core stream upward into the blanket in the helium channels, contributing significantly to the flux near the interface. However, the ratio decreases with increasing z as a result of attenuation of the core streaming component in the blanket, indicating that (1) the streaming component is not highly collimated, (2) streaming is a localized effect, and (3) streaming of neutrons originating in the blanket may be more important than streaming of neutrons originating in the core.

The results also indicate that the effect of rod streaming is probably a nominal increase in the flux emerging from the blanket. It appears that the ratio of the helium channel area to channel length is an important parameter; the probability is low that a neutron originating in the core will suffer a sequence of collisions enabling it to stream upward out of the core and through the blanket.

The poor statistics preclude any definitive conclusions regarding the difference between the emergent particle energy and the angular distribution of the homogeneous and heterogeneous geometries. However, the expected trend of a harder, more forward-peaked flux was evident for the heterogeneous case. Considerably more particle histories are required if adequate statistics are to be obtained for quantifying the effect of streaming on the energy and angle flux dependence.

The results of these analyses will be used to make further refinements to the Monte Carlo methods (e.g., more elaborate biasing techniques). These modified methods will then be used to solve the combined rod region and grid plate region problem.

8.2. REVISED LOWER AXIAL AND WRAPAROUND SHIELDING

8.2.1. One-Dimensional Results

The revised lower axial and wraparound shielding was described in Ref. 8-1; the initial lower and wraparound shielding is shown in Fig. 8-1 of Ref. 8-1. After performing one-dimensional calculations at GA, as described in Ref. 8-1, a revised model of the lower axial and wraparound shielding was developed and is shown in Fig. 8-3.

8.2.2. Two-Dimensional Results

The two-dimensional DOT-III calculations of the revised lower axial and wraparound shielding were received from ORNL near the end of this quarter; consequently, a thorough study of the results has not been completed. However, preliminary review of the results (see Figs. 8-4 through 8-6) indicates that (1) the fluence at the liner above the wraparound shield is marginally below the fluence required to attain the liner 75°C nil-ductility temperature shift limit; (2) gamma heating of the concrete behind the wraparound appears to be marginal; and (3) the gamma dose to the PCRV tendons appears to be marginal. Figure 8-4 presents two-dimensional isoflux plots of total neutron flux (n/cm^2-s) in the lower axial assembly; Fig. 8-5 gives two-dimensional isoheating plots for gamma heating (mW/cm^3) in the PCRV concrete in the vicinity of the lower axial shield assembly; and Fig. 8-6 shows isodose plots for the gamma dose rates (rad/s) in the concrete.

In Fig. 8-4, the anticipated neutron damage critical areas were (1) behind the wraparound shield at the liner in the region below the outer radial shield and (2) above the wraparound shield at the liner. The critical isoflux level behind the wraparound shield is contour A of Fig. 8-4, which represents a total flux of 1.0×10^{11} n/cm^2-s. The corresponding total fluence is 7.6×10^{19} n/cm^2 (24 full-power years), which would marginally meet the liner fluence limit corresponding to the spectrum at the liner at the level of the core midplane. However,

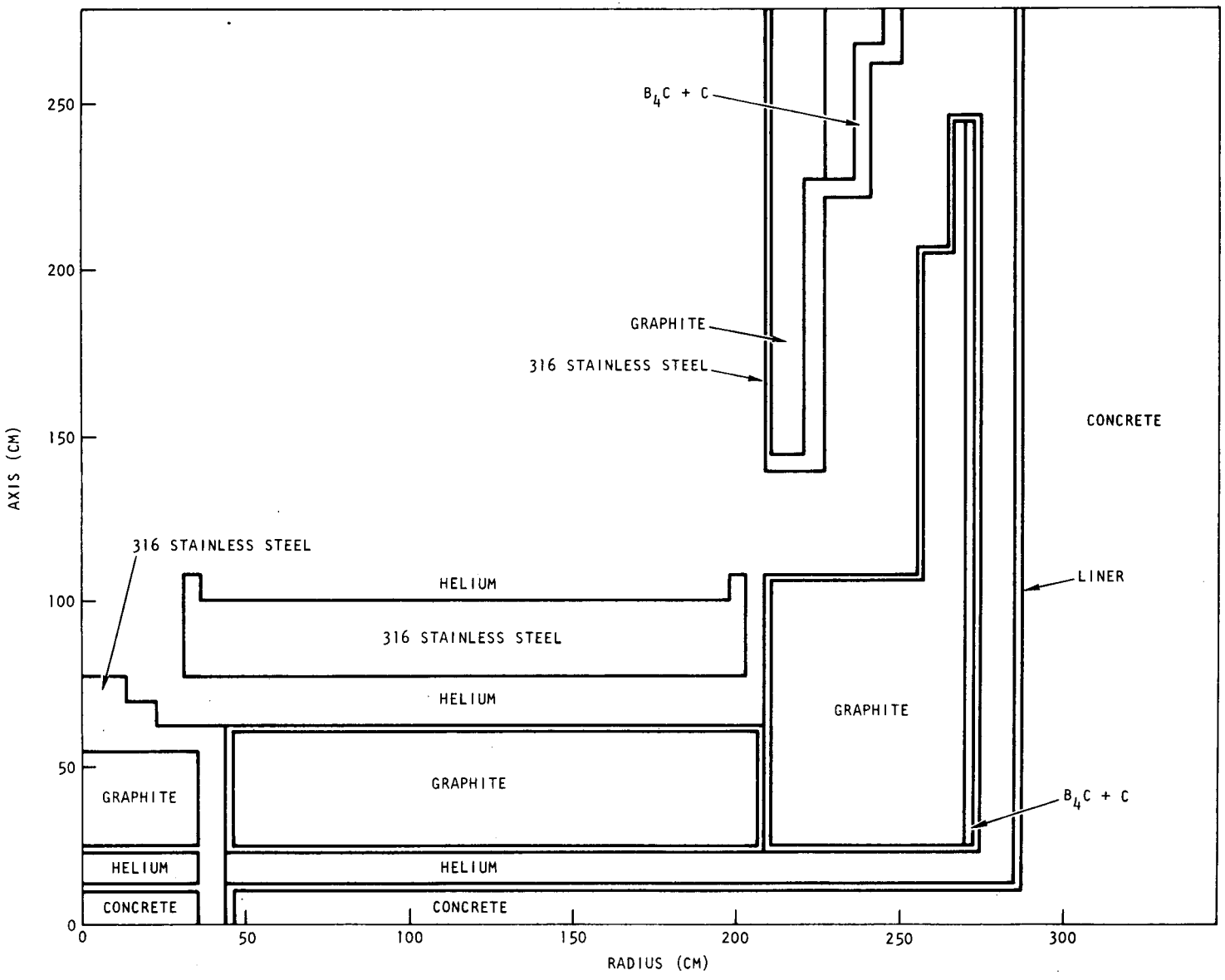

Fig. 8-3. 300-MW(e) GCFR lower axial shield and wraparound model for two-dimensional calculations

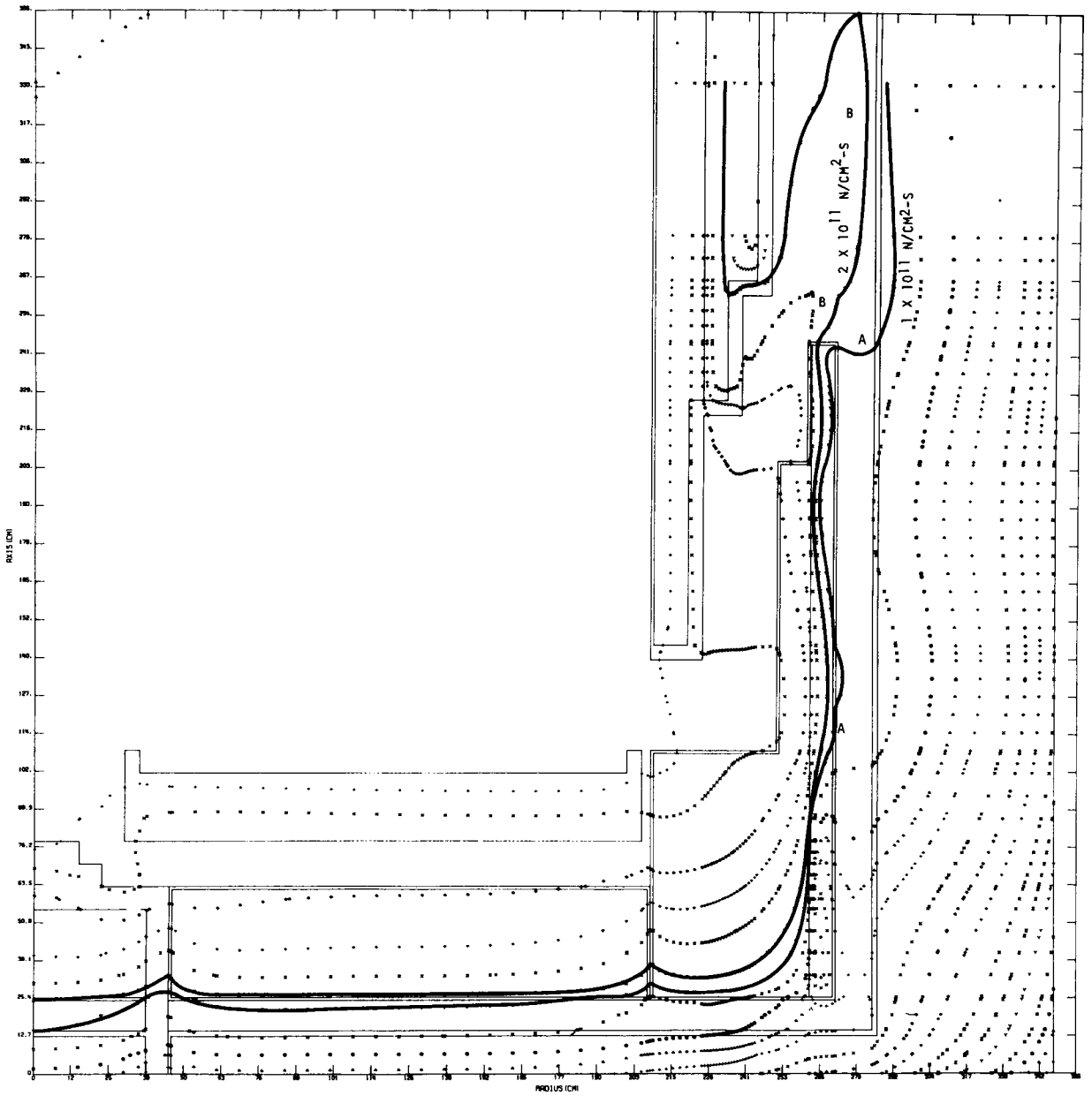

Fig. 8-4. Total neutron flux for lower axial shield assembly

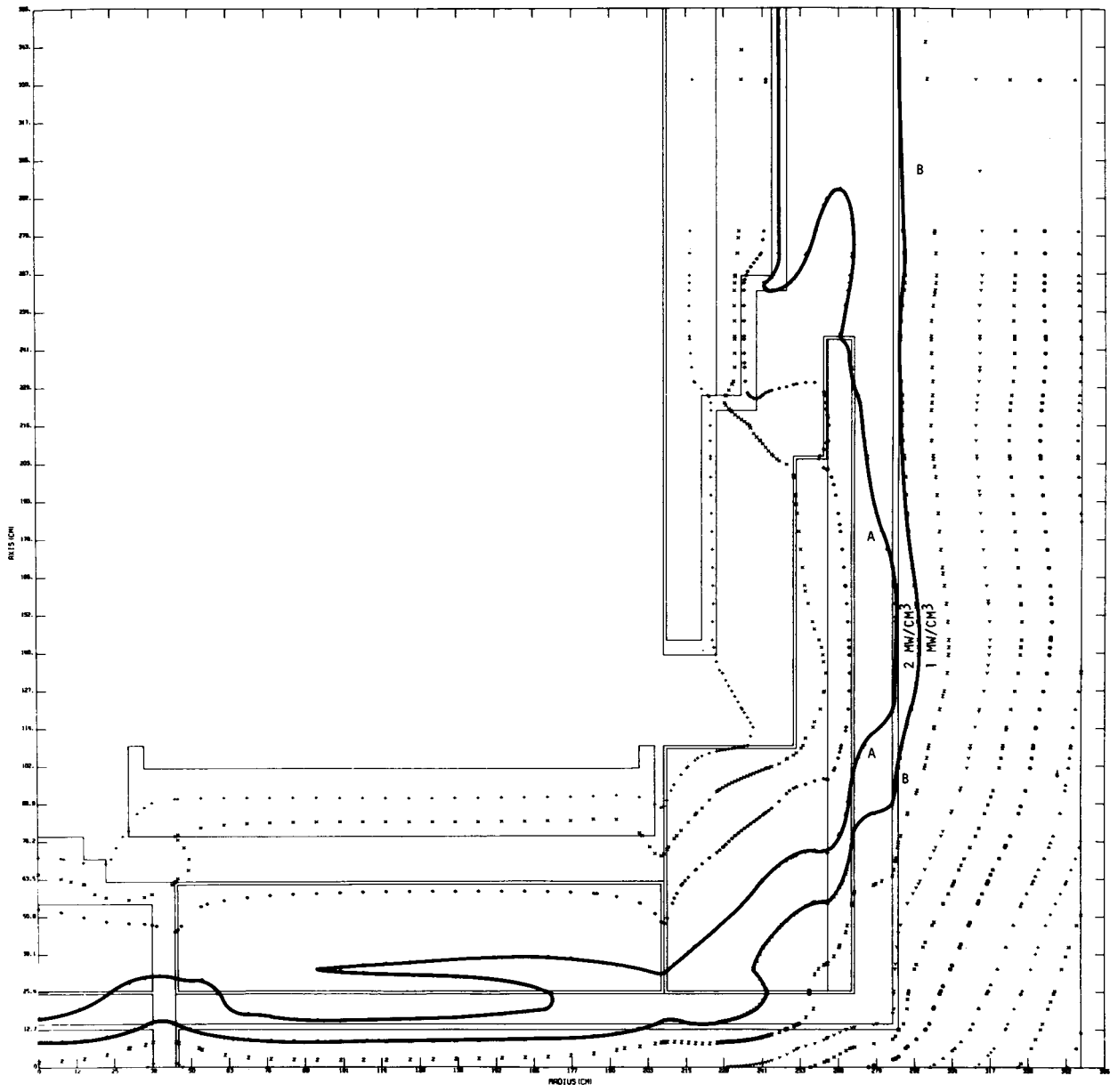

Fig. 8-5. Concrete gamma heating for lower axial shield assembly

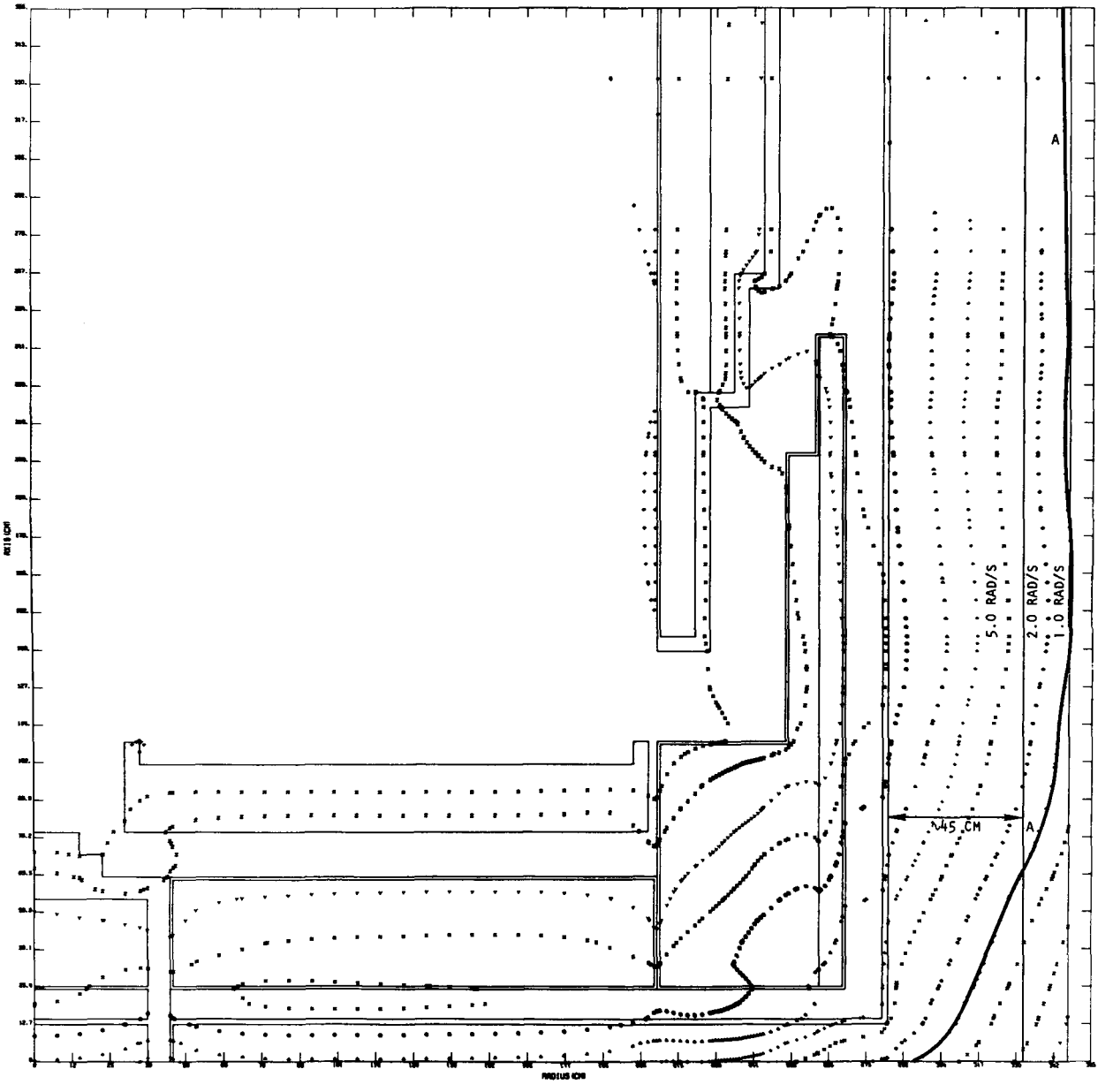

Fig. 8-6. Gamma dose rate in concrete for lower axial shield assembly

since the spectrum at the liner near the wraparound shield is considerably softer than that at the core midplane level, a new fluence limit will have to be determined. The resulting critical isoflux level above the wraparound shield is contour B of Fig. 8-4, which represents a flux of 2.0×10^{11} n/cm^2-s, or a 24-yr fluence of 1.5×10^{20} n/cm^2. However, a new fluence limit corresponding to a 75°C nil-ductility temperature shift will have to be calculated for this region as well.

In Fig. 8-5, the anticipated concrete gamma heating critical areas were the same as those for the total neutron flux damage. Figure 8-5 shows that the calculated gamma heating rate in the concrete behind the wraparound shield is nearly 2 mW/cm^3 (contour A), and that above the wraparound shield in the concrete, more than 1 mW/cm^3 (contour B). Since the design limit is 1 mW/cm^3, the present calculations must be reviewed.

Figure 8-6 presents the gamma dose rates in the concrete. The PCRV tendon lubricant dose limit is 10^9 rad, which corresponds to the 1-rad/s isodose contour labeled A in Fig. 8-6. This contour essentially represents the tendon lubricant dose limit for 24 yr, or 7.6×10^8 s. The vertical line at a radius of about 332 cm is the approximate innermost position of the vertical reinforced concrete tendons. Consequently, nearly the entire tendon length below the core appears marginal.

A review of the gamma dose and gamma heating calculations is necessary so that new shielding designs can be developed to alleviate the three problems noted: the 75° nil-ductility temperature shift damage at the liner; the gamma heating in the concrete; and the gamma dose at the tendons.

8.3. REVISED UPPER AXIAL SHIELD

The revised upper axial shield and the initial reference upper axial shield are discussed in Ref. 8-2. During this quarter, the first part of the DOT-II two-dimensional transport calculations for the revised upper axial shield was completed. This part includes the shield and upper plenum between the grid plate (surface source) and the level of the plane defined

by the inlet coolant duct axes. As in the grid plate shielding calculations, S_8 symmetric quadrature and P_3 anisotropic scattering with ten energy groups were used in DOT-II. The second part of the problem begins at the level of the plane defined by the inlet coolant duct axes and continues upward through the shield covering the lower face of the reactor cavity closure. The results from both calculations will be discussed in the next quarterly report.

REFERENCES

8-1. "Gas-Cooled Fast Breeder Reactor Quarterly Progress Report for the Period February 1, 1976 Through April 30, 1976," ERDA Report GA-A13868, General Atomic, May 31, 1976.

8-2. "Gas-Cooled Fast Breeder Reactor Quarterly Progress Report for the Period May 1, 1976 Through July 31, 1976," ERDA Report GA-A13975, General Atomic, August 31, 1976.

8-3. Perkins, R. G., and R. J. Cerbone, "Physics Design of the 300-MW(e) Gas-Cooled Fast Breeder Reactor Demonstration Plant Grid Plate Shielding," ERDA Report GA-A14124, General Atomic, September 30, 1976.

8-4. "Gas-Cooled Fast Breeder Reactor Quarterly Progress Report for the Period February 1, 1975 Through April 30, 1975," ERDA Report GA-A13458, General Atomic, July 31, 1975.

8-5. Slater, C. O., and D. E. Bartine, "Analysis of the GCFR Pin Streaming Experiment Performed at the TSF," Trans. Am. Nucl. Soc. 23, 624 (1976).

8-6. "MORSE-CG: A General Purpose Monte Carlo Multigroup Neutron and Gamma-Ray Transport Code With Combinatorial Geometry," Computer Code Collection Report CCC-203, Oak Ridge National Laboratory Radiation Shielding Information Center, August 1973.

8-7. "Gas-Cooled Fast Breeder Reactor Quarterly Progress Report for the Period August 1, 1975 Through October 31, 1975," ERDA Report GA-A13766, General Atomic, January 5, 1976.

9. REACTOR SYSTEMS ENGINEERING (189a No. SU019)

Under this task, reactor system development activities are being defined and carried out; analytical methods and models applicable to the assessment of thermal-hydraulic performance of the GCFR reactor core are being developed and utilized to define operating strategies; methods and materials behavior models are being evaluated to assess the capability of the PCRV internal structures to serve as a postaccident fuel containment (PAFC); and GCFR plant control systems are being developed, including establishment of the interface requirements between these control systems, the plant protection system, the operational protection system, and the plant operator.

9.1. CORE THERMAL-HYDRAULIC PERFORMANCE

Activities for this subtask are devoted to the development of accurate computer models for the evaluation of core thermal-hydraulic performance. In addition, the requirements for and methods of core temperature monitoring are being investigated.

During this quarter, the first draft of a core orificing report was prepared to satisfy an ERDA milestone, and some refinements were made to GACOOL. In the area of low-flow analyses, the magnitude of buoyancy forces has been calculated for specified inlet and outlet temperature conditions. Using simplified analyses, an expression has been derived for the frictional pressure losses resulting from the mass flow associated with the specified inlet and outlet coolant temperature conditions. Evaluation of alternate core temperature monitoring systems was also continued.

9.1.1. GACOOL Development

Development activity during this quarter was minimal. An additional general-purpose input subroutine which will give GACOOL multiple-case capabilities is being written, and an option which allows assembly and fuel rod power distribution data to be internally generated instead of using input power distribution data which has been generated by external computer programs has been added to GACOOL. The external computer program used to provide power distribution information to GACOOL has been updated, and it now has better models for treating the axial and radial blankets and can provide power distribution information for the whole core, the axial and radial blankets, and the active fuel region in a form which can be used by GACOOL in one computer run.

9.1.2. Preliminary Core Thermal Hydraulic Performance and Orificing Results

This section is concerned with the following core thermal-hydraulic performance studies: (1) nominal design point performance, (2) part-load power to flow, (3) core orificing, and (4) core parameters (Refs. 9-1 through 9-4). Performance studies are currently being done based on the latest available system and core design parameters to provide a consistent set of information for overall core thermal-hydraulic performance and orificing. These studies and all work done to date will be reported in an upcoming core orificing report. The major effort made during this quarter was the writing of a draft of this report and the performance of support analysis.

9.1.3. Low-Flow Analysis

After irradiation of core and blanket assemblies, there is a residual heat source in the fuel. This residual heat source arises from the decay of fission products and the transmutation of fertile materials. Although this heat source constitutes only a small fraction of the total, full operating power, provisions must be made for its removal by forced

circulation. The coolant flow rates required at these low power levels are low; consequently, the related core pressure drops are also low. These pressure differentials are so low that buoyancy forces arising from the reduced density of the heated coolant become significant. These buoyancy forces which oppose the normal downward flow of coolant in the core tend to reduce the flow in an assembly, increase the average coolant temperature, and thereby further increase the buoyant forces. In addition, helium exhibits an increasing viscosity as a function of temperature, which further contributes to the tendency for a reduction in downward coolant flow. In the extreme, buoyancy forces may lead to flow starvation and flow reversal in assemblies with high decay heat power levels and/or abnormally high flow resistances.

With a relatively low core heat capacity (in comparison with HTGR systems), flow starvation in a GCFR assembly would result in an adiabatic temperature rise of several degrees centigrade per second in the assembly, even at times long after shutdown. Therefore, although it is desirable from a systems point of view to keep the coolant mass flow at a minimum, there is also the requirement that down-flow be maintained in all assemblies and subchannels of the GCFR core at all times.

Ultimately, the goal of low-flow analyses is to specify the limiting conditions of operation to prevent the flow reversal phenomenon while simultaneously not allowing the cladding temperature limits to be exceeded. Based on the pressure differential across the core required to prevent flow reversal, the total core flow rate may be determined and the adequacy of circulator performance evaluated. To specify particular core flow rates and pressure differentials, however, would require detailed power distributions as a function of time after shutdown and hydraulic performance parameters at low Reynolds numbers for fuel, blanket, and control assemblies in the rod bundle, orifice, and inlet sections. These data will be generated in ongoing programs. The magnitudes of the buoyancy forces for various coolant inlet and outlet temperature conditions may be calculated independent of such information and are given in Table 9-1. These buoyancy forces

TABLE 9-1
MAGNITUDE OF BUOYANCY FORCES[a]

T_{in}	T_{out} 300°C (572°F)	400°C (752°F)	500°C (932°F)	600°C (1112°F)	700°C (1292°F)
100°C (212°F); P_{in} = 10.94 kg/m^3 (0.683 lbm/ft^3)	$\bar{T}$ = 200°C (392°F) $\bar{\rho}$ = 8.618 kg/m^3 (0.538 lbm/ft^3) $\bar{\mu}$ = 2.769 x 10^{-4} N-s/m^2 (0.067 lbm/ft-hr) BF = 44.5 Pa (0.00645 psi)	$\bar{T}$ = 250°C (482°F) $\bar{\rho}$ = 7.801 kg/m^3 (0.487 lbm/ft^3) $\bar{\mu}$ = 2.934 x 10^{-4} N-s/m^2 (0.071 lbm/ft-hr) BF = 57.9 Pa (0.0084 psi)	$\bar{T}$ = 300°C (572°F) $\bar{\rho}$ = 7.144 kg/m^3 (0.446 lbm/ft^3) $\bar{\mu}$ = 3.058 x 10^{-4} N-s/m^2 (0.074 lbm/ft-hr) BF = 68.4 Pa (0.00992 psi)	$\bar{T}$ = 350°C (662°F) $\bar{\rho}$ = 6.567 kg/m^3 (0.410 lbm/ft^3) $\bar{\mu}$ = 3.306 x 10^{-4} N-s/m^2 (0.080 lbm/ft-hr) BF = 77.2 Pa (0.0112 psi)	$\bar{T}$ = 400°C (752°F) $\bar{\rho}$ = 6.119 kg/m^3 (0.382 lbm/ft^3) $\bar{\mu}$ = 3.472 x 10^{-4} N-s/m^2 (0.084 lbm/ft-hr) BF = 84.8 Pa (0.0123 psi)
200°C (392°F); P_{in} = 8.618 kg/m^3 (0.538 lbm/ft^3)	$\bar{T}$ = 250°C (482°F) $\bar{\rho}$ = 7.081 kg/m^3 (0.487 lbm/ft^3) $\bar{\mu}$ = 2.934 x 10^{-4} N-s/m^2) (0.071 lbm/ft-hr) BF = 16.5 Pa (0.0024 psi)	$\bar{T}$ = 300°C (572°F) $\bar{\rho}$ = 7.144 kg/m^3 (0.446 lbm/ft^3) $\bar{\mu}$ = 3.058 x 10^{-4} N-s/m^2 (0.074 lbm/ft-hr) BF = 28.9 Pa (0.0042 psi)	$\bar{T}$ = 350°C (662°F) $\bar{\rho}$ = 6.567 kg/m^3 (0.410 lbm/ft^3) $\bar{\mu}$ = 3.306 x 10^{-4} N-s/m^2 (0.080 lbm/ft-hr) BF = 38.6 Pa (0.0056 psi)	$\bar{T}$ = 400°C (752°F) $\bar{\rho}$ = 6.119 kg/m^3 (0.382 lbm/ft^3) $\bar{\mu}$ = 3.472 x 10^{-4} N-s/m^2 (0.084 lbm/ft-hr) BF = 46.2 Pa (0.0067 psi)	$\bar{T}$ = 450°C (842°F) $\bar{\rho}$ = 5.686 kg/m^3 (0.355 lbm/ft^3) $\bar{\mu}$ = 3.678 x 10^{-4} N-s/m^2 (0.089 lbm/ft-hr) BF = 53.8 Pa (0.0078 psi)
350°C (572°F); P_{in} = 7.144 kg/m^3 (0.446 lbm/ft^3)	BF = 0 $T_{in} = T_{out}$	$\bar{T}$ = 350°C (662°F) $\bar{\rho}$ = 6.567 kg/m^3 (0.410 lbm/ft^3) $\bar{\mu}$ = 3.306 x 10^{-4} N-s/m^2 (0.080 lbm/ft-hr) BF = 11.7 Pa (0.0017 psi)	$\bar{T}$ = 400°C (752°F) $\bar{\rho}$ = 6.119 kg/m^3 (0.382 lbm/ft^3) $\bar{\mu}$ = 3.472 x 10^{-4} N-s/m^2 (0.084 lbm/ft-hr) BF = 20.7 Pa (0.0030 psi)	$\bar{T}$ = 450°C (842°F) $\bar{\rho}$ = 5.686 kg/m^3 (0.355 lbm/ft^3) $\bar{\mu}$ = 3.678 x 10^{-4} N-s/m^2 (0.089 lbm/ft-hr) BF = 28.2 Pa (0.0041 psi)	$\bar{T}$ = 500°C (932°F) $\bar{\rho}$ = 5.334 kg/m^3 (0.333 lbm/ft^3) $\bar{\mu}$ = 3.844 x 10^{-4} N-s/m^2 (0.093 lbm/ft-hr) BF = 35.2 Pa (0.0051 psi)
400°C (752°F); P_{in} = 6.119 kg/m^3 (0.382 lbm/ft^3)	$T_{in} > T_{out}$ undefined	BF = 0 $T_{in} = T_{out}$	$\bar{T}$ = 450°C (842°F) $\bar{\rho}$ = 5.686 kg/m^3 (0.355 lbm/ft^3) $\bar{\mu}$ = 3.678 x 10^{-4} N-s/m^2 (0.089 lbm/ft-hr) BF = 8.96 Pa (0.0013 psi)	$\bar{T}$ = 500°C (932°F) $\bar{\rho}$ = 5.334 kg/m^3 (0.333 lbm/ft^3) $\bar{\mu}$ = 3.844 x 10^{-4} N-s/m^2 (0.093 lbm/ft-hr) BF = 15.8 Pa (0.0023 psi)	$\bar{T}$ = 550°C (1022°F) $\bar{\rho}$ = 4.998 kg/m^3 (0.312 lbm/ft^3) $\bar{\mu}$ = 4.000 x 10^{-4} N-s/m^2 (0.097 lbm/ft-hr) BF = 22.7 Pa (0.0033 psi)
500°C (932°F); P_{in} = 5.334 kg/m^3 (0.333 lbm/ft^3)	$T_{in} > T_{out}$ undefined	$T_{in} > T_{out}$ undefined	BF = 0 $T_{in} = T_{out}$	$\bar{T}$ = 550°C (1022°F) $\bar{\rho}$ = 4.998 kg/m^3 (0.312 lbm/ft^3) $\bar{\mu}$ = 4.009 x 10^{-4} N-s/m^2 (0.097 lbm/ft-hr) BF = 6.20 Pa (0.0009 psi)	$\bar{T}$ = 600°C (1112°F) $\bar{\rho}$ = 4.725 kg/m^3 (0.295 lbm/ft^3) $\bar{\mu}$ = 4.175 x 10^{-4} N-s/m^2 (0.101 lbm/ft-hr) BF = 13.1 Pa (0.0019 psi)

[a] BF = buoyancy forces.

have been tabulated only for the fully pressurized system because buoyancy forces are proportional to system pressure, and the core pressure drop, to which the buoyancy forces are compared, is inversely proportional to the system average pressure. Therefore, the potential for flow reversal is only significant for the fully pressurized PCRV (Ref. 9-5). The buoyancy forces in Table 9-1 are the difference between the static head of a column of coolant at its inlet temperature and the static head of a column of coolant at the reduced average density associated with the temperature rise to various outlet temperatures. A linear coolant temperature rise through the active core region was assumed in these calculations.

The inlet and outlet coolant temperature conditions given in Table 9-1 uniquely define a mass flow rate for any given decay heat power level. For long irradiation times ($\sim 10^7$ s), the power level ratio, $P(t)/P_o$, t seconds after shutdown is given by a modified Way-Wigner formula (Ref. 9-6):

$$P(t)/P_o = (0.13)(t^{-0.2} - 0.0398) \quad .$$

Therefore, for given inlet and outlet temperature conditions, the mass flow rate and the related frictional pressure drop, which is dominant in the low flow regimes, exhibit the same time dependence. Utilizing the reference design parameters (Ref. 9-7) and a friction factor inversely related to Reynolds number, an expression for frictional losses as a function of time for specified inlet and outlet conditions was derived:

$$\Delta P_{friction} = \frac{K\bar{\mu}(t^{-0.2} - 0.0398)}{(T_{out} - T_{in})\bar{\rho}} \quad ,$$

where $K = 4.536 \times 10^9$,

$T = °C$,

$t =$ seconds,

$\bar{\rho} = kg/m^3$,

$\bar{\mu} = N\text{-}s/m^2$,

$\Delta P = Pa$.

Independent work has indicated the importance of consideration of the unique characteristics of atypical subchannels such as edge and corner channels. This formulation, however, is for average subchannels operating at the maximum decay power. For an inlet temperature of 200°C (392°F) and an exit temperature of 400°C (752°F), buoyancy forces equal one-third of the frictional pressure losses at 13.3 hr. These results suggest the rapidity with which buoyancy forces become significant after shutdown when flow rates are controlled on the basis of inlet and outlet coolant temperatures.

9.2. POSTACCIDENT FUEL CONTAINMENT

The activities under this subtask have been transferred to the Safety Program and are described in Section 12.4.

9.3. CONTROL SYSTEMS

Development of system component mathematical models is nearing completion, and work has begun on integrating these models into the system simulation. To establish how the component models are intended to mathematically interface with each other, the model solution diagram shown in Fig. 9-1 was generated. This diagram illustrates that a complete set of defining equations with a consistent causality can be developed. Each block in the diagram represents a physical component or group of components. The lines interconnecting the blocks show the flow of information from one component to the next and are not to be confused with the fluid flow direction in the process. The variables required as inputs for a given component model are represented by arrows pointing toward the block, and the variables computed by the component model are represented by arrows pointing away from the block. The fluid process variables pressure, enthalpy, and flow are used to mathematically interface the component models in the steam loop. In the primary loop, a characteristic helium pressure (loop pressure drop is considered small relative to loop average pressure), flow, and gas temperature are the component interface variables.

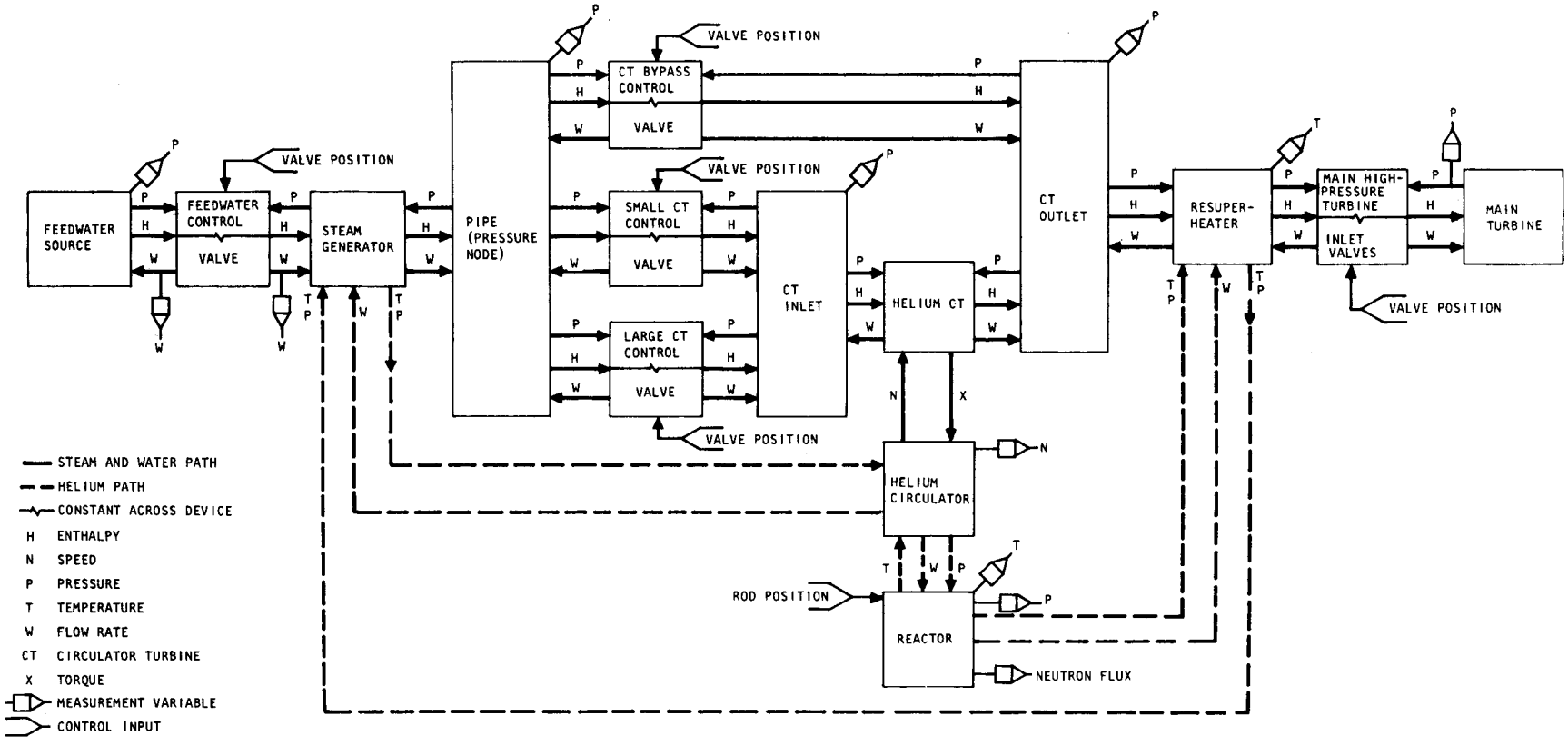

Fig. 9-1. Model solution diagram

The process variable measurements and control inputs which will be considered in the initial control system analyses are also indicated.

Initially, the steam loop will not be closed through the condenser, condensate pumps, feedwater heaters, and turbine-driven feedwater pumps. These BOP components will be added later when their requirements are better known and after the characteristics of the initial model are established and understood.

One of the uses of this simulation will be to investigate numerous different plant configurations and/or control strategies. The modular construction of the simulation based on hardware components permits relatively easy modification of the plant configuration. In keeping with this need for versatility, a circulator turbine bypass control valve has been added to the steam loop although it is not part of the present GCFR configuration. A preliminary control system development plan has been generated and will be submitted for review and comment in the near future.

9.4. ALTERNATE CORE TEMPERATURE MEASUREMENT

The possibility of measuring the average coolant temperature from each core assembly by infrared imaging has been investigated. The initial phase of this study was restricted to considerations of the feasibility of two concepts. The reference design concept consists basically of a system of two concave mirrors inside the PCRV for viewing the full reactor core. A detector outside the PCRV scans the core image and relays the spectral irradiance signals to a minicomputer or the plant data acquisition and processing system. The latter converts the signals to obtain the average coolant temperature at the outlet of each fuel assembly. The backup concept consists of a servomechanism-controlled plane objective mirror which sequentially scans the core. The reflected image is then picked up by a concave mirror, reduced in size, and viewed by the detector.

Two basic criteria were identified to determine the feasibility and compare the merit of the two concepts: the system signal-to-noise ratio

and the resolution, which may be interpreted as the number of resolvable temperature points per fuel assembly. Comparison of the two concepts indicates the following:

1. The signal-to-noise ratio for the reference design concept is adequate within the range of temperatures of interest. The resolution is poor and is expected to diminish owing to mirror aberration. A study of aberration for both concepts was started but has not been completed.

2. The signal-to-noise ratio and the resolution of the system for the backup concept are more than adequate; the resolution will be confirmed after the mirror aberration study is completed.

The above conclusions are based on initial concepts, with a minimal effort toward optimization. Additional work to increase the optical aperture of the reference design system and the reliance on computation and pattern recognition techniques rather than precise positioning of the scanning mirror in the backup concept may result in significant improvements.

REFERENCES

9-1. "Gas-Cooled Fast Breeder Reactor Quarterly Progress Report for the Period May 1, 1975 Through July 31, 1975," ERDA Report GA-A13565, General Atomic, October 2, 1975.

9-2. "Gas-Cooled Fast Breeder Reactor Quarterly Progress Report for the Period August 1, 1975 Through October 31, 1975," ERDA Report GA-A13766, General Atomic, January 5, 1976.

9-3. "Gas-Cooled Fast Breeder Reactor Quarterly Progress Report for the Period February 1, 1976 Through April 30, 1976," ERDA Report GA-A13868, General Atomic, May 31, 1976.

9-4. "Gas-Cooled Fast Breeder Reactor Quarterly Progress Report for the Period May 1, 1976 Through July 31, 1976," ERDA Report GA-A13975, General Atomic, August 31, 1976.

9-5. Joksimovic, V., et al., "An Analysis of HTGR Core Cooling Capability," Gulf General Atomic Report Gulf-GA-A12504, March 30, 1973.

9-6. Yevick, J. G., ed., Fast Reactor Technology: Plant Design, MIT Press, Cambridge, 1966.

9-7. "300-MW(e) Gas-Cooled Fast Breeder Reactor Demonstration Plant," General Atomic Report GA-A13045, July 15, 1974.

10. COMPONENT DEVELOPMENT (189a No. SU025)

10.1. REACTOR VESSEL

The scope of this subtask is to assure that the design of the PCRV and related components which contribute to the integrity of the pressure boundary is satisfactory and to test critical component configurations to make certain that they attain the design objectives. This subtask will demonstrate by analyses and tests that the PCRV and its penetrations and closures meet the design criteria. It will also provide assurance that (1) the design of the thermal barrier satisfactorily protects the liner and PCRV from the effects of high temperatures and (2) the flow restrictors for the large penetrations can be developed to limit the flow of helium from the primary coolant systems to acceptable levels in the event of structural failure of a penetration or closure component.

Work accomplished during the previous quarter included preparation of a prototype configuration of the reactor cavity closure. Computer analysis showed that the stress levels were within the allowable limits of the ASME Pressure Vessel Code, Section III, except in the regions of the perforations. To overcome this, shear webs were added to the design, and this configuration was sent to ORNL for preparation of a 1/15-scale test model. Layout drawings were prepared for the PCRV configurations for the low-pressure-drop loops. One configuration has the helium circulator and steam generator in the same cavity, and the other has these components in separate cavities. The structural adequacy of the reference design PCRV is being confirmed by a three-dimensional finite-element computer code. The stress levels for the initial prestress condition and the prestress condition with the maximum cavity pressure were determined and found to be satisfactory. The highest stress zone was in the area of the fuel handling penetrations in the bottom head. A stress relief sleeve proposed for the central penetration would reduce the magnitude of the stresses to acceptable levels.

During this quarter, drafting efforts are continuing on the layout of the alternate PCRV configurations for the updated nuclear steam supply system (NSSS) with the low pressure drop for the primary coolant loops. The two candidate configurations are being revised to incorporate the low-pressure-drop fuel assemblies, which have an increased pitch and length [pitch = 196.5 mm (7.74 in.), length = 3665.0 mm (144.3 in.)]. The first configuration, which has the helium circulator and the steam generator in the same cavity, was preliminarily sized for the vertical cross section by calculating the concrete ligament between the reactor core cavity and the steam generator cavity and the ligament between the steam generator cavity and the wire-winding channels. Layouts of the upper and lower faces of the PCRV have established that there is sufficient space for installing the large-capacity tendons required for each of the cavities and ducting. This first configuration had a total of six cavities radially spaced around the central cavity: three steam generator cavities and three auxiliary circulator cavities. This design resulted in adequate concrete ligaments in the circumferential direction between the steam generator cavities and the auxiliary circulator cavities. In the case of the second PCRV configuration, which has the steam generators and the helium circulators in separate cavities, there are three steam generator cavities, three helium circulator cavities, and three auxiliary circulator cavities, making a total of nine radial cavities around the central cavities. Provision of sufficient concrete for the circumferential ligaments betewen the nine radial cavities will dictate the size of the second configuration. Layout studies are being conducted for locating the cavities and determining the size of the PCRV for placement of the tendons. Structural analyses performed with the three-dimensional finite-element computer code for the thermal conditions for the GCFR PCRV have established that the peripheral tendons are not required; therefore, the layout drawing for the two alternate configurations are being prepared without space requirements for the peripheral tendons. The three-dimensional computer analysis performed for the reference design PCRV has established that the configuration is structurally adequate for the elastic conditions of one maximum cavity pressure (MCP).

In connection with the PCRV closure tests being conducted by ORNL, coordination discussions were held pertaining to the materials and material specifications for the prototype configuration of the reactor cavity closure, shown in Fig. 10-1 of Ref. 10-1. ORNL responded with material specifications for the 1/15-scale model. These materials are being reviewed to determine if their physical properties compare satisfactorily with those specified for the prototype. ORNL will proceed with acquisition of the materials and performance of material qualification testing. The tubing to be used in the model will be checked by nondestructive methods utilizing eddy current, dye penetrant, and ultrasonic vibration. Consultations of the engineering staff and the management of the ORNL machine shops have established that the fabrication of the scale model is feasible and the model can be completed by the date of the start of the scheduled test. ORNL has made arrangements with Midwest Technical, Incorporated., for detailing the 1/15-scale central closure model. The fixture for the 1/15-scale model test was successfully pressurized to ∿193 MPa (∿28,000 psi) and had no leakage at the seals. However, the pressure galled the threads of the fixture closure plug within the pressure chamber. This plug has been removed for remachining of the threads. Members of ORNL and GCFR have discussed plans for the testing requirements for the test fixture to be used in the 1/4-scale models of the GCFR closures.

10.2. CONTROL AND LOCKING MECHANISMS

The scope of this task covers the preparation of a development plan for the core assembly control and locking mechanisms for the 300-MW(e) GCFR demonstration plant.

During this quarter, alternate approaches were generated to the system described in the preliminary draft of the development plan (Ref. 10-1). Consequently, this effort will be pursued until a decision can be made regarding which alternative is the most technically and economically practicable.

10.3. FUEL HANDLING DEVELOPMENT

10.3.1. Conceptual Studies and System Optimization

The primary effort during this quarter was the completion of the milestone summary report draft for this subtask. The study effort concentrated on evaluations of various refueling system design concepts, with the goal of attaining an optimum system concept. A secondary effort summarized in the report was the initiation of component conceptual design studies of the in-vessel fuel handling machines.

Alternative system concepts were compared with criteria established during the evaluation phase, and a refueling system concept which will be the basis for continued component conceptual design, follow-on preliminary design, and subsequent detail design was recommended. This concept can be referred to as the baseline design concept. The factors which make up the trade-off comparison criteria fall into three basic categories according to priority:

1. Safety improvement.
2. Expeditious operation.
3. Cost impact (economic).

These basic criteria were considered when reviewing potential system concept improvements. However, for the present and contemplated demonstration plant design, there were several specific criteria or requirements developed which are of prime importance to this subtask:

1. Minimum or no impact on PCRV design.

2. Minimization of impact on containment building design, especially base mat depth.

3. Minimization or elimination of the need to leave fuel handling equipment inside the containment building during power reactor operations.

4. Minimization of large and heavy shielded equipment items which must be moved into position under the PCRV.

The rationale for these requirements is very basic when considering interfaces with the demonstration plant. It is desirable to keep the refueling system equipment in an accessible location when it is not in use in order that there be minimum impact on the rest of the plant and availability of equipment to enable functional checkout and/or operator training. Unless a radical change or revision is made to the PCRV, the reactor containment building, or the core arrangement within the reactor, the refueling system design concept will not be significantly affected by changes to the remainder of the plant.

During this quarter, concept studies were initiated on the fuel lifting machine (FLM) and the plenum service machine (PSM); the PSM was previously known as the fuel service machine (FSM). In addition, studies on the fuel transfer machine (FTM) continued. An FLM concept is being developed which utilizes a telescoping carriage containing a moving grapple; this is similar to the FTM lifting mechanism. The FTM study efforts are summarized in Ref. 10-1.

A potential shielding problem was identified during the FLM study. As the spent fuel assembly is lowered through the PCRV lower head in the region close to the isolation valve, additional shielding may be required. Two alternatives have been suggested:

1. Addition of a shielding sleeve as part of the FLM or a removable sleeve provided as an extension to the fuel transfer cask (FTC).

2. Permanent shielding sleeve or cylinder built around the penetration and buried in the concrete and/or attached to the bottom face of the PCRV.

Both alternatives require further investigation after more definitive radiation analysis and shielding requirements are received from the Analysis and Safety Department.

The PSM functional requirements may be classified into two broad groups: (1) servicing functions related to the entire refueling plenum space; (2) lifting of a fuel assembly from the bottom of the plenum. Certain facts were uncovered during the initial studies:

1. Lifting of a fuel assembly requires a large manipulator capable of handling weights up to 400 kg (900 lb).

2. Servicing of the entire plenum volume involves a complex telescoping or collapsible mechanism.

3. A mechanism which can reach every point of the plenum with the large manipulator may be quite bulky and not easily packaged into the available equipment space.

During FY-77, continued conceptual studies will be carried out on a broader basis to consider and evaluate different service machine mechanism concepts. The subtask summary report (Ref. 10-2) discusses the methods utilized, the alternate concepts considered, and the recommended baseline refueling system design concept.

10.3.2. Postirradiation Examination Facility Evaluations

During this quarter, an initial draft of the subtask milestone report was prepared. This draft was based on the amount of criteria data received and the available information on similar postirradiation examination facilities. The draft was implemented into an evaluation report and issued

internally (Ref. 10-3). Certain inspection parameters were verified, and a preliminary list of the items to be inspected together with some of the inspection equipment which may be utilized is identified in the report.

Visual inspection and nondestructive examination (NDE) of certain selected spent fuel assemblies will be carried out under water in an extension to the spent fuel storage pool. Dimensional gauging equipment will be utilized for external measurements of an intact assembly, and the flow duct will be cut or disassembled to enable removal of the intact internal components. Visual inspection will be enhanced by use of underwater television cameras, a periscope, and a borescope where appropriate. Nondestructive examination techniques and equipment (e.g., neutron radiography, ultrasonics, pulsed eddy current measurements, etc.) will require further investigation and development when a final fuel assembly design is approved. Further study and concept investigation is recommended after BOP facility arrangements are firm and fuel assembly design is fixed. Additional input is required from the safety and nuclear analysis groups. A cost impact study on related operations should be included in this investigation.

10.3.3. Spent Fuel Shipping Studies

This effort consisted primarily of a literature search and a review of the applicable data. Data from vendors of shipping casks and related equipment were incorporated into the subtask milestone preliminary report (Ref. 10-4).

The primary areas of concern include those associated with shielding and cooling requirements during shipping. A survey was made of existing and planned shipping casks to help ascertain if some of these designs comply with GCFR requirements. The transportation and handling of spent fuel receives much attention during an international symposium held every three years.* Most of the data which have been collected are from papers presented at

*The International Symposium on Packaging and Transportation of Radioactive Materials.

these symposia. A brief review and evaluation of existing casks and preliminary GCFR data indicates that it is feasible to ship a limited number of GCFR spent fuel assemblies in an existing cask designed primarily for LWR fuel (e.g., six GCFR fuel assemblies in a modified General Electric IF-300 cask shipped by rail). The preliminary report (Ref. 10-4) presents some of the data available on casks and equipment, and based on these related data, GCFR spent fuel shipping requirements will be quite similar to those for LWR spent fuel.

Areas which require further in-depth investigation, including determining the maximum quantity of fuel assemblies to be shipped in each cask, the cooling medium (wet or dry), and the governmental restrictions and requirements regarding transportation by rail and/or highway. These items should be considered after the more critical GCFR components have been developed and the fuel assembly design and associated decay heat parameters are more fully defined.

10.4. CORE SUPPORT STRUCTURE

The purpose of this subtask is to assure the availability of the structural analysis methods and materials mechanical behavior required to assess the structural integrity of the GCFR core support structure under all anticipated operational and safety-related loading conditions in the GCFR environment.

A number of tasks were performed during this quarter, and the draft on the GCFR core support structure static test report was completed.

A meeting was held with ERDA on the Clinch River Breeder Reactor (CRBR) core support design at the CRBR project office in Oak Ridge. The purpose of the meeting was to gather information on CRBR core support design and fabrication and the effect of irradiation on stainless steel. It was concluded that the design of the GCFR core support grid plate is not different in concept from that of the CRBR core support grid plate. The CRBR grid plate is designed for a greater pressure drop [1.379 MPa versus

151.68 kPa (∿200 versus ∿22 psi)] than the GCFR grid plate, and it has a greater ligament efficiency, which is achieved by a modular inlet nozzle which penetrates the grid plate and acts as a manifold to supply coolant to seven reactor fuel assemblies.

10.4.1. Structural Analysis

10.4.1.1. Clamping Effect in the Edge of the Grid Plate Test Model.

Because the grid plate test model is clamped against the applied pressure loading between two steel rings by eight preloaded bolts, the boundary condition of the grid plate is not a simply supported case. Determination of the effect of clamping is necessary for comparing the results of testing with numerical and analytical methods. The test setup is shown in Fig. 10-1. The free-body diagram of the grid plate and the support rings is shown in Fig. 10-2, where V and Q are the edge forces exerted at the corner edges of the support ring when the grid plate is subjected to a pressure loading. The rotation at the edge of the grid plate can be shown as

$$\theta = \frac{3(1 - \nu^*)pR^3}{2E^*H^3} - \frac{12(1 - \nu^*)R}{E^*H^3}(QH + tV) \quad . \tag{10-1}$$

The lower support ring can be treated as a short cylinder* which is subjected to an edge force Q at the upper end and free at the lower end (Fig. 10-3). From Ref. 10-5, the exact formulas for a short cylinder shell with uniform wall thickness subjected to an edge force is

$$u_r = -\frac{Q}{2Dk^3}\left[\frac{F_4}{F_1}F_7(\xi) - \frac{F_5}{F_1}F_{15}(\xi) - \frac{F_6}{F_1}F_{16}(\xi)\right] \quad , \tag{10-2}$$

where $k = \frac{\sqrt[4]{3(1 - \nu^2)}}{\sqrt{Rt}}$,

$\xi = \frac{x}{l}$.

*For a cylinder with $L < 3.1\sqrt{Rt}$.

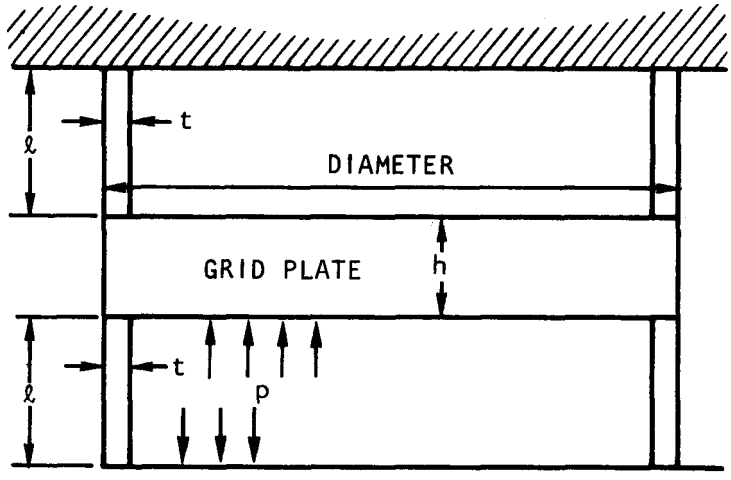

Fig. 10-1. Test setup

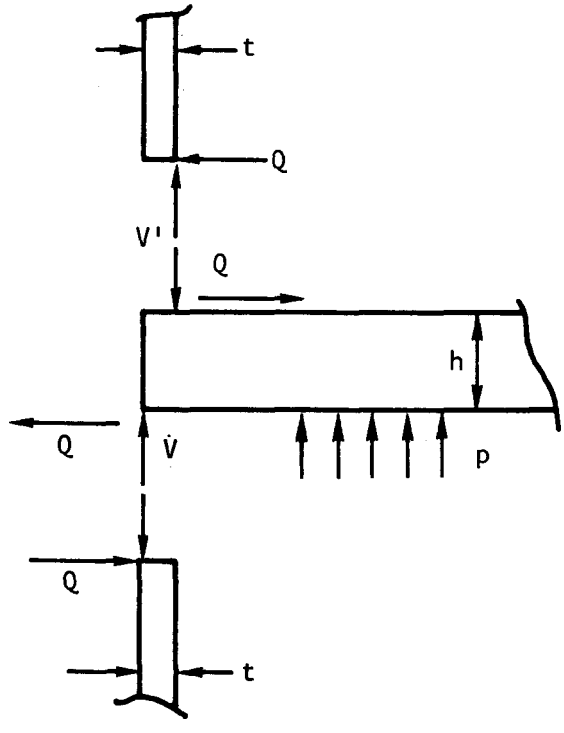

Fig. 10-2. Free-body diagram of grid plate and support rings

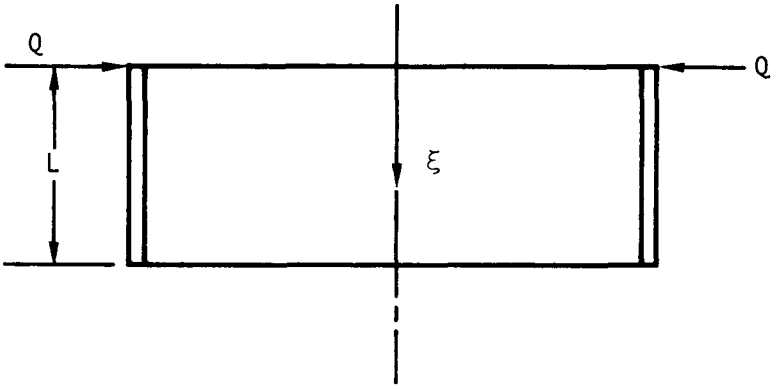

Fig. 10-3. Edge forces acting on short cylinder

The factors F_i are defined as follows:

$$\left.\begin{aligned} F_1 &= \sinh^2 kl - \sin^2 kl \quad , \\ F_4 &= \sinh kl \cosh kl - \sin kl \cos kl \quad , \\ F_5 &= \sin^2 kl \quad , \\ F_6 &= \sinh^2 kl \quad , \\ F_7(\xi) &= \cosh kl\xi \cos kl\xi \quad , \\ F_{15}(\xi) &= \cosh kl\xi \sin kl\xi \quad , \\ F_{16}(\xi) &= \sinh kl\xi \cos kl\xi \quad . \end{aligned}\right\} \qquad (10\text{-}3)$$

For the lower support cylinder, the radial deflection at the point of loading can be calculated as follows:

$$l = 63.5 \text{ mm } (2.5 \text{ in.}) \quad ,$$

$$E = 2.0684 \times 10^6 \text{ MPa } (30 \times 10^7 \text{ psi}) \quad ,$$

$$R = 241.3 \text{ mm } (9.5 \text{ in.}) \quad ,$$

$$\nu = 0.3 \quad ,$$

$$t = 9.525 \text{ mm } (0.375 \text{ in.}) \quad ,$$

$$D = \frac{Et^3}{12(1 - \nu^2)} = 0.1448 \times 10^6 \quad ,$$

$$F_1 = 7.0369 - 0.9828 = 6.0541 \quad ,$$

$$F_4 = (2.6527)(2.8349) - (0.9913)(-0.1313) = 7.6512 \quad ,$$

$$F_5 = 0.9828 \quad ,$$

$$F_6 = 7.0369 \quad ,$$

$$F_7(\xi)_{\xi=0} = 1 \quad ,$$

$$F_{15}(\xi)_{\xi=0} = 0 \quad ,$$

$$F_{16}(\xi)_{\xi=0} = 0 \quad .$$

Substituting these factors and parameters into Eq. 10-2, the expression for the radial deflection can be reduced:

$$u_r = \frac{Q}{0.63160}\left(\frac{7.6512}{6.0541}\right) \cong \frac{2Q}{D} \quad . \tag{10-4}$$

When the test grid plate is deflected by the pressure loading, the support rings will be also deformed. As shown in Fig. 10-4, the line $\overline{a\ b}$ rotates as the grid plate and support rings deform. After the grid plate and support rings deform, the radial deflection of the ring can be written as

$$u_r = \overline{a\ a'} = \overline{b\ b'} = (\overline{bc})\ \theta \quad .$$

Since

$$\overline{bc} = 1/2(h^2 + t^2)^{1/2} \quad ,$$

then by using Eqs. 10-1 through 10-3 and the relation of compatibility between the support ring and the grid plate, the following relations can be derived: since

$$\theta = \frac{w}{\overline{bc}} \quad ,$$

then

$$\left.\begin{aligned} &\frac{2}{\sqrt{h^2 + t^2}}\left(\frac{2Q}{D}\right) = \frac{3(1 - \nu^*)pR^3}{2E^*h^3} - \frac{12(1 - \nu^*)R}{E^*h^3}(Qh + tV) \\ &\text{or} \\ &Q\left[\frac{2}{D\sqrt{h^2 + t^2}} + \frac{12(1 - \nu^*)Rh}{E^*h^3}\right] = \frac{3(1 - \nu^*)pR^3}{2E^*h^3} - \frac{12(1 - \nu^*)RtV}{E^*h^3} \quad , \end{aligned}\right\} \tag{10-5}$$

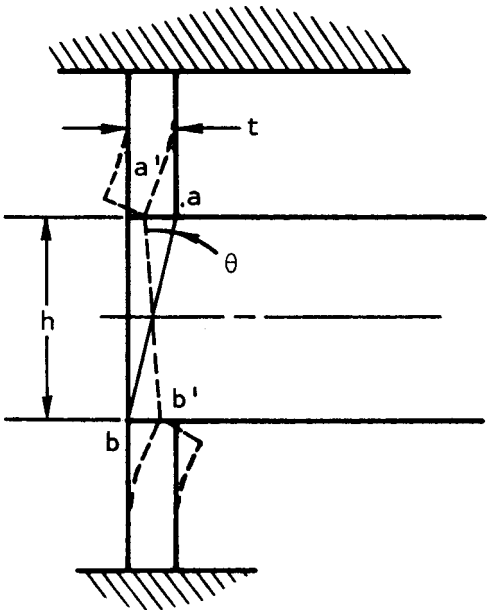

Fig. 10-4. Relationship of grid plate and support ring after deformation

where $E^* = 1.3789 \times 10^3$ MPa (0.2×10^6 psi),

$\nu^* = 0.76$,

$p = 413.68$ kPa (60 psi).

The other constants were defined previously.

Substituting the numerical values of all the constants into Eq. 10-5 yields

$$Q(3.816 + 10.5555) \times 10^{-6} = (33.0777p - 1.0995V) \times 10^{-6} \quad , \qquad (10\text{-}6)$$

where

$$V = [P - \pi(9.625)^2 p]/(2\pi)(9.625) = 0.0165P - 4.8125p \quad .$$

The eight bolts connecting the upper ring to the base plate were torqued to 67.791 Nm (50 ft-lb) each. Therefore, the total torque applied to the bolts was

$$67.791 \text{ Nm} \times 8 = 542.3 \text{ Nm (4800 in.-lb)} \quad .$$

According to Stewart's estimate (Ref. 10-6), the preload P can be shown as

$$T = 0.2P \times \text{diameter of the bolt} \quad ,$$

and the total preload of the bolts is

$$P = \frac{4{,}800 \times 2}{0.2} = 2.1351 \times 10^5 \text{N (48,000 lb)}$$

Thus, the right-hand side of Eq. 10-6 becomes

$$33.0777 \times 10^{-6} p - 1.0995 \times 10^{-6} (0.0165P - 4.8125p) \quad ,$$

where $p = 413.68$ kPa (60 psi) and $P = 2.1351 \times 10^5$N (48,000 lb).

The right-hand side of Eq. 10-6 then yields

$$1748.82 \times 10^{-6} \quad .$$

The force Q can be found as follows:

$$Q = \frac{1748.82 \times 10^{-6}}{14.3716 \times 10^{-6}} = 13.749 \text{ Nm } (121.69 \text{ in.-lb}) \quad .$$

10.4.1.2. Clamping Effect on the Center Deflection of the Grid Plate. If w_1 is the axial deflection at the center of the grid plate due to pressure loading p, and w_2 is the reduction of axial deflection at the center of the grid plate due to clamping effect, then w_1 and w_2 can be written as

$$w_1 = \frac{p}{64D^*} \frac{5 + \nu^*}{1 + \nu^*} R^4 \quad ,$$

$$w_2 = \frac{6(1 - \nu^*)R^2}{E^*h^3} (Qh + tV)$$

$$= \frac{R^2}{2D^*(1 + \nu^*)} [(121.69 \times 3.6) + (0.375)(0.0165 \times 48{,}000 - 4.8125 \times 60)]$$

$$= \frac{R^2}{2D^*(1 + \nu^*)} (249.36) \quad ,$$

$$\frac{w_2}{w_1} = \frac{249.36 \times \frac{R^2}{2D^*(1 + \nu^*)}}{\frac{p}{64D^*} \frac{(5 + \nu^*)}{(1 + \nu^*)} R^4}$$

$$= \frac{249.36 \times 32}{p(5 + \nu^*)(9.5)^2} = 0.2558 \quad .$$

The clamping effect reduces the center deflection of the grid plate by 25.58%.

10.4.1.3. Effective Young's Modulus. Correlation of the grid plate displacements under the pressure loadings of the experimental, analytical, and finite-element models has been completed using the experimentally determined effective moduli of elasticity of the grid plate, and it was found that agreement is excellent. The displacement difference among the three models ranges from 3% at the center of the grid plate to 10% 152.4 mm (6 in.) from the center. It is concluded that the effective elastic constants provided by the ASME Code for perforated plates are very conservative, and the effective Young's modulus E* of the test grid plate should be 2.7027×10^3 MPa (0.392×10^6 psi) instead of the ASME Code value of 1.3789×10^3 MPa (0.2×10^6 psi). Through this detailed comparison and correlation study of the experimental, analytical, and finite-element models, the response and structural integrity of the grid plate can be more confidently assured.

10.4.2. Core Support Structure Dynamic Model Test

Free vibration and simplified seismic excitation tests of a 15%-scale grid plate and core model containing 267 core assembly simulators were completed, and the results are reported in Ref. 10-7. The test and test setup are described in Ref. 10-1.

First, the perforated plate and simulated core assemblies were separately tested to determine their individual dynamic behavior. The grid plate was subjected to a free vibration test using an acoustic generator as the excitation source. This test determined that the two lowest frequencies of the perforated plate were 1498 and 4441 cps; the normalized mode shapes are shown in Fig. 10-5.

The core assembly simulators were individually installed in a rigid steel block simulating the assembly to grid plate connection and were "plucked" to determine the lowest natural frequency and damping factor. The natural frequency of the blanket assembly was 38.5 cps and that of the fuel assembly was 54 cps. These values represent the approximate scale

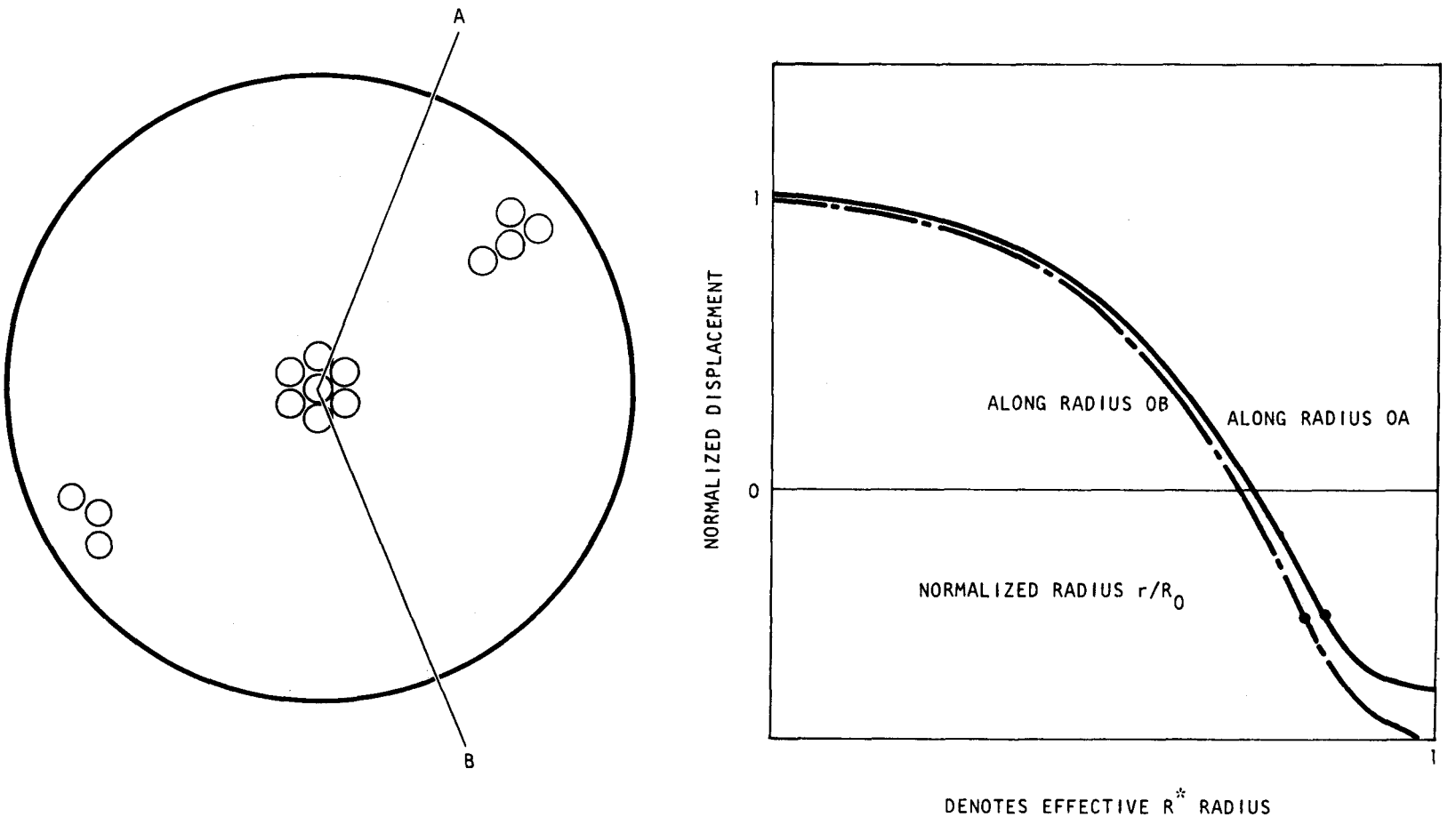

Fig. 10-5. Normalized grid plate free-vibration displacements

frequencies of the actual blanket and fuel assemblies, whose dynamic properties (principally their masses) are different. The damping factors of the simulated blanket and fuel assemblies were determined to be 0.6% and 0.3%. The damping values of the actual core assemblies are expected to be in the range of 5% to 10%. In forthcoming tests, the core assembly simulator damping characteristics will be modified to simulate this expected range.

After completion of individual component tests, the core assemblies were fixed into the grid plate, and the grid plate was mounted on top of a thin-wall cylindrical shell. The dynamic excitation of this structure was performed by a mechanical shaker in the plane of the grid plate and in some cases in the vertical direction of the grid plate. Harmonic excitation was applied to determine the resonant frequencies and the general mode shape patterns of the assembly. The dynamic response of the assembly was measured by accelerometers, and the mode shapes and relative displacements between adjacent core assemblies were determined by accelerometers and a relative displacement transducer. The general patterns of the system mode shapes were recorded by a high-speed camera, and the measured resonant frequencies due to horizontal excitation were 21, 41, 48, and 50 Hz. High-speed motion pictures illustrate that at frequencies of 21 and 48 Hz, the core assemblies move in phase in the direction of excitation and at 41 Hz, the blanket assemblies are predominantly excited and move in phase in the direction of excitation. The observed resonant frequencies due to vertical excitation were 23, 30, and 34 Hz.

The tests show the existence of system resonant frequencies which are approximately half the frequencies of the single core assemblies. This low system frequency is caused by dynamic coupling between the grid plate and the core assemblies. Although this phenomenon cannot be explained with a simple spring-mass beam model, the analysis method employed in Ref. 10-8 takes into account the elastic coupling effect between the plate and the core elements and predicts this frequency shift.

For random excitation, a simplified version of the El Centro earthquake frequency spectrum modified to account for scaling effects was applied in the horizontal direction, and predominant core motions were observed at frequencies of 21, 41, and 48 Hz.

The objectives of this seismic test program are to observe and study the basic physical phenomena of core structural dynamics and to use the test results for verification of the core seismic computer model. These tests have primarily been exploratory in nature, and further testing is planned to determine the nature of core motion during more representative seismic excitation. So far, the conclusive result of the tests is that the experiment indicates a low system resonant frequency. A detailed report of the test results and a comparison of them with computer and analytical results is in preparation and will be published at a later date. A follow-on test is being planned to study the effect of variation of damping and interassembly clearances. This test will use a more representative seismic excitation. In conjunction with the proposed flow test for the upper axial shield assembly, flow parameters were calculated for the flow past the core assembly support tubes. These flow parameters will be used in the evaluation of potential flow-induced vibration problems of the core assembly support tubes.

10.5. REACTOR SHIELDING ASSEMBLIES

The purpose of this task is to develop analytical methods and experimental programs to evaluate the reference design of the reactor shields. This evaluation considers heating and cooling of the shields, materials evaluation, seismic effects, need for flow tests, structural analysis, and alternate shield configurations necessary for developing a satisfactory design.

During this quarter, an intermediate report (Ref. 10-9) was written on the analytical methods used for the shield assembly. This report covers the structural, heat transfer, and hydrodynamic methods for

shield analysis, the results of the shield heat transfer and hydrodynamic analysis, and a shield flow test.

10.6. MAIN HELIUM CIRCULATOR, VALVE AND SERVICE SYSTEM

The objectives of this task are (1) to evaluate alternate main loop isolation valve conceptual designs; (2) to develop components for the main helium circulator valve and service system; and (3) to demonstrate the performance and reliability of the system by testing under anticipated operating conditions.

The basic function of the main loop isolation valve is to limit the reverse flow of primary coolant through a shut-down circulator. The performance requirements of the valve demand that the valve perform reliably under normal, upset, emergency, and faulted conditions. A draft copy of the topical report for the GCFR main loop isolation valve has been completed. This report includes a technical evaluation of the reference design and other alternative valve design concepts based on the reference design circulator configurations. Other valve designs applicable to the reverse flow and separate circulator cavity configurations will be included in the final topical report scheduled for issue in December 1976.

10.7. STEAM GENERATOR

The purpose of this task is to develop a steam generator which meets the operational, performance, and safety requirements of the GCFR. During FY-76, several steam generator designs were analyzed and evaluated and the merits of each design compared.

A first draft of a topical report (Ref. 10-10) which evaluates steam generator designs for the 300-MW(e) GCFR was completed and is being reviewed. The conclusions reached in the report are as follows:

1. The helical coil steam generator is recommended over the straight tube steam generator because of its wide variation in bundle

length (for a range of reasonable bundle diameters) and the resulting flexibility in the arrangement of the helium circulator and ducting.

2. Substitution of 2-1/4 Cr - 1 Mo steel for Incoloy alloy 800 H reference tubing material would be advantageous. However, this substitution cannot be made until the safety-related tritium permeability of 2-1/4 Cr - 1 Mo steel is determined for GCFR service conditions.

3. The critical heat flux behavior of a coiled tube differs considerably from that of a straight tube. Whereas critical heat flux occurs in one location in a straight-tube evaporator, it can occur over a considerable length and in different peripheral locations in the evaporator section of a helical coil. This nonuniform critical heat flux behavior produces an asymmetrical temperature distribution on the tube periphery, which should be experimentally and analytically evaluated for its effect on tube thermal stress, corrosion characteristics, and tube life.

4. An experimental/analytical program is required to establish the low-flow boiling stability characteristics of a GCFR-type steam generator coil. As part of the safe shutdown procedure for a GCFR, the steam generator must operate stably and produce high-quality steam at flow rates as low as 2% of design flow rate. Experimental evidence, at least for vertical straight-tube steam generators, demonstrates that such operation is readily attainable. However, the nonuniform critical heat flux behavior of coiled tubes combined with the fact that the GCFR steam generator coiled tube is nearly horizontal can result in low-flow boiling characteristics which substantially differ from those observed for straight vertical tubes.

The French Commissariat à L'Energie Atomique (CEA) Zebulon or Carmen-2 test loop was considered for performing GCFR low-flow boiling

stability tests. The various aspects of the test (development schedule, type of test section, instrumentation, etc.) are discussed in Ref. 10-11.

10.8. AUXILIARY CIRCULATOR, VALVE AND SERVICE SYSTEM

The general objectives of this task are (1) to prepare and issue a core auxiliary cooling system (CACS) component development plan document, (2) to develop components for the CACS which meet reliability and safety criteria, and (3) to demonstrate the performance and reliability of critical components by testing under anticipated operating conditions.

The development plan has been completed and is being reviewed. It includes all work activities, regardless of their funding sources, i.e., government, private, utility program, or international funding. Scheduling of the development program has also been integrated into an overall reference schedule showing the GCFR program milestone interfacing requirements.

The general approach to the CACS program is as follows:

1. Preparation of a CACS design criteria document which will establish the operational performance and safety and reliability requirements of the 300-MW(e) CACS demonstration plant (this document has been developed by GA under private funding).

2. Preparation of a CACS analysis which will cover system evaluation, trade-off, and design optimization studies. This analysis will include the auxiliary circulator motor drive and control system, core auxiliary heat exchanger (CAHE), core auxiliary cooling water system (CACWS), and residual heat removal system which interfaces with the NSSS and BOP equipment.

3. Development of CACS component design criteria. This work is being carried out under private funding.

4. Provision of design and performance analysis of components which meet CACS design criteria.

5. Verification of selected critical CACS component designs by extensive development tests, leading to a qualification test for the first-of-a-kind CACS circulator system.

6. Provision of in-service operation, evaluation, and operational qualification of the CACS for the demonstration plant.

The present CACS component development plan covers only item 5 work. The scope includes the auxiliary circulator, electric drive motor, variable-frequency control system, CAHE, and auxiliary loop isolation valve.

REFERENCES

10-1. "Gas-Cooled Fast Breeder Reactor Quarterly Progress Report for the Period May 1, 1976 Through July 31, 1976," ERDA Report GA-A13975, General Atomic, August 31, 1976.

10-2. DeLillo, R. L., "Summary Report of Refueling System Conceptual Studies and System Optimization," General Atomic, unpublished data.

10-3. DeLillo, R. L., "Postirradiation Examination (PIE) Facility Evaluation Report," General Atomic, unpublished data.

10-4. DeLillo, R. L., "Spent Fuel Shipping Study Preliminary Report," General Atomic, unpublished data.

10-5. Baker, E. H., L. Kovalevsky, and F. L. Rish, Structural Analysis of Shells, McGraw-Hill, New York, 1972.

10-6. ASME Handbook, McGraw-Hill, New York, 1953, pp. 171-177.

10-7. Bedore, R. L., "Static and Dynamic Test Results on a Gas Cooled Fast Breeder Reactor Scale Model," San Diego State University, July 14, 1976.

10-8. Penzes, L. E., "Seismic Model of the Core Support Structure for the Gas-Cooled Fast Breeder Reactor," ERDA Report GA-A13542, General Atomic, September 12, 1975.

10-9. Penzes, L. E., S. K. Bhat, and V. Jovanovic, "Mechanical Aspects of the Thermal Shielding for the Gas-Cooled Fast Breeder Reactor," ERDA Report GA-A14045, October 18, 1976.

10-10. Baroczy, C., "Evaluation of Steam Generator Designs for Application to the 300-MW(e) Gas-Cooled Fast Breeder Reactor," General Atomic, to be published.

10-11. Baroczy, C., "Considerations Affecting the Possible Use of the Zebulon and Carmen-2 Loops for GCFR Low Flow Boiling Stability Tests," General Atomic, unpublished data.

11. HELIUM CIRCULATOR TEST FACILITY (189a No. SU046)

The objective of this task is to develop a test facility for qualification testing of the GCFR main helium circulator. The scope of this task involves (1) evaluation of alternative test facility concepts in terms of technical feasibility and cost, (2) identification of the most promising test facility concept, (3) an architect/engineer preliminary design study, and (4) final design, construction, and checkout of the facility.

During the previous quarter, the full-power scoping study report and the Rocketdyne feasibility study were completed and reviewed (Refs. 11-1 and 11-2), and draft copies were sent to ERDA in accordance with the agreements made at the May 20-21, 1976 ERDA/GA meeting in San Diego. In keeping with these agreements, a draft copy of the part-power scoping study (Ref. 11-3) was completed during this quarter and forwarded to ERDA for review and comment. The draft copies of Refs. 11-1 to 11-3 constitute the completion of the 189a No. SU046 milestone entitled "Complete Draft of Conceptual Facility Design Requirements."

REFERENCES

11-1. Weaver, L., and G. Mouritzen, "Helium Circulator Test Facility for the 300-MW(e) GCFR," General Atomic, unpublished data.

11-2. Weaver, L., "Feasibility of Using the Rocketdyne Components Test Laboratory V as the GCFR Helium Circulator Test Facility," General Atomic, unpublished data.

11-3. "Part-Power Helium Circulator Test Facility for the 300-MW(e) Gas-Cooled Fast Breeder Reactor," General Atomic, unpublished data.

12. REACTOR SAFETY (189a No. SU021)

The purpose of this task is to study the reactor safety aspects of the GCFR. Logical probabilistic methods are employed to determine the probabilities associated with various accident initiation and progression sequences and to identify potential design modifications which would help reduce risks. The thermal behavior of the fuel assembly duct walls under conditions of loss of shutdown heat removal is being studied to determine the relative timing of duct wall melting and fuel melting, and analyses of the postaccident fuel contaminant are being performed to assess the capability of the GCFR design. This task also includes liaison between GA and the ERDA-funded GCFR safety task at ANL.

12.1. ACCIDENT INITIATION AND PROGRESSION STUDIES

Accident initiation and progression analysis (AIPA) techniques developed in FY-74 (Ref. 12-1) are being applied to the probabilistic analysis of potential accident sequences leading to low-probability, high-consequence outcomes. The consequences of these sequences are also under study at ANL under the task entitled "GCFR Safety Aspects of Fuel and Core." The objective of this work is to assess the risks of these accident chains in the GCFR.

Work has been completed (Ref. 12-2) on a best-estimate assessment of the probability of accident sequences leading to a loss of coolable core geometry in the 300-MW(e) demonstration plant. Table 12-1 summarizes the results of this work. The total frequency of events leading to a loss of coolable core geometry has been assessed as less than 10^{-5}/yr, including common mode failure considerations. As can be seen from Table 12-1, the dominant cause of loss of coolable core geometry is failure to remove residual heat from the reactor core after shutdown. The most likely

TABLE 12-1
GCFR AIPA RESULTS TO DATE

Accident Cause	Probability (per yr)	Comments
Residual heat removal failure	$<10^{-5}$	Most probable sequence involves loss of electric power; diversity of GCFR cooling systems limited by common reliance on conventional electrical power systems
		Depressurization accidents are negligible contributors to failure probability
Reactor trip failure	$<10^{-7}$	Most probable sequence initiated by total loss of feedwater
		GCFR scram reliability expected to be as good as that proposed for CRBR design (Ref. 12-3)
		Design basis depressurization accident plus scram failure is an extremely low-probability event ($<10^{-10}$/yr)
Structural failure	$<10^{-8}$	Most probable sequence initiated by large earthquake (greater than the safe shutdown earthquake); frequency determined by large earthquake frequency which is highly uncertain

cause of failure of both residual heat removal systems (main loop cooling and CACS) has been identified as an extended loss of on-site and off-site ac electric power. Depressurization accidents have been found to be negligible contributors to residual heat removal failure.

The probability of core damage being initiated by sequences with reactor trip failure has been assessed as less than 1% of the core damage events for which trip occurs. The low probability of such events can be attributed to the relatively low likelihood of an accident initiator requiring immediate shutdown in the GCFR coupled with the low unavailability of the two diverse, automatically actuated shutdown systems.

Severe structural faults leading to core damage are of extremely low probability owing to the high redundancy provided in the PCRV design. Current assessments of the probability of large seismic forces (greater than the design basis earthquake), although highly uncertain, indicate that these events might be the most likely cause of severe structural damage. Such a structural failure event, however, is much less likely than the most probable core damage events for failures of residual heat removal equipment.

12.2. ANALYSIS OF LOSS OF DECAY HEAT REMOVAL ACCIDENT

12.2.1. Introduction

The heat-up and melting sequence for core assemblies during a loss of decay heat removal accident is being investigated to determine the time of cladding, duct, and fuel melting. Detailed two-dimensional thermal analyses have shown that even for the most unfavorable accident sequence, the assembly ducts melt circumferentially before melting of fuel within the assembly begins. These analyses assume that the assembly geometry remains unchanged during the heat-up transient, but the material is removed from the core region as it melts. The analyses also assume that fuel pellets fuse into an integral fuel rod which retains its

integrity after the cladding melts. These analyses have shown that a significant temperature gradient develops across the outermost rows of fuel rods adjacent to the duct wall. The largest temperature gradients exist at the time of duct melting. At this time, the cladding and grid spacers have melted over the core length such that the fuel rods are laterally unsupported over the core length. Thermal bowing of the fuel rods induced by this temperature gradient occurs toward the assembly center, which increases the gap between the outermost fuel rods and the duct wall while decreasing the fuel rod pitch. Deflections due to rod bowing have been calculated in order to determine the degree of fuel rod interference and to assess the effect of bowing on the duct melting time.

12.2.2. Conditions and Assumptions

The deflections of fuel rods subject to a transverse and an axial temperature distribution have been analyzed for the rods located (1) along a traverse to the duct midflat at the time of 50% heat of fusion at the duct midflat and (2) along a traverse to the duct corner (a) at the time of 50% heat of fusion of the duct corner with the unfueled corner rod melted and (b) at the time of 0% heat of fusion of the hottest unfueled corner rod node. These traverses are shown in Fig. 12-1.

The following assumptions have been made for the analysis:

1. The fuel pellets fuse together and form a single rod, and the bonding between the fuel pellets is permanent, so that they retain their geometry as a single rod even after the cladding has completely melted in the fuel region of the fuel rod. There is some experimental evidence to support this assumption.

2. The declad fuel rod is a narrow (one-dimensional) beam; the lateral and transverse stresses in cross-section planes are neglected.

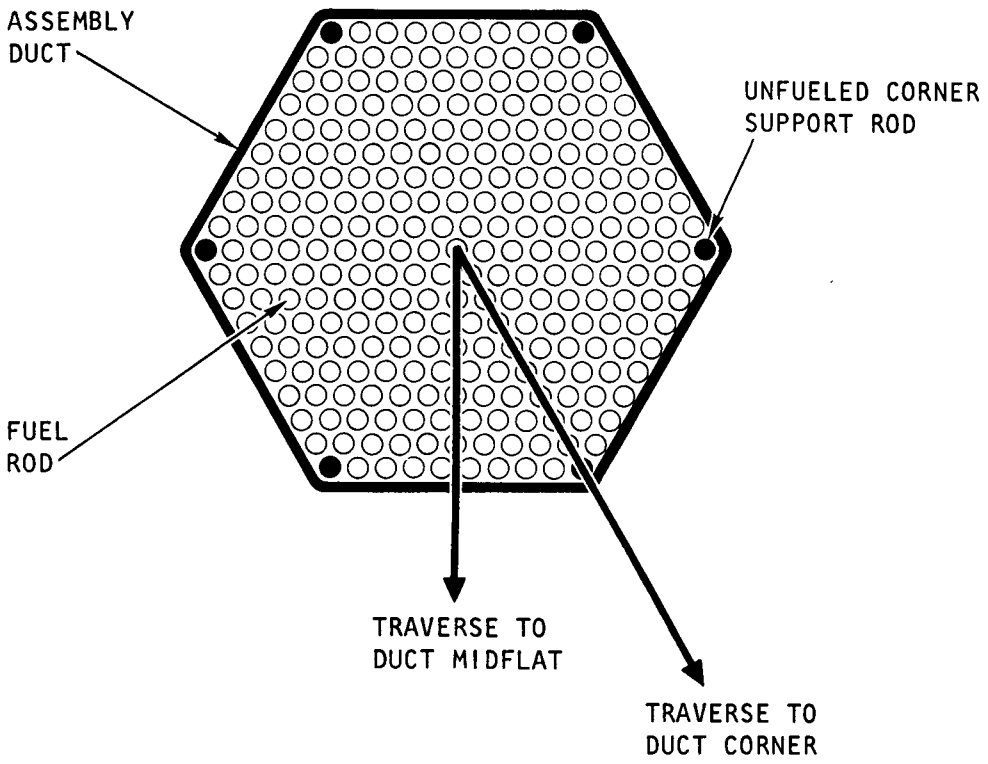

Fig. 12-1. Fuel assembly cross section

3. The temperature T of the declad fuel rod is a linear function of the transverse coordinate y and a chopped cosine function of the axial coordinate z. For the temperature conditions in question, the temperature gradient in the axial direction is much smaller than the temperature gradient in the transverse direction, which is consistent with the one-dimensional beam assumption.

4. The axial thermal expansion is unrestrained owing to concurrent expansion of the duct. This assumption is important in that large axial loads can be developed as a result of the restrained expansion of a thermal beam, and these loads can have a significant effect on beam deflection.

5. Material properties such as modulus of elasticity and coefficient of expansion of the fuel are independent of temperature and are evaluated at the volumetric average temperature of the rod.

12.2.3. End Supports and Boundary Conditions

Three types of end supports, i.e., fixed-fixed, fixed-pinned, and fixed-free, have been considered in this analysis. The lower end of the fuel rods is modeled as a fixed connection because refrozen cladding is assumed to prevent rotation. At the upper end, the boundary condition depends on the strength of pellet bonding at the cool inlet region and the stiffness of the remaining cladding in the upper axial blanket region. The three types of upper boundaries chosen, fixed, pinned, and free, are expected to bracket fuel rod deflections and stresses. Thus, for the fixed-fixed support, the deflection and gradient of deflection are zero at both ends. For the fixed-pinned support, the deflection and gradient deflection are zero at the fixed lower end; at the upper end, the deflection is zero and the second derivative of the deflection is proportional to the thermal moment. For the fixed-free support, the deflection and gradient of deflection are zero at the lower end; at the upper end, where displacement moment and shear are zero, the second derivative of the deflection is

proportional to the thermal moment, and the third derivative of the deflection is proportional to the first derivative of the thermal moment.

12.2.4. Data

Temperature data on fuel rods have been obtained from previous duct melting analyses which assume that the fuel rods are not deformed. The input data, which are in the form of a temperature difference ΔT across the fuel rods at the core midplane, are given in Table 12-2.*

The mean thermal expansion coefficient α of the fuel material has been calculated using the following equation (Ref. 12-4):

$$\alpha = 6.8 \times 10^{-6} + 2.9 \times 10^{-9} \overline{T} \text{ (mm/mm °C)} \quad , \qquad (12\text{-}1)$$

where $\overline{T}$ is the volumetric average temperature (°C) of the fuel rod.

12.2.5. Discussion of Results

Analysis of free deflection (i.e., not restrained by neighboring rods) to determine the extent of rod-to-rod interference has been completed for all the cases listed in Table 12-2. The deflection and interference patterns are similar for all six cases. However, the deflections are significantly influenced by the choice of the upper boundary condition. The high-pressure-drop core design results in the largest deflections and interference because it combines the largest temperature gradients with the smallest rod-to-rod spacing. Figures 12-2 to 12-4 show the calculated free deflections of the fuel rods on the traverse to the duct midflat for the high-ΔP fuel assembly (case 4, Table 12-2). The free deflections of each rod are plotted without accounting for interference between rods. The distance S between rods is equal to the minimum allowable deflection without interference. Since all rods deflect in the same direction, larger deflections are possible

*The temperature data for the rods in a given transverse have been chosen at the point in time during the loss of decay heat removal accident sequence when these temperature gradients are the largest.

TABLE 12-2
TEMPERATURE DIFFERENCE ΔT ACROSS THE FUEL RODS AND THE CORNER ROD
AT THE CORE MIDPLANE

	Fuel Assembly Design					
	Low ΔP			High ΔP		
	Rod Traverse to Duct Midflat	Rod Traverse to Duct Corner		Rod Traverse to Duct Midflat	Rod Traverse to Duct Corner	
Time after shutdown[a] (s)	111	117	176	118	122	173
Duct condition	50% HOF[b] at midflat	0% HOF in corner rod	50% HOF at corner	50% HOF at midflat	0% HOF in corner rod	50% HOF at corner
Case No.	1	2	3	4	5	6
	ΔT (°C)					
Fuel rod[c] 1	406	87[d]	Melted[d]	436	74[d]	Melted[d]
Fuel rod 2	284	345	370	278	282	412
Fuel rod 3	150	170	158	151	196	144
Fuel rod 4	63	84	91	78	101	107
Fuel rod 5	31	34	45	45	51	43
Fuel rod 6					44	24

[a] Assumed loss of flow time is 2 s after shutdown.

[b] HOF = heat of fusion.

[c] Counted from the duct wall inward.

[d] Rod 1 is the unfueled corner support rod.

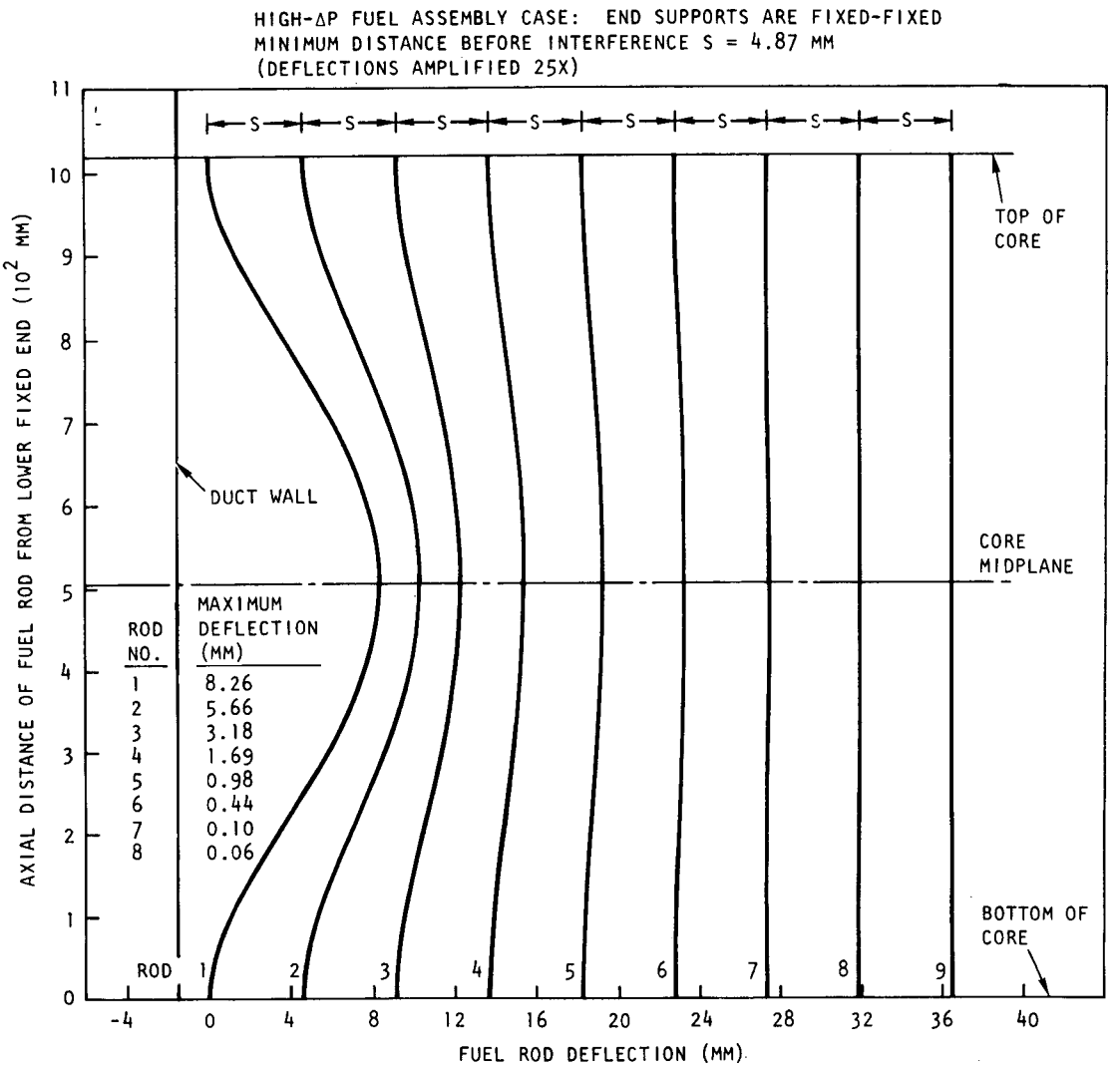

Fig. 12-2. Thermal deflection with respect to the centerline of the fuel rod along a traverse to the midflat at the time of 50% heat of fusion at the duct midflat

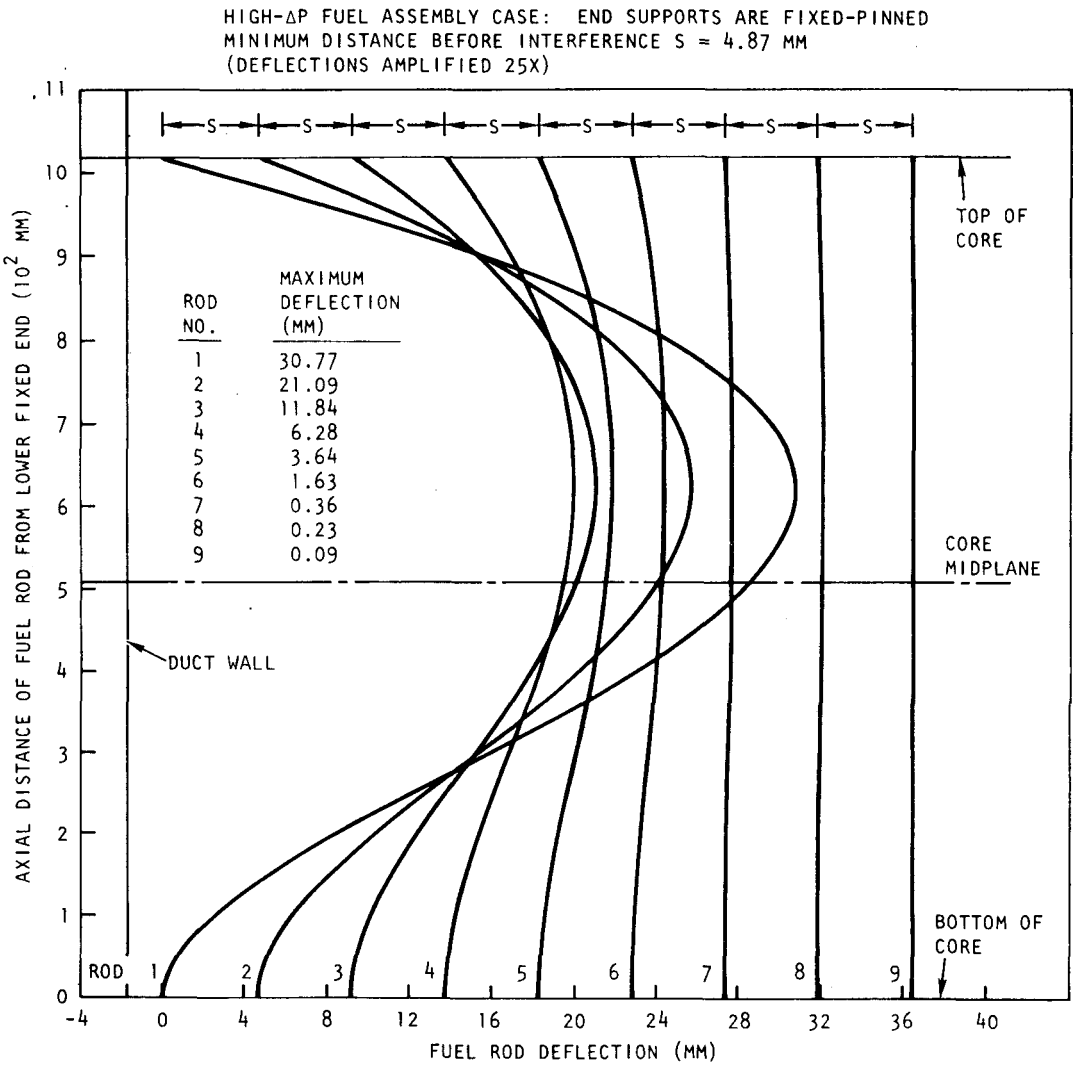

Fig. 12-3. Thermal deflection with respect to the centerline of the fuel rod along a traverse to the midflat at the time of 50% heat of fusion at the duct midflat

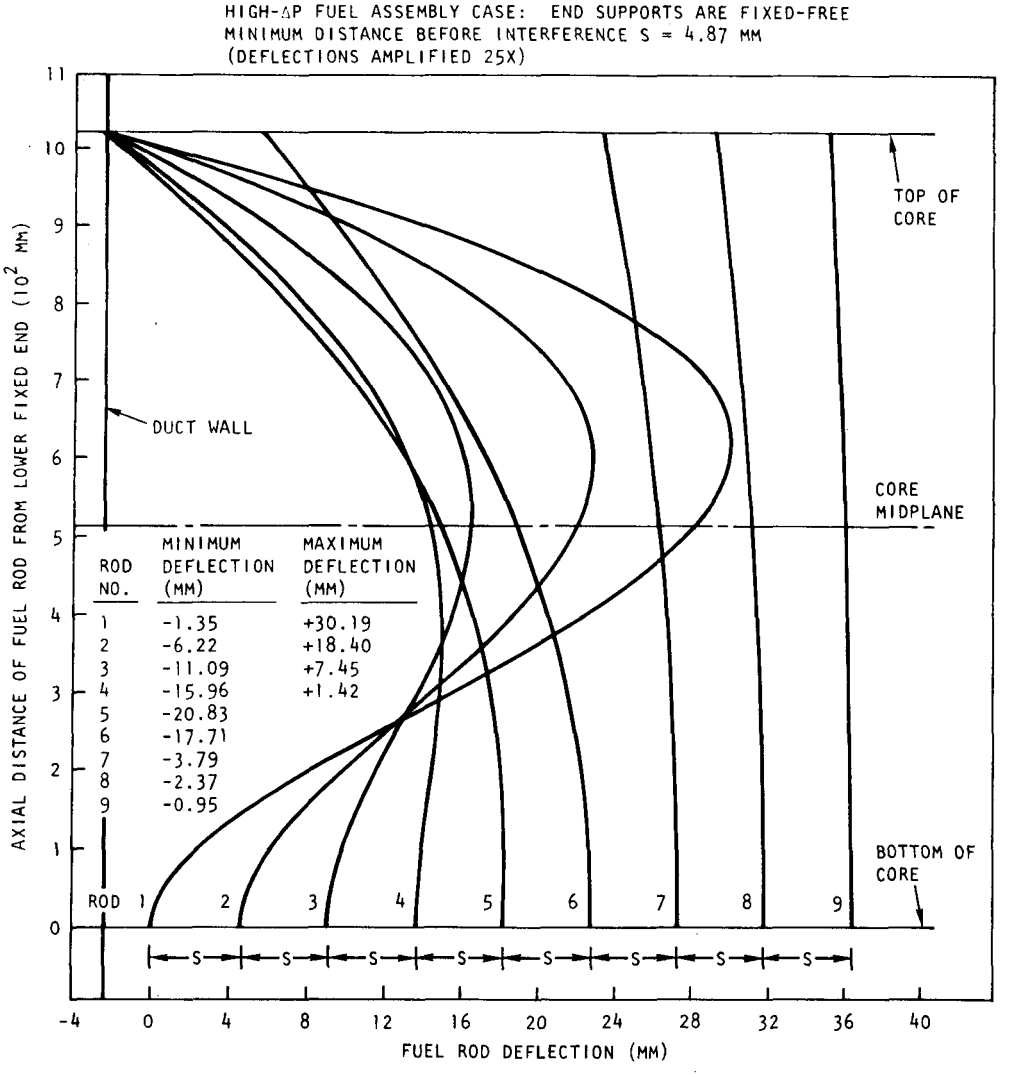

Fig. 12-4. Thermal deflection with respect to the centerline of the fuel rod along a traverse to the midflat at the time of 50% heat of fusion at the duct midflat

without interference. Physical interference between two rods is indicated wherever their deflection shapes overlap. The maximum free deflection of each rod is also given in these figures; the rods are numbered from the duct toward the assembly center. Figure 12-2 shows that for a fixed boundary condition at the top of the core, no interference occurs between rods. This boundary condition would be approached if the restraining moment from the unmelted cladding in the upper axial blanket were large and the pellet bonding in the inlet region of the rods were strong.

A weak restraining moment by the unmelted cladding in the upper axial blanket is simulated by a pinned connection at the top (i.e., no restraining moment for rotation, only shear restraint). Figure 12-3 indicates significant interference of up to seven rows of fuel rods over as much as half the core length for this boundary condition. The maximum deflections are shifted to the upper half of the core. For clarity, the scale for the deflections have been amplified by a factor of 25.

If bonding of fuel pellets is weak near the top of the core, the fuel rods could become detached at the core - upper blanket interface as a result of bowing-induced stresses. Such a condition is simulated by a free upper boundary condition where neither moment restraint nor shear restraint is present. In this case the fuel rods will initially tend to bow outward until interference with the duct wall or the unfueled corner support rod occurs. Figure 12-4 shows the deflections resulting from this boundary condition. It is assumed that the fuel rods are free to deflect outward toward the duct wall, which prevents further outward deflection and thus forces the rods to deflect inward toward the core region. Up to seven fuel rods experience interference over a significant fraction of the core length.

For each of the three boundary conditions, very similar but somewhat less severe interference patterns have been calculated for the five other cases. In no case did a fixed-fixed boundary condition lead to interference, although for either the fixed-pinned or the fixed-free boundary

condition (with deflection restraint by the duct wall or the unfueled corner support rod at the free upper end), it was found that from four to seven rows of fuel rods interfere with each other prior to duct melting. On the traverse to the duct corner, the unfueled corner rod is calculated to deflect much less than the adjacent fuel rods. However, deflection of the fuel rods is very similar for the traverse to the duct midflat and the traverse to the corner. Thus, if the restraint provided by the upper axial blanket is not fairly stiff, a general "tightening up" of the rod bundle over a significant fraction of the core will result. Rod interference will lead to reactive contact forces, making the deflections physically compatible (i.e., with no overlap) and inducing additional stresses.

It is concluded that rod-to-rod interference may occur following cladding melting during a loss of decay heat removal accident. The physically compatible deflections, including interactive forces, are being determined. The resulting bending stresses in the fuel rods will also be determined. Out-of-pile direct electric heating experiments at ANL are expected to yield information on the bending strength of bonded fuel pellet stacks. The effect of fuel rod bowing on the timing of duct melting will also be assessed. The slow heat-up of fuel rods during a loss of decay heat removal accident may lead to significant fuel swelling, which would restrict the degree of bundle tightening which can occur and lead to earlier rod-to-rod interference.

12.3. SAFETY RESEARCH AND DEVELOPMENT LIAISON

Safety R&D liaison with ERDA and the national laboratories involved in the GCFR Safety Program was maintained during this quarter at a somewhat reduced level because the primary efforts at GA and at ANL were aimed at completing documentation of the 2-yr effort on high-consequence accident assessment. A new liaison effort has been initiated with ANC (now EG&G). EG&G will perform a review for ERDA during FY-77 of the probabilistic accident analysis work done at GA.

12.4. POSTACCIDENT FUEL CONTAINMENT

Results have been reported (Ref. 12-5) for the study of upward heat removal by natural helium circulation at an extreme depressurized condition. This study has been expanded to cover a partial core meltdown condition in which the blanket assemblies and the fuel cladding and box wall above the core region remain in place. Results were obtained for system pressures from 0.61 MPa to a full pressure of 9.0 MPa.

12.4.1. Initial Configuration and Assumptions

The initial configuration of a 300-MW(e) GCFR reactor cavity after a postulated core meltdown accident is shown in Fig. 12-5; a partial core meltdown in which the upper axial blanket and the radial blanket remain in place is assumed. The dropped core debris, presumed to be molten, is accumulated above the lower thermal shield. The events leading to this configuration are assumed to occur instantly at the beginning of the accident. After a total loss of forced circulation, the helium loop isolation valves are normally closed, so that natural convection coolant flow paths can only develop within the central cavity. After a 30-min delay, the isolation valves in the core auxiliary cooling loops are assumed to be mechanically opened, and a natural convection flow path develops through the auxiliary cooling loops, as shown in Fig. 12-5. The helium flows upward through the central portion of the reactor cavity which forms the hot leg with an average temperature T_h and then flows downward through the auxiliary heat exchangers to the outer radial shield annulus which forms the cold leg with an average temperature T_c. The effective loop height h is measured from the lower end of the outer radial shield to the midheight of the auxiliary heat exchangers.

The two-dimensional computational model and the initial conditions are shown in Fig. 12-6; for simplicity, irregular geometrical shapes have been replaced by regular ones. The perforated grid plate and the blanket rod bundles are represented by equivalent solid masses. The radial shields

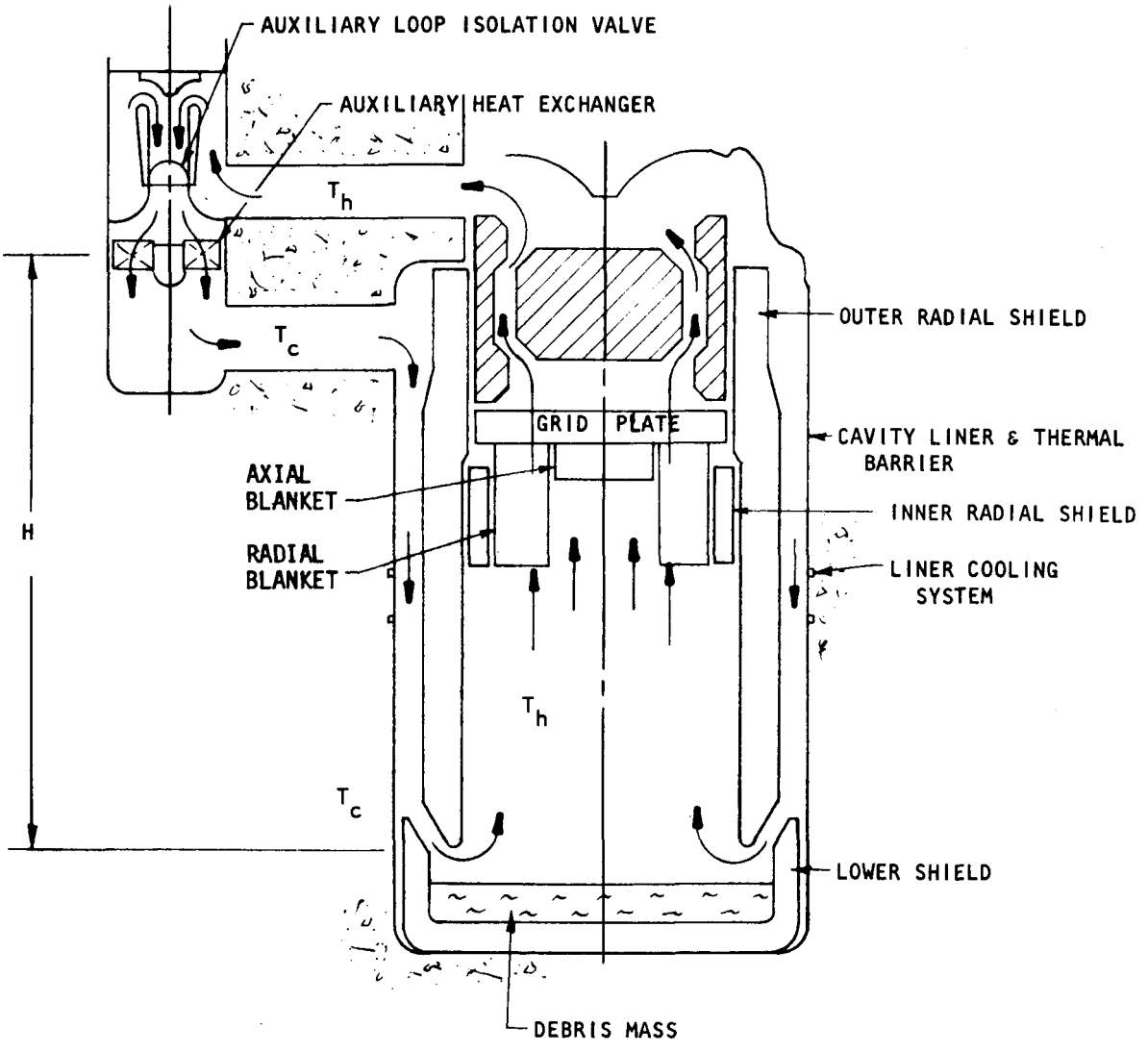

Fig. 12-5. Initial configuration and natural circulation flow path

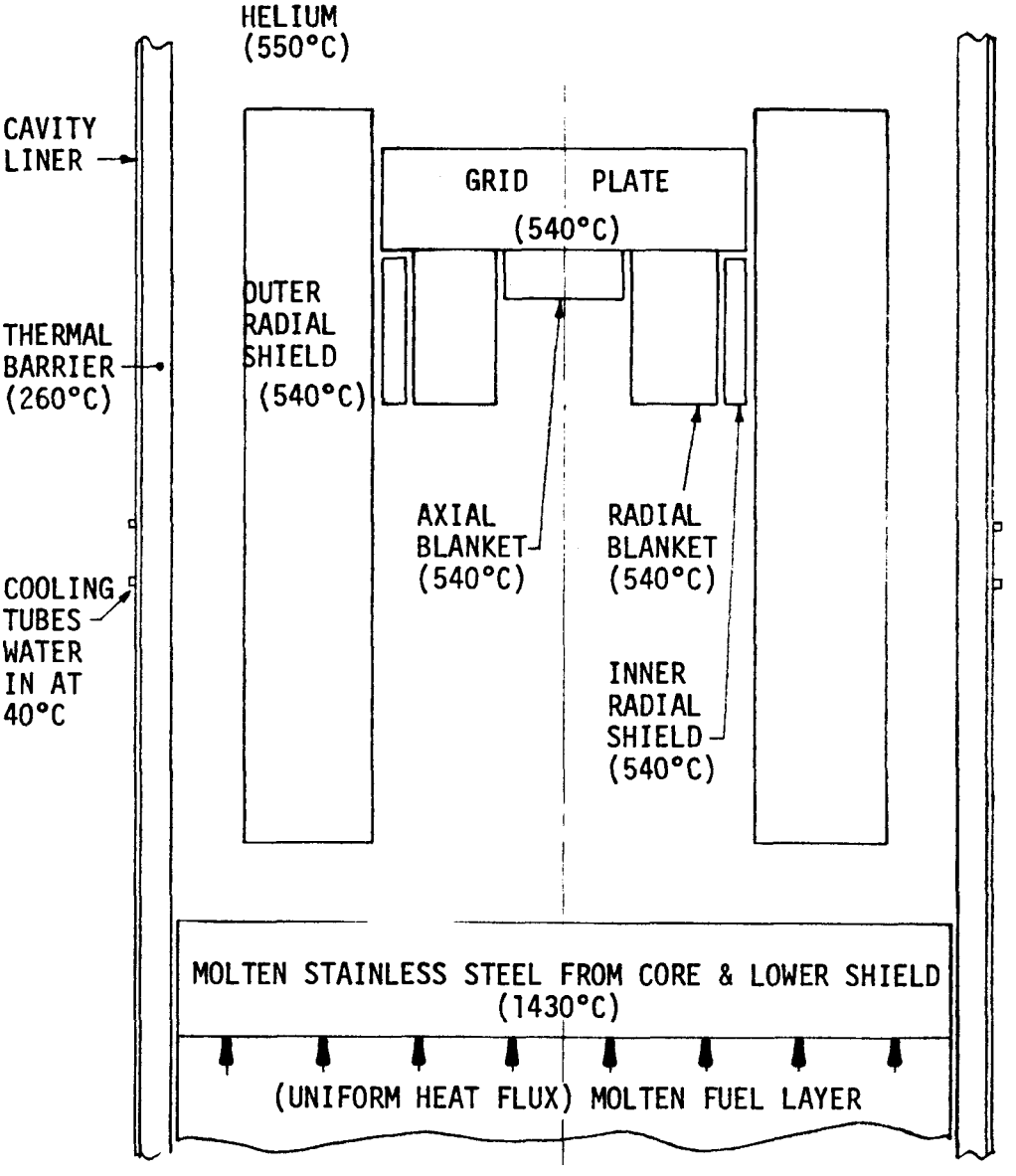

Fig. 12-6. Computational model with initial temperatures

and the radial blanket assemblies are assumed to consist of one material having the weighted property values of the actual materials, and the molten core debris is assumed to separate into two distinct layers, with the molten stainless steel from cladding and assembly ducts overlaying the molten fuel. Volatile fission products are presumed to have escaped into the reactor cavity, where they flow with the helium to the auxiliary heat exchangers. The volatile fission products in the unmelted radial blanket are not released to the helium. The nonvolatile fission products are distributed in the oxide fuel and the molten stainless steel. Based on the isotope-by-isotope decay heat rate for the first 30 hr, which covers the time span of the present analysis, 80% of the decay heat (from the nonvolatile products) is generated in the oxide region, and the remaining 20% is generated in the molten stainless steel region. Based on previous analyses (Ref. 12-6), two-thirds of the heat generated in the oxide layer is assumed to flow upward into the steel layer. A uniform heat flux passing into the bottom of the molten stainless steel layer constitutes the lower boundary of the computational model. The sides of the stainless steel layer are presumed to be insulated. Internal free convection within the molten stainless steel layer is treated as an equivalent heat conduction with an assumed effective thermal conductivity based on previous analysis (Ref. 12-6). All reactor internal surfaces emitting or reflecting thermal radiation are assumed to be gray and diffuse. The emissivity of the molten stainless steel surface is assumed to be the same as that of solid stainless steel, and the helium, which is partially mixed with aerosols, is assumed to be transparent.

12.4.2. Results and Discussion

Numerical results were obtained using the NUTAP computer code (Ref. 12-7), a multidimensional network-type thermal analysis computer program. The upward-flowing portion of the decay heat in the molten pool and the cold helium temperature at the exit of the auxiliary heat exchangers were precalculated and the results were prepared as input to the NUTAP code. The results of the decay heat calculation are given in Fig. 12-7, which shows the total decay heat flowing upward, the decay heat in the core debris

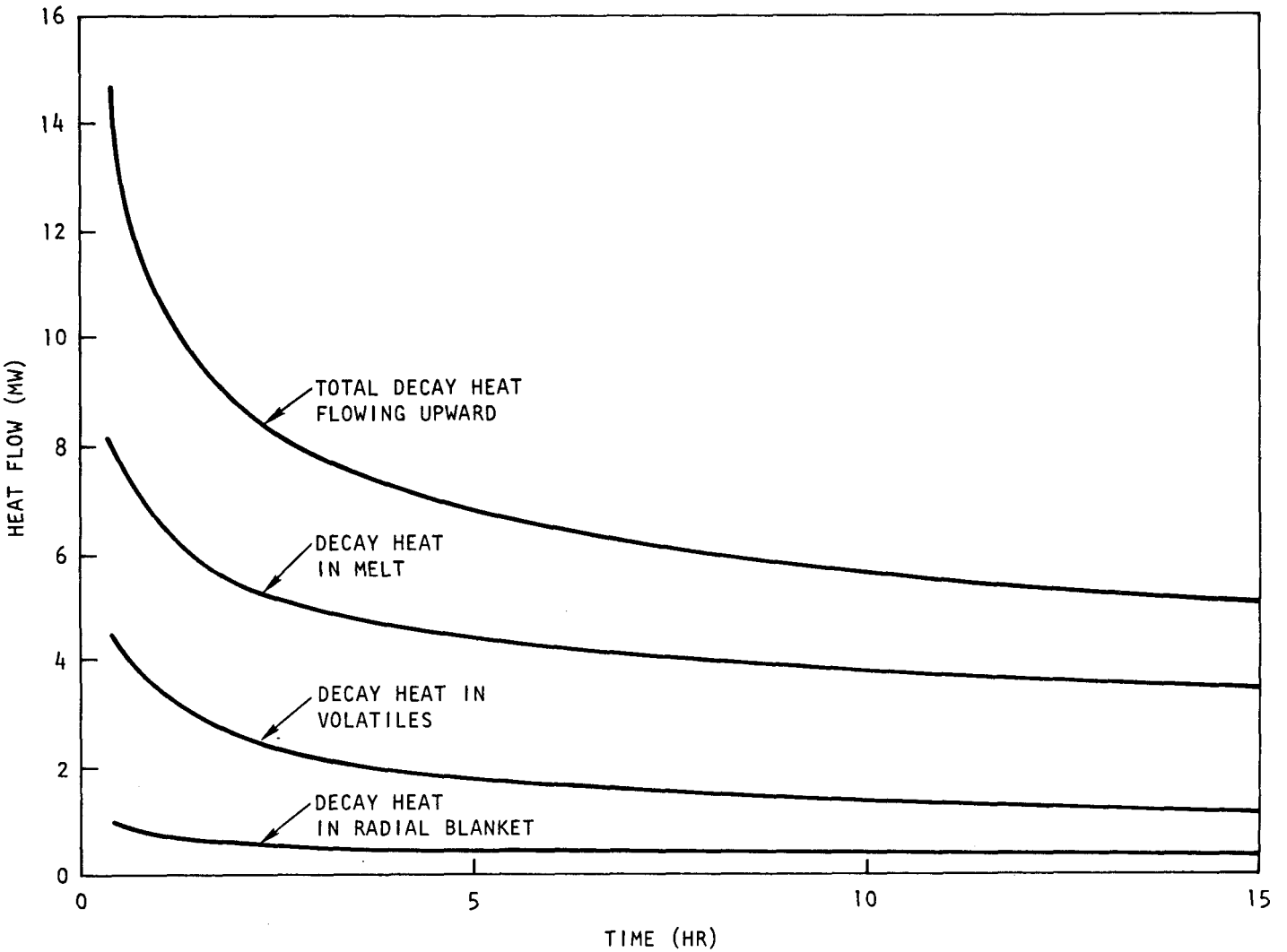

Fig. 12-7. Distribution of upward-flowing decay heat vs time

melt, the decay heat from the volatile fission products, and the decay heat in the radial blanket. The cold helium temperature as a function of helium mass flow and hot helium temperature at the inlet of the auxiliary heat exchanger is shown in Fig. 12-8. Based on auxiliary heat exchanger performance characteristics, a simple linear relation between the cold and hot helium temperatures was observed.

Calculations were made for various depressurization conditions, and the lowest allowable residual pressure without melting of any reactor internal structure was 0.61 MPa. Figure 12-9 shows the temperature history at various locations for a coolant pressure of 0.61 MPa. It can be seen that the temperatures at all surface locations increase during the first 30 min, when no helium is circulating through the core auxiliary cooling loops. Sudden temperature drops occur at 30 min, when auxiliary loop isolation valves are mechanically opened. The debris surface, assumed to be molten at the time of accident initiation, reaches its maximum temperature of 1640°C after 2 hr. The surface temperature at the lower end of the outer radial shield reaches the melting point after 2 hr and begins to decrease after 5 hr. Temperatures at other locations are well below the melting point except in the radial blanket, where temperature increases continuously owing to decay heat generation. Only a small helium flow rate develops through the radial blanket assemblies because of the high flow resistance compared with the remaining portion of the core assemblies. After cladding and assembly wall melting in the radial blanket, the blanket assemblies drop into the molten pool and thereby reduce the flow resistance in the central cavity; consequently, more helium flow will be naturally induced. Thus, convective cooling is improved, resulting in lower temperatures for the structures. This configuration is not considered in the present analysis.

Temperatures at all locations pass their maximum values within 15 hr except for the grid plate temperature, which continues to increase for another 5 to 10 hr but does not reach the melting temperature. Maximum temperatures at various locations are shown in Fig. 12-10 as a function

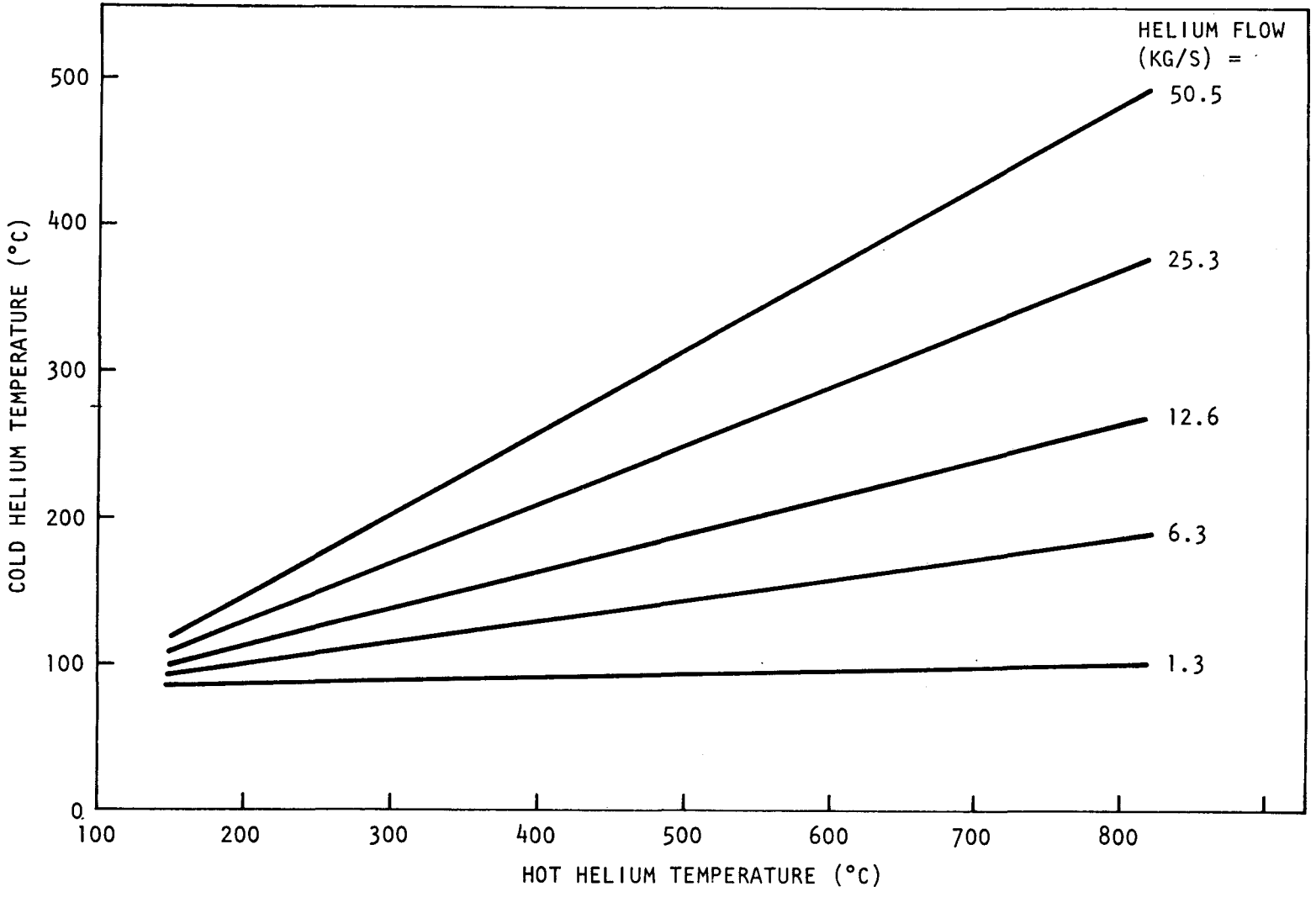

Fig. 12-8. Hot and cold leg temperatures for various mass flow rates

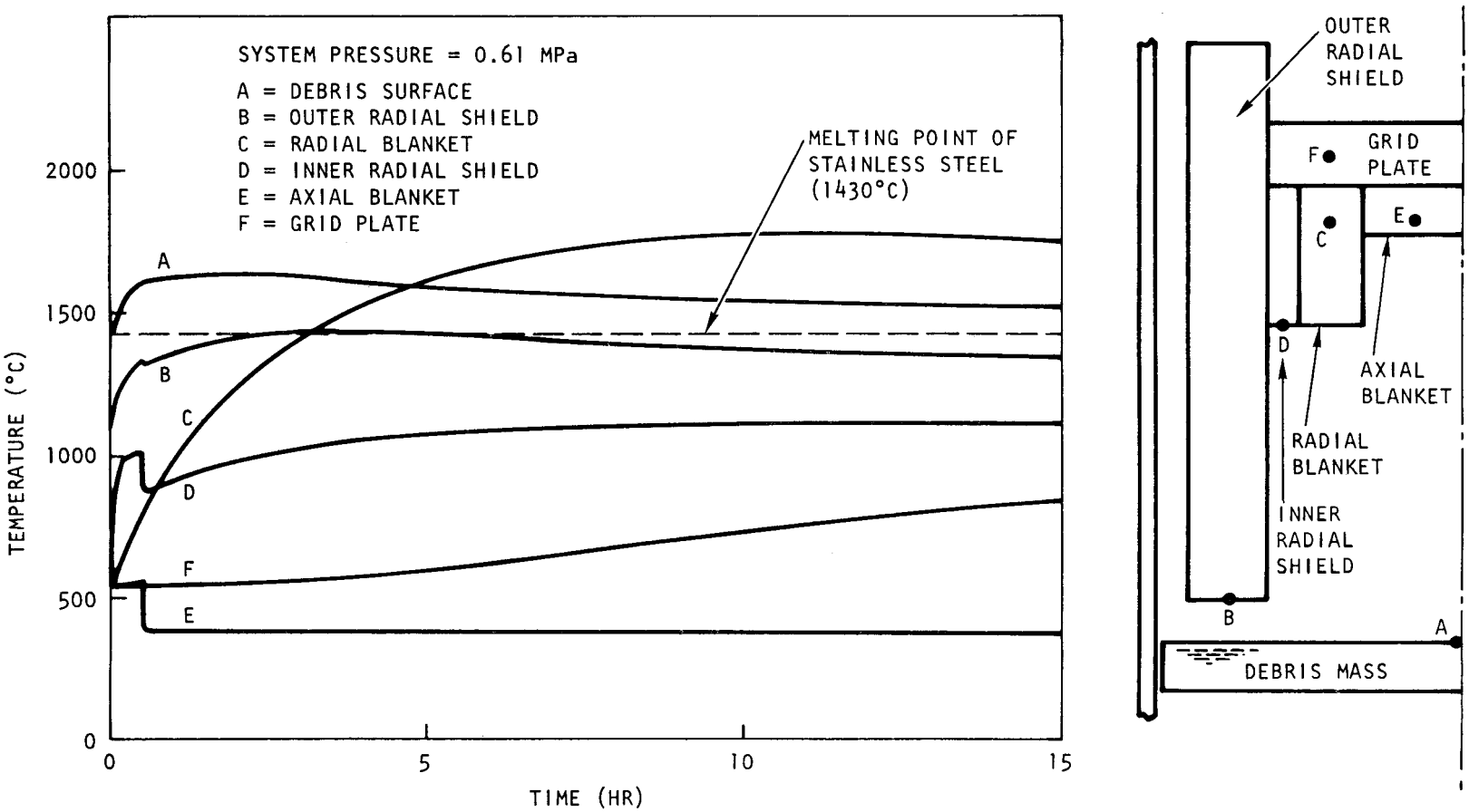

Fig. 12-9. Temperature vs time at various locations for a system pressure of 0.61 MPa

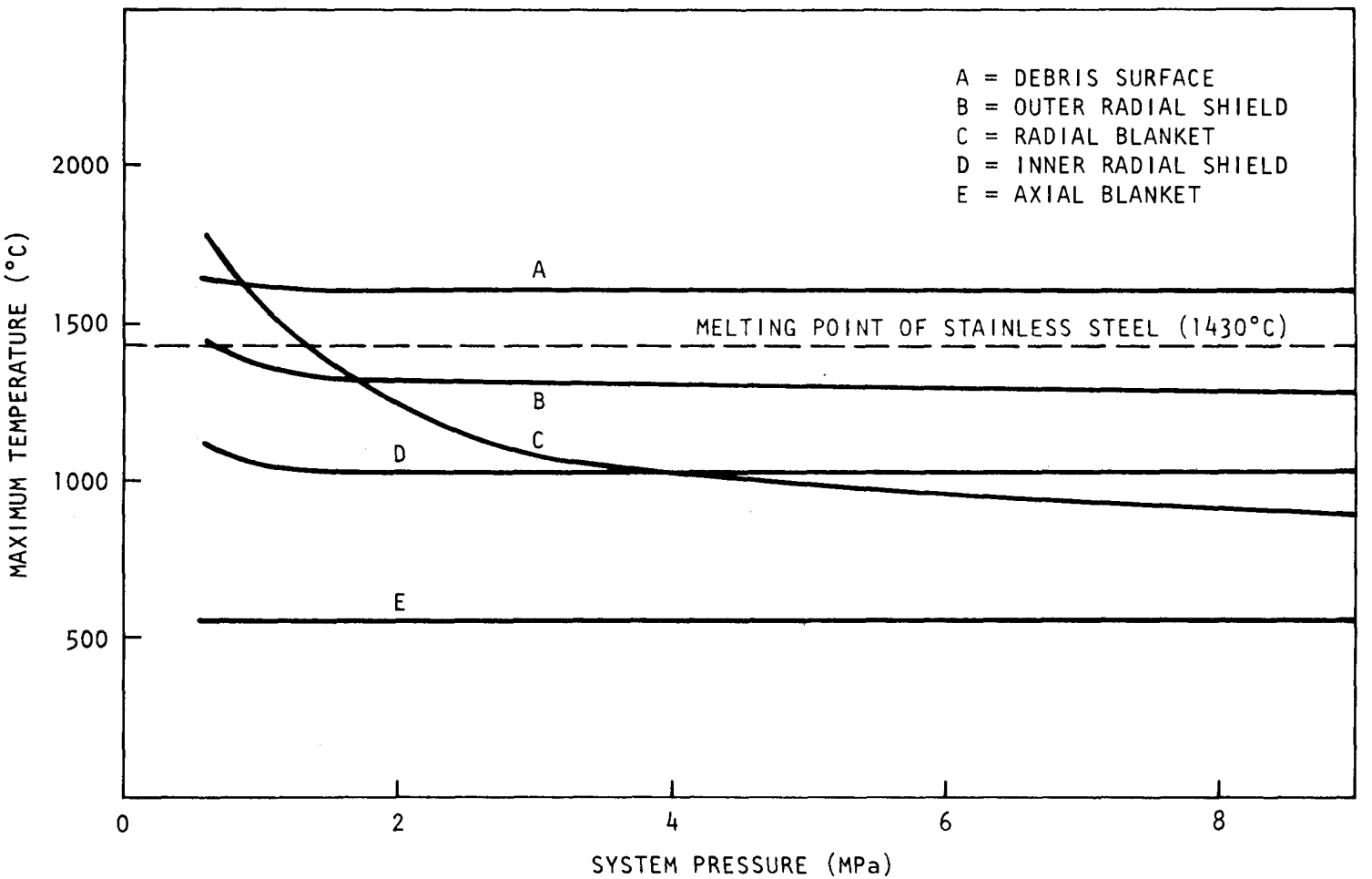

Fig. 12-10. Maximum temperature at various locations vs system pressure

of the system pressure. It can be seen that no melting of the radial shield surface occurs for system pressures greater than 0.61 MPa, and no meltdown of the radial blanket occurs for system pressures greater than 1.4 MPa.

Helium temperatures as a function of time are shown in Fig. 12-11 for various system pressures. Because of the low specific heat capacity of helium, maximum temperatures are reached early in the 30-min period during which the isolation valves are closed. Helium temperatures in the annulus between the outer radial shield and the thermal barrier are much lower than those in the central cavity because of the comparatively larger cooling surface in the annulus. This temperature difference initiates the helium flow when the auxiliary loop isolation valves are mechanically opened. At this moment, a sharp temperature drop is observed. The temperature difference between the hot leg and the cold leg is also reduced owing to helium circulation.

12.4.3. Conclusions

For system pressures greater than 0.61 MPa, natural helium convection has been shown to be effective in transporting the upward-flowing decay heat from a core melt on the central cavity floor to the CACS heat exchangers. Therefore, forced-convection helium circulation is not necessary for upward heat removal after a pressurized core meltdown in the GCFR demonstration plant. However, two requirements are necessary to prevent melting of the radial thermal shield at the lower end: (1) the CACS loop isolation valves must be opened within about 30 min, and (2) the PCRV pressure relief valves must maintain system pressure above 0.61 MPa.

For fully depressurized conditions, natural convection of helium will not prevent melting of the lower portion of the radial thermal shield. Probabilistic accident analyses have shown that a core meltdown caused by an accidental primary system depressurization is of significantly lower probability than a pressurized core meltdown accident.

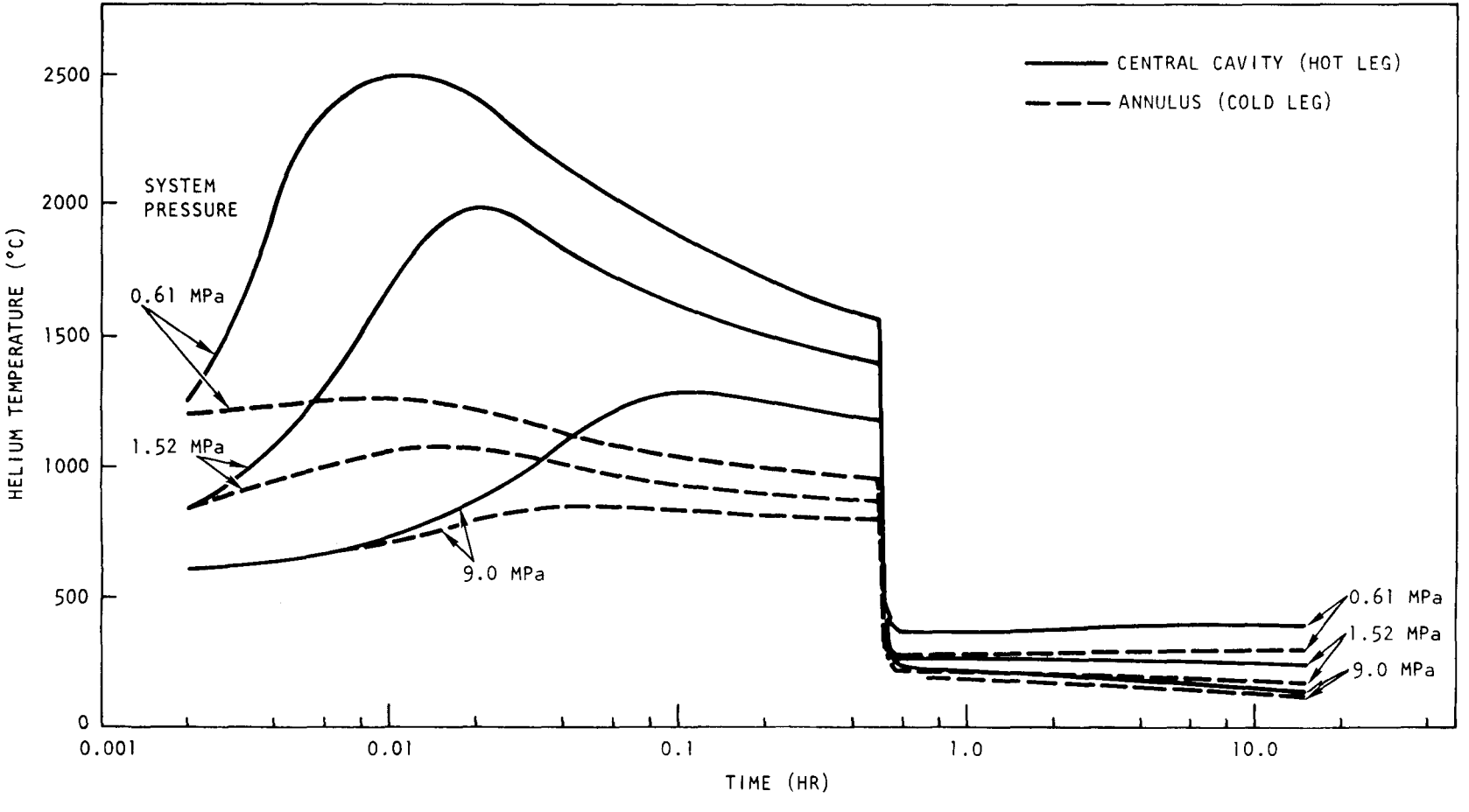

Fig. 12-11. History of helium temperature for different system pressures

Forced water circulation in the CACS heat exchangers was assumed for this analysis. Future investigations are planned to determine the capability of the system for heat rejection from the CACS heat exchangers by natural convection.

REFERENCES

12-1. "GCR Accident Initiation and Progression Analysis Progress Report for the Period February 1 Through June 30, 1974," ERDA Report GA-A13094, General Atomic, October 8, 1974.

12-2. "Gas-Cooled Fast Breeder Accident Initiation and Progression Analysis Progress Report for the Period July 1, 1975 Through June 30, 1976," General Atomic, unpublished data.

12-3. "Clinch River Breeder Reactor Project Preliminary Safety Analysis Report," Project Management Corporation (NRC Docket 50-537).

12-4. "Properties for LMFBR Safety Analysis," ERDA Report ANL-CEN-RSD-76-1, Supplement 1, Argonne National Laboratory, April 1976.

12-5. "Gas-Cooled Fast Breeder Reactor Quarterly Progress Report for the Period February 1, 1976 Through April 30, 1976," ERDA Report GA-A13868, General Atomic, May 31, 1976, p. 9-6.

12-6. Menzel, H. F., and C. S. Kang, "Status of Post-Accident Fuel Containment Studies for a 300-MW(e) GCFR Demonstration Plant," General Atomic Report GA-A13734, December 18, 1975.

12-7. Leach, C. E., and E. L. Kelley, Jr., "TAP-LOOP: A Stable Thermal Analyzer Code for Thermal Analysis of Closed Hydraulic Systems," USAEC Report BNWL-1172, Battelle Northwest Laboratory, 1970.

13. GCFR SAFETY TEST PROGRAM (189a No. SU015)

13.1. GRIST PROGRAM

The GRIST Program is being evaluated by ERDA, ANL, ANC, and GA as a potential follow-on to analytical and experimental programs being conducted under the LMFBR and GCFR programs. The GRIST program has the objective of going beyond design basis accidents and, in particular, investigating the behavior of melted cladding and fuel. The GCFR Safety Program Review Committee has reached the consensus that GCFR fuel tests in a transient facility are needed. Acting on this recommendation, ERDA has directed that work commence on a transient GCFR loop program (to be known as GRIST-2). This program has a higher priority and will replace work previously scheduled for the steady-state GCFR loop program in the engineering test reactor (ETR) (GRIST-1).

During this quarter, efforts were devoted to completion and documentation of the GRIST-1 multisection test assembly conceptual designs to ensure that GRIST-1 information already developed was properly reported. The multisection test assemblies considered were designed to prototypically simulate duct wall behavior during temperature excursions which cause duct wall melting. Two multisection test assembly designs were prepared at GA, both of which evolved from the 37-rod fuel test assembly design (developed earlier). These designs were developed in order to include localized duct melting as a part of the test program. The two test assembly designs, a double- and a triple-section design, are described in detail in Ref. 13-1. Consistent with the GCFR fuel design concept, both designs incorporate hexagonally patterned rod bundles and flow ducts with a cylindrical section above the manifold grid.

Documentation of the GRIST-1 test bundle designs has been completed, and the design requirements and conceptual design description of the

double- and triple-section test assemblies for the GRIST-1 program have been forwarded to ERDA. No further work on GRIST-1 is scheduled. As requested, test facility requirement information for the GRIST-2 program has been supplied to ANC.

13.2. DUCT MELTING AND FALLAWAY TEST PROGRAM

An out-of-pile test program has been initiated at the Los Alamos Scientific Laboratory (LASL) to investigate duct melting and fallaway phenomena during a loss of decay heat removal accident. General Atomic will define the test objectives, criteria, and requirements, and LASL will develop a program plan. A technical meeting was held at LASL on September 20 and 21. The primary objectives of the meeting were to further familiarize the LASL staff with the GCFR fuel assembly design and the accident sequence and to discuss a preliminary set of test criteria and requirements. These objectives were met, and the discussions have resulted in an expansion of the scope of test criteria and requirements in several areas. The expansion in scope is related to the desirability of defining specific test requirements and features with respect to heater power, coolant flow capability, and the force inducing assembly dropout rather than descriptive requirements for the conditions to be simulated. The expanded definition of test criteria and requirements will be completed by the end of 1976.

As part of the design information provided to LASL during this quarter, the axial power distribution in the core and axial blanket as well as the time dependence of the decay heat in these regions was defined and is shown in Figs. 13-1 and 13-2. Prototypical test simulation requires simulation of the decay heat distribution in space and time in the out-of-pile tests. However, the relative importance of fission product decay and breeding product decay to the total decay heat is different for the core and the blanket region. This results in a different time dependence for the total decay heat in the core and blanket region, as seen in Fig. 13-2. Simulation of the correct decay heat distribution in the lower axial blanket as well as its time dependence is important for correctly

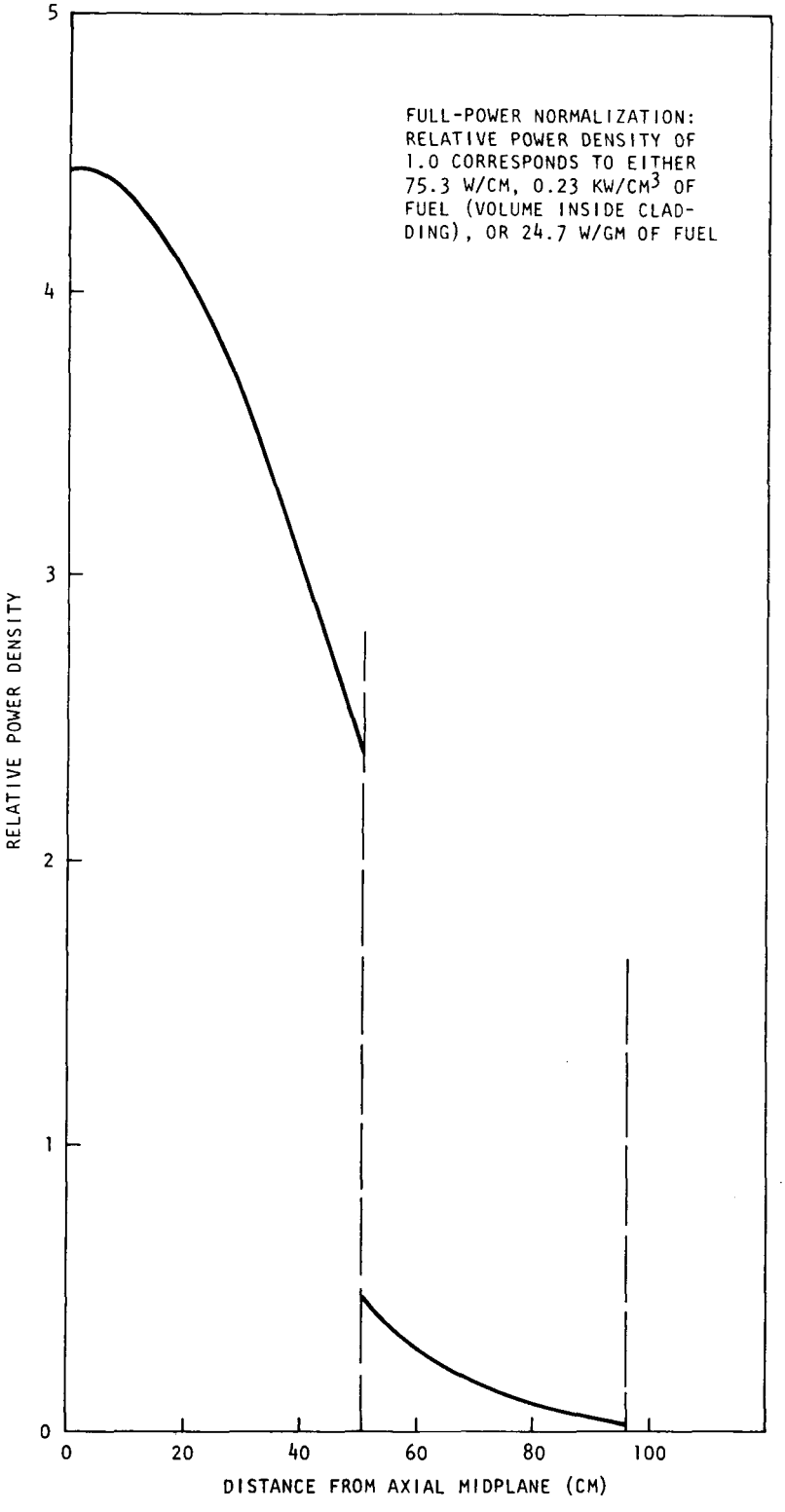

Fig. 13-1. Relative axial power distribution in the 300-MW(e) GCFR demonstration plant at the beginning of an equilibrium cycle

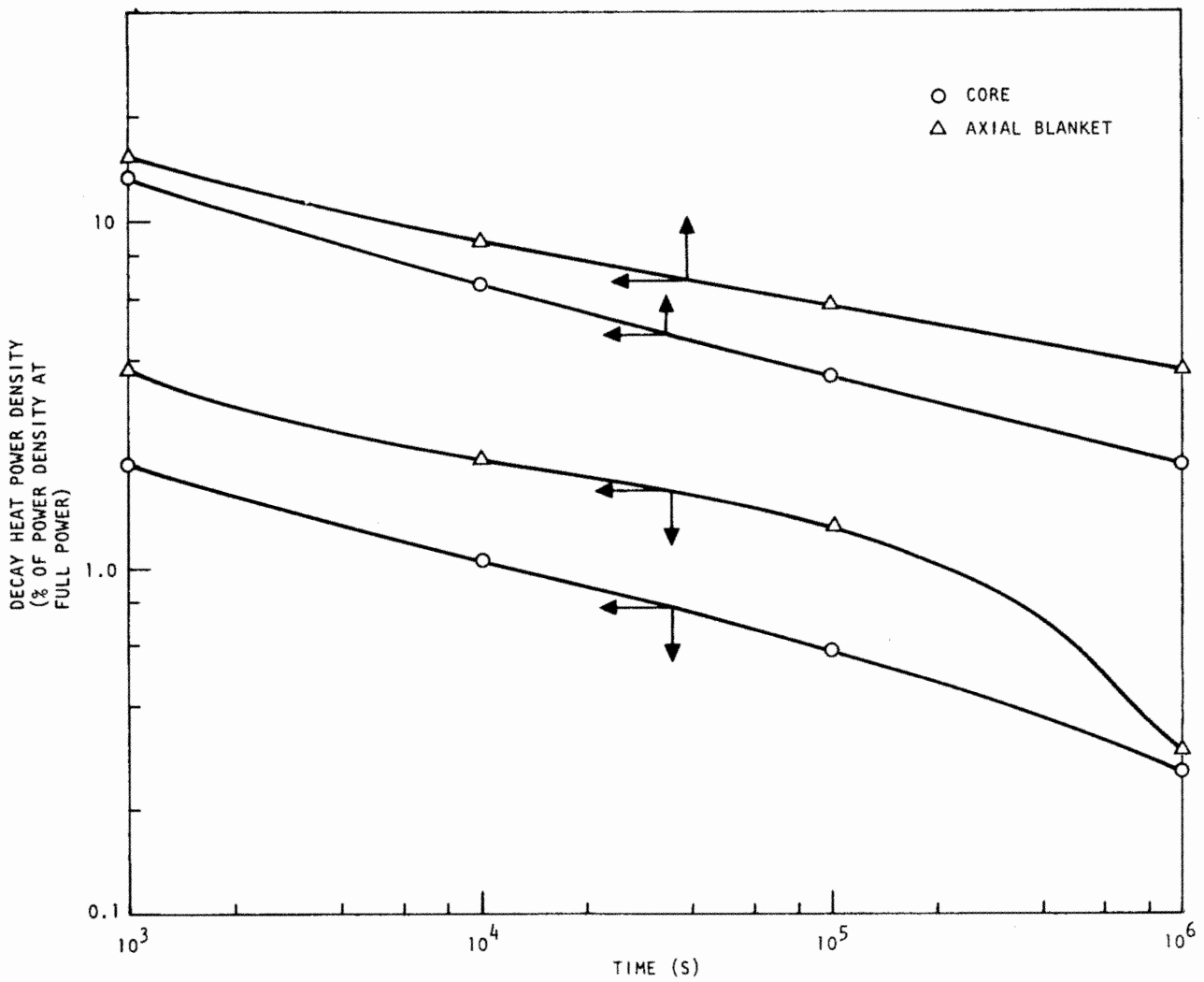

Fig. 13-2. Core and axial blanket decay heat vs time

simulating the conditions for molten cladding refreezing and duct heatup in the lower blanket. It appears to be difficult to experimentally simulate the different time dependence of the decay heat in the core and the blanket since for a given integral heater rod design, the ratio of blanket power to core power is fixed except for the temperature-dependent variation of the electrical resistance of the heater material. Further investigations are necessary to resolve this potential limitation of out-of-pile tests.

REFERENCE

13-1. "Gas-Cooled Fast Breeder Reactor Quarterly Progress Report for the Period May 1, 1976 Through July 31, 1976," ERDA Report GA-A13975, General Atomic, August 31, 1976.

14. GCFR NUCLEAR ISLAND DESIGN (189a No. SU064)

14.1. GENERAL NUCLEAR ISLAND ARRANGEMENT AND SYSTEMS

Work has started on the definition and general arrangement of the nuclear island. The scope of the Balance of Plant Requirements (BOPR) document, which will supply the basic information to an architect-engineer, has been determined, and preliminary RECS* logic diagrams for preparation of the BOPR have been completed. Since the BOPR document covers all aspects of NSSS/BOP interfaces, it encompasses most of the work under this task.

14.2. NUCLEAR ISLAND STRUCTURAL DESIGN AND LAYOUT

The purposes of this subtask are to (1) perform the necessary design of the GCFR nuclear island; (2) participate in the layout of equipment in the containment, service, and auxiliary buildings; and (3) support efforts needed to assure the feasibility of the nuclear island.

This subtask was initiated during this quarter. Under private funding, a review was made of Bechtel Corporation's BOP preliminary engineering and cost estimate (Ref. 14-1) and follow-on study (Ref. 14-2) to determine their recommendations for the nuclear island buildings. Equipment and component lists were compiled for each building, and a survey of present design requirements and preliminary layouts will be made.

REFERENCES

14-1. "300-MW(e) Gas Cooled Fast Breeder Reactor Balance of Plant Preliminary Engineering and Cost Estimate," Bechtel Job 10437, August 1973.

*RECS = Resource Evaluation and Control System.

14-2. "300 MW(e) Gas Cooled Fast Breeder Reactor Balance of Plant Follow-on-Study," Bechtel Job 10437, November 1973.